A FIBRE FLEXURE – LUMPED SHEAR MODEL FOR MASONRY STRUCTURES.

Dummy page

A FIBRE FLEXURE – LUMPED SHEAR MODEL FOR MASONRY STRUCTURES.

By

Willem Leendert Nobel

in partial fulfilment of the requirements for the degree of

Master of Science

in Civil Engineering

at the Delft University of Technology,
to be defended publicly on 16th June 2017, at 15:30

Supervisor:	Dr. F. Messali	TU Delft
Thesis committee:	Prof.dr.ir. J.G. Rots	TU Delft
	Dr.ir. G.J.P. Ravenshorst	TU Delft
	Dr.ir. M.A.N. Hendriks	TU Delft

TUDelft

Delft University of Technology

PREFACE

This report is submitted in partial fulfilment of the requirements for the degree of Master of Science in Civil Engineering, track Structural Engineering, specialisation Structural Mechanics at the Technical University of Delft. The work has been performed at the Structural Engineering department, currently engaging in research in the fields of novel computational and analytical techniques to develop more reliable, efficient and effective methods to analyse existing masonry structures. In line with this trend this work reports an investigation into the behaviour of an equivalent frame model, adopting beam finite elements available in the finite element software TNO DIANA.

ABSTRACT

Existing sophisticated numerical micro- and macro models have already proven to be capable of simulating typical masonry behaviour. However, assessing the global response of masonry buildings using brick-to-brick micro modelling or even simplified macro modelling, in which masonry is regarded as a continuum material, takes such an amount of time that these methods cannot be considered as cost-effective. For the last two decades it has been recognized that, for the global structural behaviour of masonry buildings, simplifications have to be made. The idealization of a masonry wall as an assemblage of numerically integrated (or fibre) beam elements could considerably reduce the computational burden and therefore this study addresses the following research question:

To what extent are numerically integrated beam elements applicable for assessing the global response of masonry structures?

Whereas existing equivalent frame methods are usually based on lumped plasticity models, the approach discussed here considers the entire member (e.g pier or spandrel) as an inelastic element in which the sectional response is evaluated via a fibre discretization in which each fibre (or integration point over the depth) may follow a material uniaxial nonlinear stress-strain relation. Initially the shear response is kept linear, automatically idealizing the structural response as purely flexural. The proposed model will be hereinafter named FFM (Fibre Flexure Model). Additionally, an extension of the FFM has been proposed, describing the shearing behaviour by means of a structural nodal interface element. Adopting the nodal interface element, placed between two nodes of adjacent beam elements, the axial and bending behaviour is described with the fibre-section discretization and the shear behaviour is modelled via an equivalent Coulomb-type criterion describing the shear force limit. The proposed model will be hereinafter named FF-LSM (Fibre Flexure – Lumped Shear model) because it lumps shearing nonlinearities in one single interface element located in the centre of the structural component, whereas flexural and crushing behaviour is evaluated via smeared crack beam elements.

To validate the numerical models, two different types of benchmarks have been investigated, respectively representing the behaviour of either a single structural component (masonry pier) or a composite façade. All numerical models have been subjected to static nonlinear (pushover) analyses and results have been compared with experimental and numerical data through the use of a reference continuum model.

First, it has been demonstrated that the FFM, idealizing the structural response as purely flexural, is capable of simulating the rocking failure mode of unreinforced masonry walls, whereas it fails to simulate typical masonry shearing modes such as diagonal cracking and sliding. The use of the model for squat members that are characterized by shear failure leads to significant overpredictions, making the model not applicable for the analysis of masonry structures containing relatively squat structural components, having shear span to depth ratios less than approximately 1.

Second, the shortcoming of the FFM regarding the shearing failure mode has been overcome by combining the numerically integrated beam elements with a structural nodal interface element describing the shear behaviour. The FF-LSM including the nodal interface is able to correctly predict the shear capacity of both slender and squat walls, although the observed level of accuracy depends largely on the adopted shear failure criterion. Various shear force criteria (Coulomb friction based) have been considered: the Mann and Muller (1982) criterion, the correction proposed by Magenes and Calvi (1997) and the modification according to Abrams (1992). Generally it was observed that the criteria developed by Abrams (1992) was the most accurate and that especially for a decreasing shear ratio the criterion developed by Magenes and Calvi (1997) appeared to be less precise.

Third, analysing a composite façade, with respect to the reference continuum model the FFM and FF-LSM significantly reduce the number of elements, nodes and integration points, consequently minimizing the computational effort and maximizing the computational robustness. In comparison with the corresponding continuum model the computational time decreases by a factor of approximately 10. Despite the limitations of the FFM regarding the shearing failure mode, the model shows an acceptable accuracy in terms of initial stiffness, stiffness reduction and peak strength. Adopting the FF-LSM the numerical model predictions were significantly enhanced and both flexural and shearing failure modes (in piers and spandrels) were detected correctly. Therefore, the result of the investigation has proved to be very promising as with the FF-LSM an acceptable balance between computational cost and accuracy is found, applicable to the global analysis of two dimensional masonry structures constituting slender as well as squat walls. As many problems in engineering practice require solutions in three-dimensional space, a fully three-dimensional extension of the FF-LSM is highly recommended.

TABLE OF CONTENT

LIST OF FIGURES

LIST OF TABLES

1 INTRODUCTION

For the last two decades the earthquakes caused by the gas extraction in the province of Groningen have been increasing both in frequency and intensity. The buildings are not designed to survive the significant horizontal earthquake forces caused by the horizontal accelerations and consequently, if these buildings are examined according to the conservative linear-elastic approach adopted in the past, most buildings would fail. Currently, Finite Element (FEM) calculations are being done in order to verify whether these buildings can withstand the horizontal earthquake forces. In most cases, this involves nonlinear calculations related to crack propagation in order to make use of the full capacity of the material or the structure. In the past very accurate non-linear computational strategies have been developed, e.g. simplified micro-models (interface model) and macro models (smeared crack model), which show the ability to simulate the pre- and post-peak behaviour of brick masonry walls. One disadvantage of these two approaches is that they are time consuming and require big data storage systems. For this reason, this study focuses on modelling techniques which can reduce the computational complexity significantly and consequently make the assessment of the global response easier than before.

1.1 The research problem

Currently, numerical simulations are one of the most powerful tools to provide insight into the structural behaviour of masonry buildings. Therefore, examining the structural reliability of existing buildings under new loading conditions requires both reliable and cost-effective numerical models for their structural assessment. Existing sophisticated numerical micro- and macro-models have already proven to be capable of simulating typical masonry properties including the anisotropy, softening behaviour after cracking and dilatancy. However, when the global response masonry buildings is assessed, even the use of numerical macro models (in which the interaction between unit and mortar is neglected) takes such an amount of time that these methods cannot be considered as cost-effective. Besides, also convergence stability is often an issue for these models. For this reason it is important to develop or extend existing theories in which the computational effort is reduced. One suggestion is to reduce the number of nodes and integration points by using series of fibre (or numerically integrated) beam elements representing the structural components of a masonry wall (e.g. piers and spandrels). Observing that the stress situation in beams is a special case of a plane stress situation, the same smeared crack concept used for plane-stress/plane strain and shell elements in current

investigations may be applied. However, the question is whether these numerically integrated beam elements are capable of simulating the complex failure mechanisms that masonry walls exhibit.

1.2 The objectives of the study

In this paper the attention is focused on the application of numerically integrated beam elements in unreinforced masonry walls. It aims at developing a reliable way of numerical modelling that can determine the global response of a masonry structure but at the same time may limit the computational burden. To provide essential information about stiffness, displacement capacity and ultimate strength, a set of benchmarks will be investigated via a static-nonlinear analysis method (pushover). Besides, to validate the behaviour of the beam elements, a comparison will be made using plane stress elements which already have proven to be in good agreement with experiments. In both approaches the same constitutive model will be adopted, in order to represent the nonlinear material behaviour of masonry. The beam- and continuum model will be compared in terms of performance at detecting the principal failure modes, accuracy and computational effort.

In order to define the capability of fibre beam elements to properly represent the structural behaviour of a masonry structure, a number of steps are required.

Initially, the discussion starts at a structural component level, focusing on the in-plane behaviour of masonry walls. Consequently, the structural components (e.g. piers and spandrels) will be replaced by series of numerically integrated beam elements. A dimensional variation analysis will be performed in order to determine the capability of the beam elements of simulating the principal failure modes of masonry piers and spandrels. Then, the structural behaviour of complete masonry façades will be simulated. The application of beam elements to model complex masonry façades involves some limitations and problems regarding an accurate representation of the single structural components which compose the façade. Therefore, in the second stage of this investigation, a masonry wall with regular distributed openings will be analysed and numerical and experimental results will be compared. Finally, to provide greater insight into the behaviour of such models, different types of sensitivity analyses will be performed and model uncertainties will be discussed.

1.3 Research question

For the last two decades it has been recognized that, for the global structural behaviour of masonry, simplifications have to be made. Often, these efforts have been directed to the development of simple constitutive models. Until now, this approach has mainly been used to model masonry structures with plane-stress, plane-strain, shell and solid elements. However, the use of these types of elements requires a considerable amount of nodes and integration points which causes a significantly high computational effort. The idealization of a masonry wall as an assemblage of beam elements could considerably reduce the computational burden and therefore this study address the following research question:

To what extent are numerically integrated beam elements applicable for assessing the global response of masonry structures?

2 REVIEW OF THE LITERATURE

This chapter presents a wide-ranging literature review of research results that are necessary for a basic understanding of the complex masonry behaviour. First a description of the mechanical properties on micro- and macro-level will be presented. Second, the masonry behaviour on a structural component level will be discussed, e.g. the in-plane behaviour of masonry panels under axial compressive and lateral shearing forces. Third, an extension will be made to existing computational strategies, in which the focus will be on the two most common constitutive models used in nonlinear finite element analyses of masonry structures. Finally, the most important features of the equivalent frame method will be discussed.

2.1 Mechanical Properties of Masonry

As mentioned in the introduction, the material description of masonry depends on the type of modelling, i.e. micro-modelling of the individual components or macro-modelling of masonry as a composite. For this reason the first part of section 2.1 deals with the mechanical properties related to the single components of masonry and the second part describes masonry as being a composite material. Especially the latter takes into account the anisotropic behaviour of masonry caused by the geometry of the joints.

2.1.1 Mechanical properties of unit and mortar

The mechanical properties of masonry are strongly related to the mechanical properties of the individual components. In the past, several authors used uniaxial compressive tests to examine the strength, stiffness and deformation capacity of masonry. McNary and Abrams (1985) carried out an experimental investigation and examined the response of a stack of bricks bonded with mortar loaded by a compressive axial force (Figure 2-1a). Based on the work of Hilsdorf (1969) they explained that in such a compressive strength test the mortar expands laterally more than the brick. Since brick and mortar are connected mechanically and chemically, shear stresses at the unit-mortar interface produce triaxial compression in the mortar and bilateral tension in the brick (Figure 2-1b). Based on this information McNary and Abrams (1985) performed triaxial compression tests of mortar under a range of lateral confining stresses, biaxial tests of bricks to determine the splitting strength and uniaxial compression tests of stack-bond prisms. The latter is discussed in section 2.1.3, since it is related to the composite behaviour of masonry.
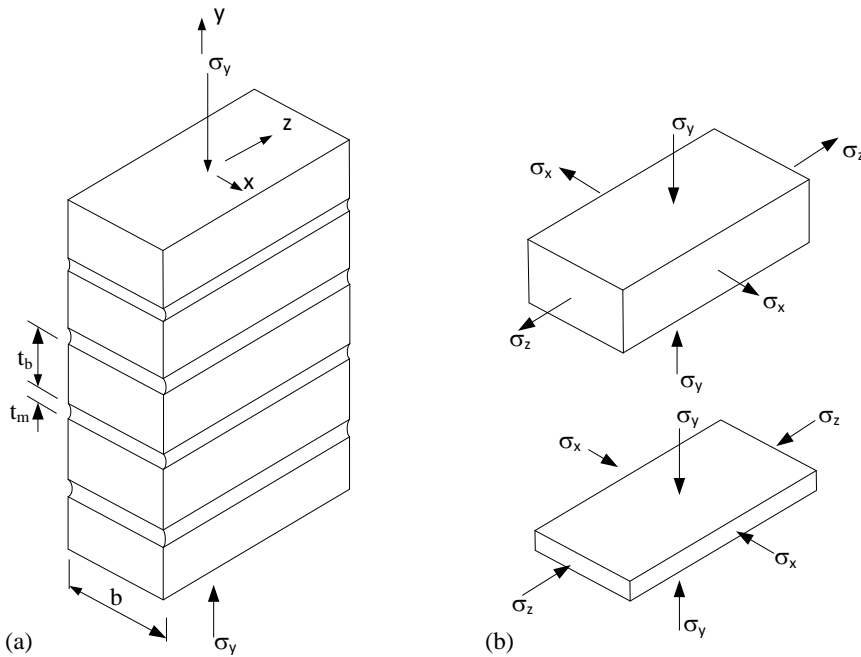
Figure 2-1Prism subjected to vertical compressive force (a); Stress states for brick and mortar elements (b) (McNary & Abrams, 1985).

By performing these tests it was shown that the mortar behaviour displayed a nonlinear stress-strain behaviour and was influenced by the confining pressure (Figure 2-2a).
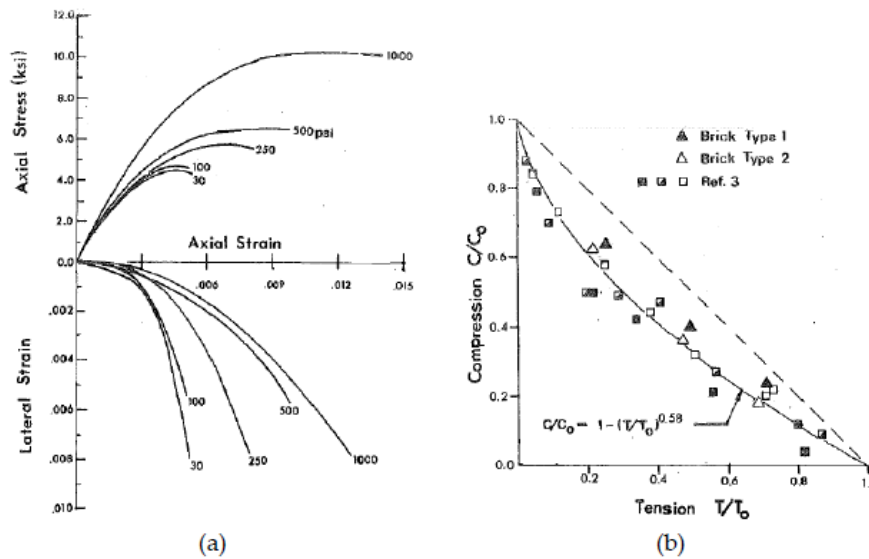
Figure 2-2Measured properties of mortar under a range of different confining stresses (a) and biaxial interaction diagram for brick specimens (b) with C_0 and T_0 being equal to f_b and f_{bt}, respectively. (McNary & Abrams, 1985).

Furthermore, testing brick units subjected to lateral tension and compressive axial pressure it was proven that the failure criterion for bricks under triaxial stresses proposed by Hilsdorf (1969) is rather accurate since an almost linear relation between the compressive strength and the biaxial tension stress was shown (Figure 2-2b). The straight line corresponding to the failure criterion of brick can be expressed as:

$$\frac{C}{f_b} = 1 - \frac{T}{f_{bt}} \qquad\qquad (2.1)$$

in which f_b is the uniaxial compressive strength, f_{bt} the direct tensile strength of brick, C the compressive stress in the brick and T the tensile stress in the brick. A trend line that best represents the data found by McNary and Abrams (1985) can be expressed using the equation:

$$\frac{C}{f_b} = 1 - \left(\frac{T}{f_{bt}}\right)^{0.58} \qquad\qquad (2.2)$$

2.1.2 Mechanical properties of the unit-mortar interface

Tests performed on masonry specimens have shown that the interface between unit and mortar can act as a plane of weakness and consequently can dominate the behaviour of masonry assemblages. Due to the low unit-mortar bond of bed and head joints, the behaviour of masonry can be characterised by a nonlinear response also at low level of load. Observing the failure modes of the unit-mortar interface two different modes can be distinguished: one related to failure due to tension normal to the interface plane (mode I: opening) and another associated with failure in shear along the mortar joint (mode II: in-plane shear) (Lourenco, 1996).

2.1.2.1 Mode I failure

Two types of bond between mortar and brick units can be identified: a chemical and a friction/mechanical bond, which play a major role in influencing the two different failure modes mentioned above. The tensile strength at the interface is mainly determined by the chemical bond. Van der Pluijm (1992) has provided results on the tensile bond strength and the fracture energy needed to create a unitary area of a crack. Results obtained from these tests showed an exponential relationship between the tensile bond strength and the crack width. Furthermore, very low fraction energies were detected, ranging from 0.005 to 0.2 [Nmm/mm^2] for tensile bond strengths varying from 0.3 to 0.9 [N/mm^2] (Lourenco, 1996). Additionally, by analysing the cracked specimens, it was discovered that the net bond surface of the specimens was approximately equal to 35% of the initial cross sectional area of the specimen.

2.1.2.2 Mode II failure

The Mode II failure is associated with the shear behaviour of the unit-mortar interface. In contrast with the tensile bond strength, the shear strength at the interface is caused by both the

chemical bond and friction between the surfaces of brick and mortar respectively. Again, experimental results showed an exponential softening stress-strain relationship, but after the peak strength a residual dry friction level is obtained (Van der Pluijm, 1993). Another factor influencing the peak strength and residual dry friction level is the confining (compressive) stress. The relation between this confining pressure, the peak and residual dry friction strength can be described with a Mohr-Coulomb friction model, in which the material parameters are described as the initial internal friction angel ϕ_0, the initial cohesion c and the residual internal friction angle ϕ_r. It should be noted that the residual dry friction strength is only influenced by the residual internal friction angle ϕ_r, since after reaching the peak strength the cohesion has disappeared (Figure 2-3).
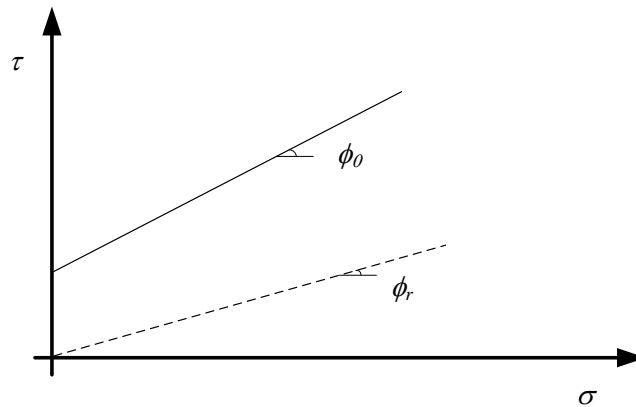
Figure 2-3 The Coulomb friction model for both the peak and residual friction strength.

2.1.3 Mechanical properties of the composite material

In the last section the mechanical properties of the individual components of masonry were analysed. Since masonry can be seen as a composite material, several laboratory tests were performed to examine the uniaxial and biaxial behaviour of masonry as a composite. This section will explain first the uniaxial tensile behaviour and second the biaxial behaviour of masonry.

2.1.3.1 Uniaxial behaviour

To determine the uniaxial behaviour of masonry, many investigators of masonry started with the simplest case, namely that of a compressive test of stack-bond masonry prisms (Atkinson et al., 1985; Hilsdorf, 1969; McNary & Abrams, 1985). As mentioned above, Hilsdorf (1969) demonstrated that failure of masonry prisms can be explained by the differences in the elastic properties of unit and mortar. However, his assumption that the mortar is at its failure state (point D in Figure 2-4) at the moment of collapse was incorrect (Atkinson et al., 1985).

Proven by experimental results it is mainly the nonlinear behaviour of the mortar that influences the strength level at masonry failure (Atkinson et al., 1985). Considering nonlinear mortar properties, failure of the stack-bond prism occurs when the stress curve of the brick intersects the brick failure envelope at point E (Figure 2-4). Therefore, the prism strength is determined by the splitting strength of the brick and the deformation capacity of the mortar, rather than its crushing strength. The latter explains the nonlinearity of the stress-strain relations till failure is reached. Atkinson et al. (1985) developed a theory to account for the nonlinear behaviour of the mortar, using a compatibility argument that the strains existing in the brick and mortar must be the same. The following equation was proposed:

$$\Delta \sigma_{x_b} = \frac{\Delta \sigma_y [\nu_b - \dfrac{E_b}{E_m(\sigma_1, \sigma_3)} \nu_m(\sigma_1, \sigma_3)]}{1 + \dfrac{E_b}{E_m(\sigma_1, \sigma_3)} \dfrac{t_b}{t_m}} \tag{2.3}$$

in which $\Delta \sigma_{x_b}$ represents the increment of lateral stress in the brick as a result of an increase in compressive stress $\Delta \sigma_y$; ν_b and E_b are the Poisson's ratio and the Young's modulus of the brick; $\nu_m(\sigma_1, \sigma_3)$ and $E_m(\sigma_1, \sigma_3)$ are the Poisson's ratio and the Young's modulus of the mortar as functions of the principal stresses; t_b and t_m are the thicknesses of the brick and the mortar respectively.
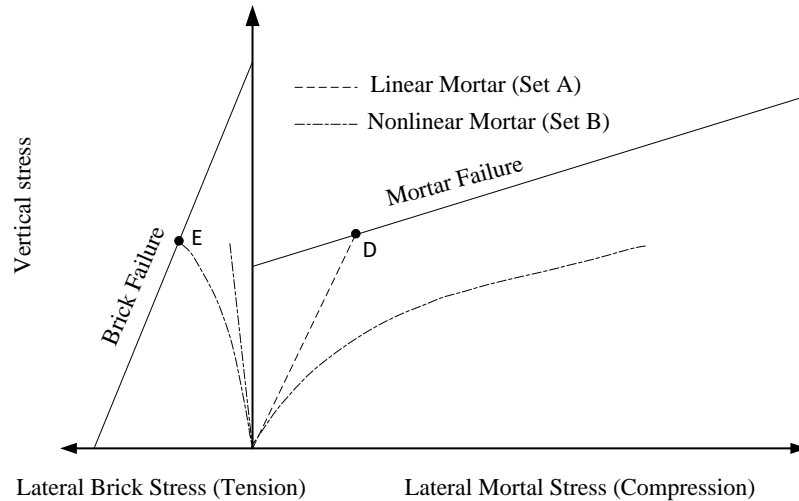
Figure 2-4 Stress paths for brick and mortar taking into account linear and nonlinear mortar properties (McNary & Abrams, 1985).

2.1.3.2 Biaxial behaviour

As previously stated, masonry is an anisotropic material; therefore, its mechanical properties vary with respect to the direction from which they are measured. Almost every structural

component subjected to in-plane loads experiences a biaxial state of stress and therefore many authors have tried to characterize the biaxial behaviour of masonry by means of laboratory tests. As mentioned above, the failure envelope of masonry cannot be defined by the principal stresses only, but the orientation of the bed joints with respect to the principal directions must also be taken into account. Page (1982) performed many tests on masonry panels with varying principal stresses (compression-compression, tension-tension, compression-tension) and bed joint orientations ranging from $\theta = 0°$ to $\theta = 90°$. A complete overview of the experimental results is reported by Page (1981, 1982). The failure surface for brickwork under biaxial compressive stress, created by plotting the line of best fit for each bed joint orientation, is given in Figure 2-6a. The figure shows clearly that most strength values are dominated by the magnitude of both principal directions and that the inclination of the bed joints is of little influence. This can be explained by the fact that a splitting failure occurred, parallel to the free surface and independently of the bed joint orientation (Figure 2-5b). However, the orientation of the bed joints has a significant influence if one of the principal stresses decreases to zero (Figure 2-6a). This phenomena can be explained observing the modes of failure and has mainly to do with the fact that for inclinations bigger than $\theta = 0°$ failure occurs by sliding of the bed joints (Figure 2-5a). Another observation that can be made from the experimental data obtained by Page (1982), is that in contrast with the biaxial compression tests, the biaxial tension-compression and tension-tension tests exhibit a strong dependency on the inclination of the bed joints for all principal stress values Figure 2-6b. In this case failure always originates from the cross-sections normal to the free surface, which clarifies the significant influence of the bed joint orientation.

$\theta = 0°, \sigma_2 = 0$ $\theta = 30°, \sigma_2 = 0$ $\theta = 90°, \sigma_2 = 0$

(a)   (b)
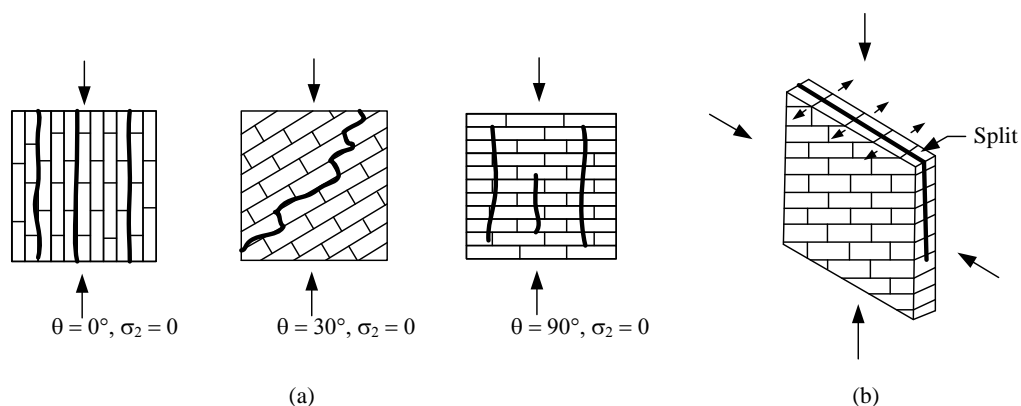
Figure 2-5Failure modes for uniaxial compression (a) and biaxial compression (b) (Page, 1982).
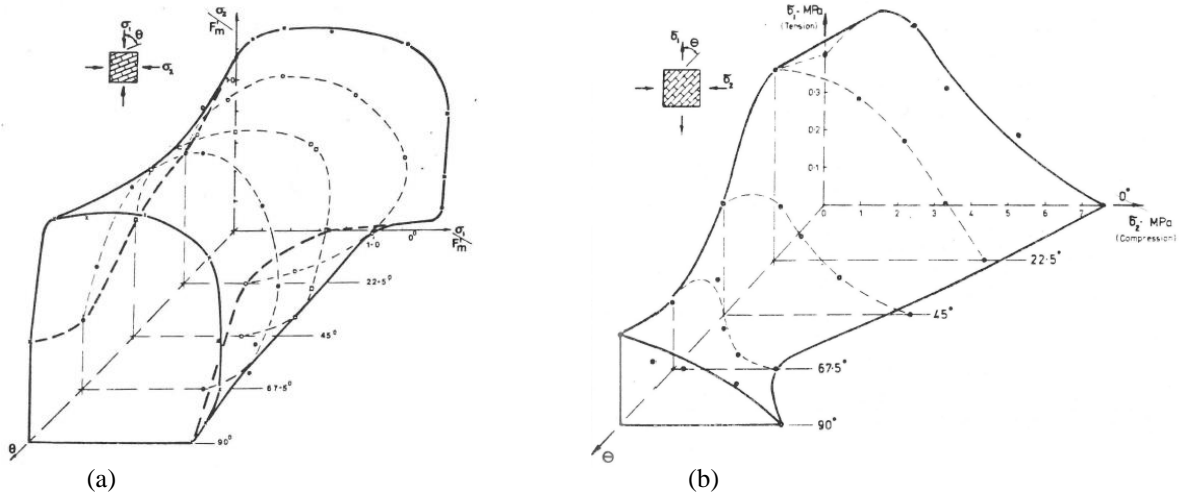
Figure 2-6Failure surface for masonry under biaxial compressive stress (a) and biaxial tensile-compressive stress (b) (Page, 1982).

2.2 In Plane Response of Brick Masonry Walls

When Unreinforced Masonry (URM) buildings are well designed and the out-of-plane failure of masonry walls is prevented in an appropriate manner, the in-plane walls provide the lateral resistance of a building. Observing the seismic response of in-plane masonry walls with openings, in general two main structural components may be distinguished, namely piers and spandrels. Piers are the vertical resistant components left by the openings and the horizontal elements coupling the response of adjacent piers under horizontal action are called spandrels. In this chapter the in-plane behaviour of masonry walls subjected to axial and lateral forces will be analysed, representing the gravity and the horizontal earthquake forces respectively.

2.2.1 Strength of masonry piers

The failure mechanisms of masonry piers subjected to gravity and seismic action can be traced back to three principal failure mechanisms and can be summarized as follows:

1. Rocking failure: due to an increase in horizontal action the bed joints crack in tension and consequently the lateral force must be carried by the masonry in the compression zone. Failure can take place in any of the two following ways or simultaneously: overturning of the wall and crushing of the compressed toes (Figure 2-7a).

2. Sliding: due to the flexural response of the panel, horizontal tensile cracks form at bed joints-units interface. In case of low friction coefficients and low vertical loads a sliding plane along these cracked bed joints can develop (Figure 2-7b).

3. Shear cracking: depending on the properties of the unit-mortar interface, mortar and units, shear loads can form an inclined diagonal crack following the path of bed- and head joints (zigzag pattern) or throughout bricks (Figure 2-7c).

(a)   (b)   (c)
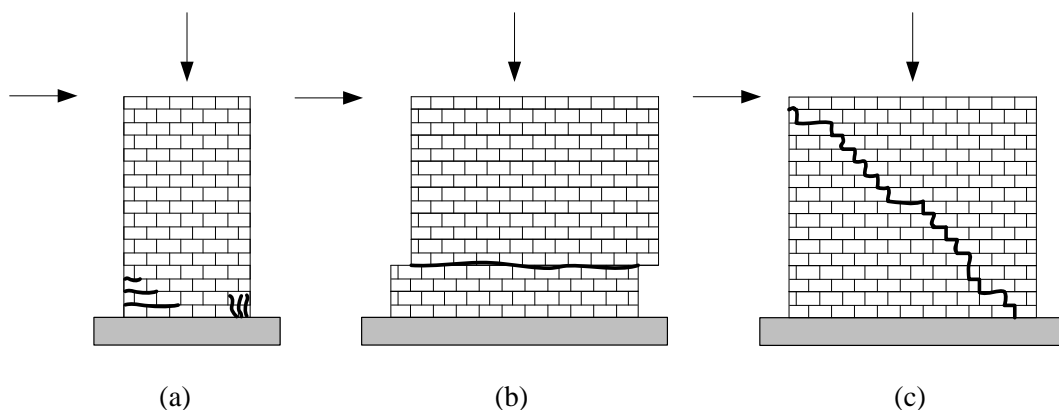
Figure 2-7 Mechanisms of lateral force resistance: rocking (a), shear sliding (b) and diagonal cracking (c) (Messali, 2015).

Since sliding and shear cracking are both associated with shear behaviour, this section will deal first with the rocking strength and second with the models and parameters for the shear strength prediction.

2.2.1.1 Rocking strength

For the last two or three decades, several authors have tried to describe the resistance of the failure modes mentioned above. Most of them are based on a simplified strength assessment and ignore for example the tensile strength of the bed joints. Magenes and Calvi (1997) have discussed possible approaches to assess the rocking strength of masonry walls. By using numerical simulations, which allow changes in boundary conditions easily, they observed that the dominating factor on the shear strength is the shear ratio $\alpha_v = M / VD$. Based on equilibrium, neglecting the tensile strength of the bed joints and assuming a simplified stress distribution at the toe (Figure 2-8), they derived a simple expression to determine the strength associated to rocking failure:

$$V_r = \frac{M}{H_0} = \frac{D^2 t}{H_0} \frac{p}{2} \left(1 - \frac{p}{\kappa f_u} \right) \tag{2.4}$$

where M is the moment resistance, H_0 is the effective pier height (distance from zero moment), D and t are the width and the pier thickness respectively, p is the mean vertical stress due to the axial load P, f_u is the masonry compressive strength and κ reflects the simplified vertical stress distribution at the toe. The elegance of the expression lies in the fact that H_0 is determined by the boundary conditions and can be related to the shear ratio:

$$\alpha_v = \frac{M}{VD} = \frac{VH_0}{VD} = \frac{H_0}{D} \tag{2.5}$$
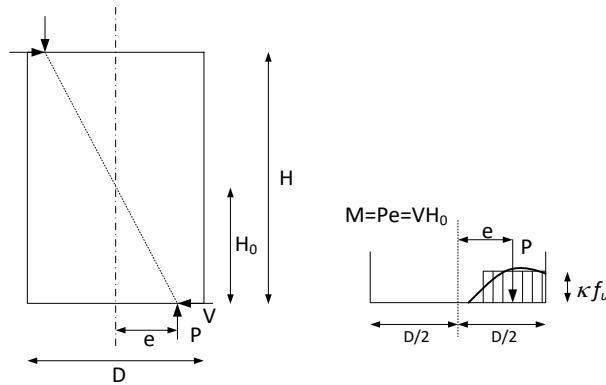
Figure 2-8 Assumptions for rocking strength evaluation of a wall failing with crushing at the base corner (Magenes & Calvi, 1997).

13

2.2.1.2 Shear strength

There are many simplified approaches available to estimate the shear resistance of masonry walls. Roughly the models can be divided into two categories: those who consider masonry as being an equivalent isotropic material (Turnšek & Cacovic, 1971; Turnšek & Shepherd, 1980), and those who describe masonry as a composite material (Mann & Müller , 1982). The two approaches mainly differ in the choice of reference stress (e.g. shear, normal or principal stress) and of a reference section where failure is initiated.

2.2.1.2.1 Mohr-Coulomb Criterion

To estimate the resistance of a shear wall associated with diagonal cracking, several authors related the shear failure to the ultimate shear stress based on the Mohr-Coulomb formulation:

$$\tau_u = c + \mu \sigma_v \tag{2.6}$$

The formula can be physically justified, since often diagonal cracking is initiated by sliding of bed- joints. If τ_u is considered as the average ultimate shear stress in a horizontal section of the wall and σ_v is assumed to be the mean vertical stress in the pier, the expression becomes:

$$V_d = Dt\tau_u = Dt(c + \mu p) = Dt(c + \mu \frac{P}{Dt}) \tag{2.7}$$

2.2.1.2.2 Mann and Müller's Theory

Based on equilibrium considerations, Mann and Müller (1982) developed a complete failure envelope in which the strength parameters of the Mohr-Coulomb criterion are corrected. Focusing on the diagonal cracking failure mode, this theory describes the crack propagation along the constituting components (i.e. joints and units) of a masonry wall. Observing a small specimen (Figure 2-9) and making use of the superposition principle the following assumptions were made:

- The axial compressive stress σ_v and the shear stress τ acting on the masonry panel are uniformly distributed over the cross section.
- Considering that in most cases the head joints are not completely filled with mortar and assuming that stresses perpendicular to the head joints are negligible, it can be concluded that no shear stresses can develop in the head joints.
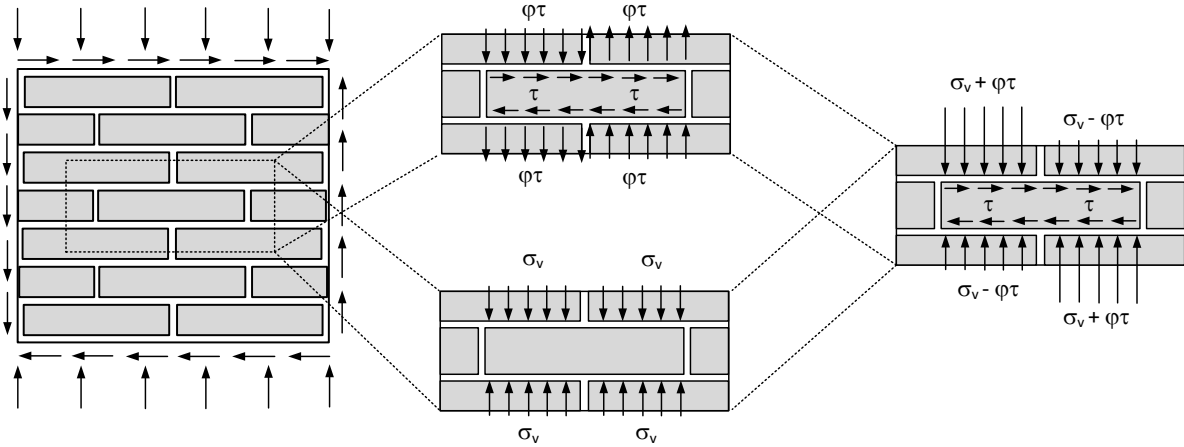
Figure 2-9 Stress state on a block due to shear and compression forces (Calderini et al., 2010).

From Figure 2-9a it can be seen that developed shear stresses along the bed joints produce a couple of vertical axial compressive stresses to provide in equilibrium. Superimposing the global axial compressive stresses, this results in a modified stress distribution for the brick which can be represented by the following formula:

$$\sigma_y = \sigma_v \pm \varphi \tau_u \tag{2.8}$$

in which $\varphi = 2\Delta_y / \Delta_x$ describes the interlocking of the masonry pattern. Assuming that cracks are exerted in the parts where the axial compressive stresses are the smallest, equation (2.8) can be inserted in equation (2.6):

$$\tau_u = c + \mu \left(\sigma_v - \varphi \tau_u \right) \tag{2.9}$$

Rewriting expression (2.9) the following expression can be obtained representing a failure criterion:

$$\tau_u = \overline{c} + \overline{\mu} \sigma_v \tag{2.10}$$

where $\overline{c}$ and $\overline{\mu}$ are the corrected cohesion and friction coefficient respectively:

$$\overline{c} = \frac{c}{1 + \mu\varphi}$$
$$\overline{\mu} = \frac{\mu}{1 + \mu\varphi} \tag{2.11}$$

Since the contribution of the shear stresses along the head joints are completely neglected, equation (2.10) provides a lower bound to the real strenght of masonry. The derivation easily explains why usually a zigzag pattern is observed during diagonal cracking failure, since the brick parts where the axial compressive stress is the smallest are located diagonally opposite one another (Crisafulli, 1997). Using equation (2.8), Mann and Müller (1982) also derived an expression that accounts for failure in compression. Observing the stresses on the specimen in Figure 2-9, it can be concluded that for very high values of the axial normal force σ_v, the

greater normal stress $(\sigma_v + \varphi\tau)$ in equation (2.8) can exceed the compressive strength f_u of masonry. From equation (2.8) and assuming that $\sigma_y = f_u$ the failure criteria for compressive failure becomes:

$$\tau_c = (f_u - \sigma_v)\frac{\Delta_x}{2\Delta_y} \tag{2.12}$$

From experiments, Mann and Müller (1982) observed that diagonal cracking not only occurs due to a diagonally stepped failure of bed and head joints, but may also occur by shear-tensile cracking of the bricks. This is a result of induced tensile stresses in the brick, caused by the shear-compressive state. It may occur when medium to high values of the axial compressive stress cause an increase in the shear strength of the mortar joints. To complete the set of equations that completely describes the failure envelope of masonry, they derived a formulation for the shear-tensile cracking of bricks. Assuming that failure occurs when the principal stress in the brick exceeds the tensile strength f_{bt} of the brick, the failure criteria can be formulated using the expression for the principal stress obtained from elementary theory of elasticity:

$$\sigma_p = f_{bt} = \frac{\sigma_v}{2} + \sqrt{\left(\frac{\sigma_v}{2}\right)^2 + (k_1 k_2 \tau)^2} \tag{2.13}$$

in which σ_v is the axial normal force, k_1 is the ratio between the shear stress at the centre of the pier and the mean shear stress and k_2 is a coefficient taking into account the ratio between the shear stress applied on a block and the shear stress at its centre. It was experimentally proven that $k_1 k_2$ is equal to 2.3. Rewriting equation (2.13) the failure criteria for shear-tensile cracking of the bricks is expressed as:

$$\tau_b = \frac{f_{bt}}{2.3}\sqrt{1 + \frac{\sigma_v}{f_{bt}}} \tag{2.14}$$

Combining equations (2.10), (2.12) and (2.14), representing respectively the failure criteria for shear-friction failure τ_u, compressive failure τ_c, shear-tensile cracking of bricks τ_b and assuming that the axial compressive stress σ_v is equal to the mean vertical stress p, the failure envelope curve of Mann and Müller (1982) is described by the following three expressions:

$$\tau_u = \overline{c} + \overline{\mu}p \tag{2.15}$$

$$\tau_c = (f_u - p)\frac{\Delta_x}{2\Delta_y} \tag{2.16}$$

16

$$\tau_b = \frac{f_{bt}}{2.3}\sqrt{1+\frac{p}{f_{bt}}} \qquad (2.17)$$

Figure 2-10 includes a diagram that represents this formulae graphically and compares the created failure envelope curve of Mann and Müller (1982) with the Mohr-Coulomb friction criterion (2.6).
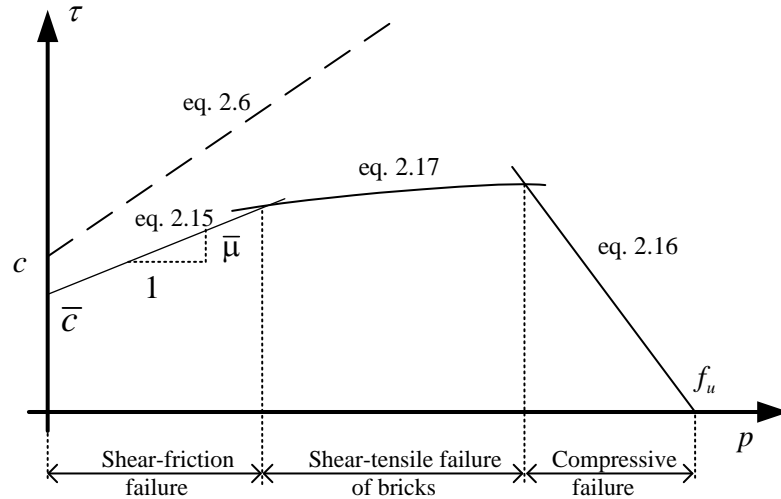
Figure 2-10 A comparison between the envelope curve for Mann and Müller's failure theory and the Coulomb criterion (Crisafulli, 1997).

Other authors (Magenes & Calvi, 1997; Abrams, 1992) take into account a reduced section length, caused by wall cracking due to flexure. Based on equilibrium, a linear compression stress distribution at the toe (Figure 2-11) and neglecting the tensile strength of the bed joints, the effective uncracked section length d is equal to:

$$d = \beta D = 3\left(\frac{1}{2} - \frac{V}{P}\alpha_v\right)D \qquad (2.18)$$
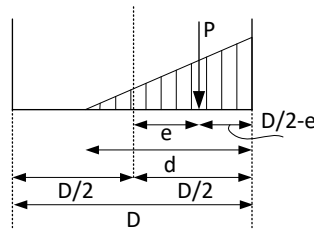
Figure 2-11Assumptions for diagonal shear strength of a wall failing with crushing at the base corner (Magenes & Calvi, 1997).

Combining expression (2.6) and (2.18) the ultimate shear force can now be calculated as:

$$V_d = \beta Dt(c + \mu p) = Dt(c + \mu\frac{p}{\beta}) = Dt\left(\frac{1.5c + \mu p}{1 + 3\alpha_v\frac{c}{p}}\right) \qquad (2.19)$$

17

Furthermore, by numerical simulation Magenes and Calvi (1997) discovered that the reciprocal of the shear strength increased linearly with the shear ratio. To account for this effect a correction factor depending linearly on the shear ratio was introduced:

$$V_d = Dt\tau_u \quad \text{with} \quad \tau_u = \min(\tau_{cs}, \tau_{cs}) \tag{2.20}$$

$$\tau_{cs} = \frac{1.5c + \mu p}{1 + 3\alpha_v \dfrac{c}{p}} \quad \rightarrow \quad \text{cracked section}$$

$$\tag{2.21}$$

$$\tau_{ws} = \frac{c + \mu p}{1 + \alpha_v} \quad \rightarrow \quad \text{whole section}$$

In both expressions presented in equation (2.21), the cohesion and friction coefficient are global strength parameters. Using local bed joint strength parameters may lead to an overestimation of the strength parameters because of the presence of weak head joints. Therefore, Magenes and Calvi (1997) have pointed out that the proposed correction of Mann and Müller (1982) for the cohesion and friction coefficients given in equation (2.11) are recommended when the expressions for the shearing strength presented in equation (2.21) are used.

2.2.1.2.3 Turnšek and Cacovic's Theory

Another approach to evaluate diagonal cracking, proposed by Turnšek and Cacovic (1971) and Turnšek and Shepherd (1980), idealises masonry as an elastic, homogeneous and isotropic continuum all the way up to failure and states that a diagonal crack is initiated when the principal stress at the centre of the wall reaches the reference tensile strength of masonry (point A in Figure 2-12).

Normal stress at A:

$$\sigma_v = \frac{P}{Dt}$$

Shear stress at A:

$$\tau_m = k_1 \frac{V}{Dt}$$
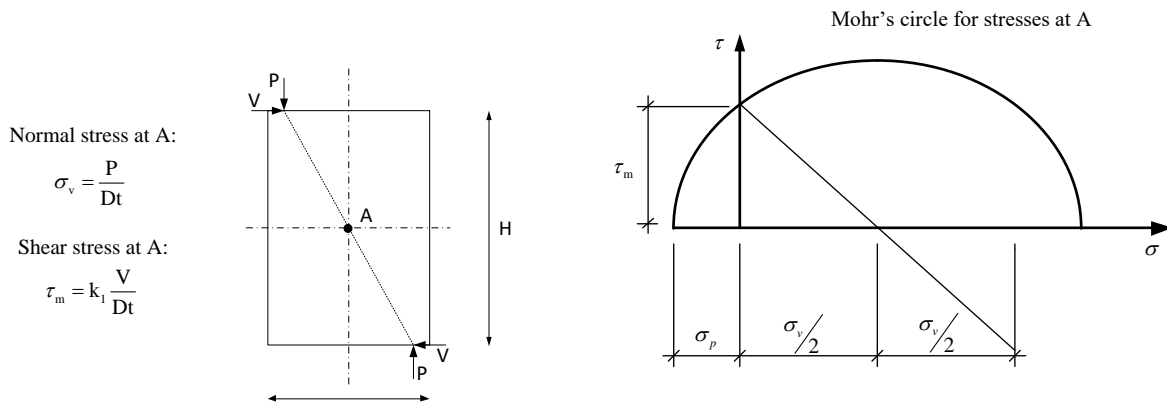
Figure 2-12 Mohr's circle for stresses at A (Turnšek and Cacovic, 1971).

The principal stress at point A is then given by the following expression:

$$\sigma_p = f_{tu} = \sqrt{\left(\frac{\sigma_v}{2}\right)^2 + (k_1 \tau)^2} - \frac{\sigma_v}{2} \tag{2.22}$$

in which σ_v is the normal stress at A, τ the shear stress at A and k_1 the shear stress distribution factor depending on the geometry. The principal tensile stress at the attained maximum resistance of the wall is often referred to as the ''tensile'' or ''reference tensile strength'' of masonry, f_{tu}. Rewriting expression (2.22) the ultimate shear force is now being calculated as:

$$V_d = Dt \frac{f_{tu}}{k_1} \sqrt{1 + \frac{\sigma_v}{f_{tu}}} \qquad (2.23)$$

By neglecting the anisotropic behaviour of masonry this approach has the advantage that the prediction of the shear strength is based on only one parameter, namely the reference tensile strength which should be obtained from experiments. As pointed out by Calderini et al. (2010), Turnšek and Cacovic's theory is generally more in line with those masonries that behave in an isotropic manner and Mann and Müller's theory with those masonries that behave anistropicallly.

2.2.2 Strength of masonry spandrels

Since masonry spandrels couple the response of adjacent piers, they are usually seen as secondary elements. According to Cattari and Lagomarsino (2008) the latter assumption cannot be justified, since a substantial energy dissipation is related to their failure. Besides, because of the fact that they act as coupling elements, their failure significantly affects the boundary conditions of piers which, in turn, influences the global response of masonry structures.

2.2.2.1 Flexural strength

To overcome the differences between expressions proposed in literature and failure mechanisms observed in laboratory experiments, Cattari and Lagomarsino (2008) derived a new formulation based on the compressive effect due to deformation of the masonry adjacent to the spandrel. In contrast to formulations in codes, which presuppose a response as an equivalent strut if the spandrel is connected with another tensile resistant element, Cattari and Lagomarsino (2008) assumed that this response may also develop as a result of the interlocking, occurring at the interface between the toe and the adjacent masonry material.

Observing a reference volume at the location mentioned, two principal failure modes can be considered, namely failure of a brick in tension Figure 2-13a and failure of the bed joints in shear Figure 2-13b.
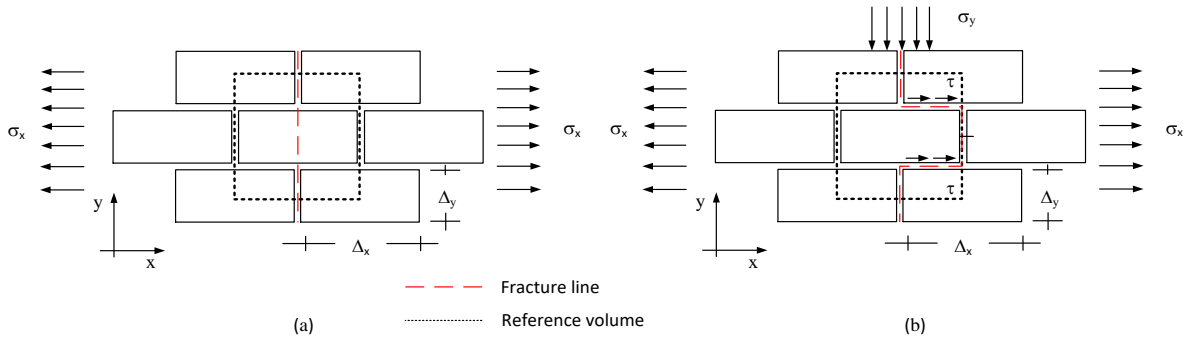
Figure 2-13Failure at the interface between the end section and the contiguous masonry material due to tensile failure of the block (a) and failure of the bed joints in shear (b) (Cattari, 2007).

Considering horizontal equilibrium (Figure 2-13a) and neglecting the thickness of the mortar joints, the following relation can be derived for brick failure in tension:

$$2\Delta_y \sigma_x = \Delta_y f_{bt} \qquad (2.24)$$

in which f_{bt} is given as the tensile strength of the brick. In case of the second failure mechanism equilibrium can only be obtained from the shear stresses developed on the horizontal bed joints since shearing stresses on the head joints should be neglected. Assuming a Mohr-Coulomb failure criterion and neglecting the contribution of the cohesion the second failure mechanism can be described as:

$$2\Delta_y \sigma_x = \tau 2 \left(\frac{\Delta_x}{2} \right) \qquad (2.25)$$

in which Δ_x and Δ_y are the block width and block height respectively, τ the shearing stress which can be presented as $\mu\sigma_y$, where σ_y is the vertical compressive stress in the spandrel. σ_y develops from a stress bulb resulting from the vertical stresses in the piers and can be expressed as a proportion of the mean vertical stress in the piers $\left(\sigma_{y;pier} \right)$:

$$\sigma_y = \gamma \cdot \sigma_{y;pier} \qquad (2.26)$$

σ_y is usually referred to as the mean clamping stress at the extreme sections of the spandrel and proposed values for γ are ranging from 0.5 (FEMA 306) to 0.65 (Cattari and Lagomarsino, 2008). Rewriting expressions (2.24) and (2.25) leads to an expression for the equivalent tensile strength, representing the properties of the spandrel element and not the masonry material:

$$f_{st} = \sigma_x = \min\left(\frac{f_{bt}}{2}, \frac{\Delta_x}{2\Delta_y} \mu\sigma_y \right) \qquad (2.27)$$

20

Using the tensile strength given in equation (2.27), the failure domain describing the flexural behaviour of the spandrel is now defined by considering a system of translational and rotational equilibrium equations. For a complete description is referred to Cattari (2007).

2.2.2.2 Shear strength

Until recently, analytical strength evaluations of the spandrel strength were hardly available, as experimental data on spandrels, required for validation, was lacking. Magenes and Della Fontana (1998) were the first to propose a model estimating the shear strength of masonry spandrels based on a Mohr-Coulomb friction criterion:

$$V_s = h_{sp} t_{sp} c \tag{2.28}$$

Following the same line of reasoning and assuming that the shear stress distribution is parabolic over the height of the spandrel (i.e. elastic and homogeneous properties), Beyer (2012) introduced a similar expression for shear crack initiation of the spandrel:

$$V_{cr,s} = \frac{2}{3} h_{sp} t_{sp} \tau_u \tag{2.29}$$

in which τ_u is given as the maximum shear stress at the spandrel axis (i.e. centre of the section). Typically shear cracking is initiated at midspan of the spandrel, since the vertical stresses at this section are generally smaller resulting in a lower shear resistance. Assuming that the cracking onset takes place in the bed joints τ_u is defined as:

$$\tau_u = c + \mu \cdot \gamma_0 \cdot \sigma_{y;pier} \tag{2.30}$$

where γ_0 referrers to the section were the vertical compressive stress in the spandrel (2.26) is the smallest. It is commonly assumed that the vertical stresses on the bed joints at midspan are approximately zero $\left(\gamma_0 = 0 \right)$ and therefore, equation (2.29) can be presented as:

$$V_{cr,s} = \frac{2}{3} c h_{sp} t_{sp} \tag{2.31}$$

However, Beyer (2012) has pointed out that for the peak strength it should be considered that cracks through head- and bed joints result into a formation of cracks over the total height of the spandrel. Therefore, the peak strength is also associated with the axial force in the spandrel and is evaluated as a function of the head joint properties:

$$V_{d,s1} = \frac{2}{3} \left(c + \mu p_{sp} \right) h_{sp} t_{sp} \tag{2.32}$$

In addition, if shear failure causes tensile cracking of the bricks, the ultimate shear resistance of the spandrel may be evaluated similar to the strength criteria adopted for piers (2.14):

$$V_{d,s2} = h_{sp}t_{sp}\frac{f_{bt}}{2.3(1+\alpha_v)}\sqrt{1+\frac{p_{sp}}{f_{bt}}} \qquad (2.33)$$

in which f_{bt} is the direct tensile strength of bricks and $\alpha_v = l_{sp}/2h_{sp}$ the shear ratio of the spandrel. It should be noted that the axial stress present in the spandrel p_{sp} is significantly affected by the stiffness of the lintel (or masonry arch) and is therefore rather difficult to predict. Besides, compared to the experimental results of spandrels, Beyer and Mangalathu (2013) showed that although the residual strength seems to be dependent on the axial force in the spandrel, equation (2.31) gives remarkable good predictions of the residual strength of spandrels. These contradictory findings are the reason why the behaviour of spandrels is still not completely understood and is part of on-going research.

2.3 Computational Strategies

As presented in Figure 2-14a masonry is a composite material consisting of units (brick, block, etc.) and mortar. Depending on the field of application, the numerical representation relates to the representation of joints by continuum elements (Figure 2-14b), joints are modelled with discontinuum elements (Figure 2-14c) or the joints, the mortar and the unit-mortar interface are smeared out in the continuum (Figure 2-14d). In this section the last two approaches, which are the most common ones in engineering practice, will be discussed with respect to the constitutive models used, accuracy and computational effort. Finally, a macro-element model will be briefly introduced and the most important features of the macro-elements adopted in that study will be explained.
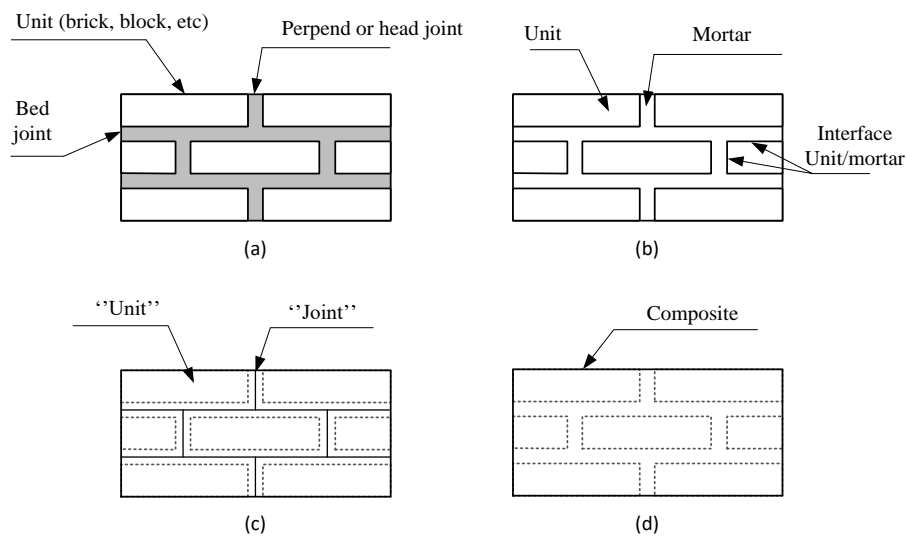
Figure 2-14Modeling strategies for masonry structures: a masonry sample (a), detailed micro modelling (b), simplified micro modelling (c), macro modelling (d) (Lourenco, 1996).

2.3.1 Micro-Modelling: a composite interface model

In general, using the concept of predefined locations of potential cracking, micro-modelling strategies pursue the aim of representing all local failure modes that can initiate a macro-level failure system. Therefore, a micro-model for masonry should be able to simulate the following local failure modes: tensile bond failure, shear bond failure, cracking of the units in uniaxial tension, diagonal tension cracking of the units due to developed friction in the joints and crushing of the masonry (Lourenco, 1996). To consider all failure modes in the model, usually the approach is to concentrate all the damage in the joints and in a potential fracture line oriented vertically in the middle of each unit (Figure 2-15). The vertical fracture lines represent the local failure mode that is associated with uniaxial tensile cracking of the unit and are able reproduce cracks that propagate from head joint to head joint right through the brick. In this way, the failure criterion of the joints has to include all other failure modes that are mentioned above.
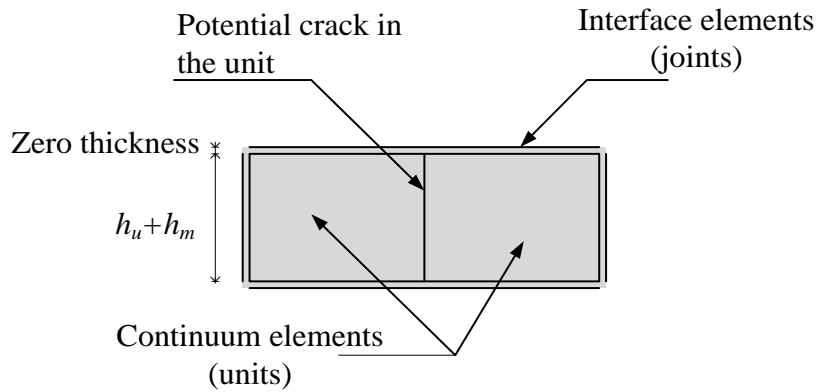
Figure 2-15Micro-modelling strategy: the potential crack in the unit and the mortar joints are modelled with zero-thickness interface elements and the units are modelled with continuum elements (Lourenco, 1996).

In finite element analysis, the mentioned approach can be achieved by using nonlinear discontinuum elements (interface elements) located at the joints and linear elastic continuum elements for the bricks (Figure 2-15). The interface element relates the normal traction s_n and the shear traction s_t to the relative normal displacement Δu_n and the relative shear displacement Δu_t across the interface:

$$\begin{bmatrix} s_n \\ s_t \end{bmatrix} = \begin{bmatrix} D_n & 0 \\ 0 & D_t \end{bmatrix} \begin{bmatrix} \Delta u_n \\ \Delta u_t \end{bmatrix} \tag{2.34}$$

The initial stiffness of the elements is equal to the elastic normal and shear moduli of the joints: $D_n = E_j / t_j$ $D_t = E_j / (2(1+\nu_j))t_j$. Once the condition of crack initiation is violated, i.e.

when the normal traction exceeds the tensile bond strength, the element stiffness changes according to a constitutive model for the crack. In general, for masonry, softening models are adopted to represent the effect that both the tensile and shear stresses do not drop suddenly to zero (elastic-brittle), but decrease gradually as the crack opening displacement increases. As presented in section 2.1.2, the failure criteria related to tensile bond failure (Mode I) can be incorporated using a tension cut-off criterion in which the softening is controlled by the tensile strength f_t, the shape of the diagram and the fracture energy G_f (Figure 2-16a). The failure mode that is associated with shear bond failure can be modelled with a Coulomb friction model (section 2.1.2) in which the softening is influenced by the cohesion c, the shape of the diagram and the fracture energy G_f^{II} (Figure 2-16b). According to Lourenco (1996), the diagonal tensile cracking of the units and the crushing of the masonry can be included by adopting a compressive cap that limits the combination of compressive and shear stresses. The parameters associated with crushing in pure compression are the compressive strength f_c, the shape of the diagram and the fracture energy G_c (Figure 2-16c). c).
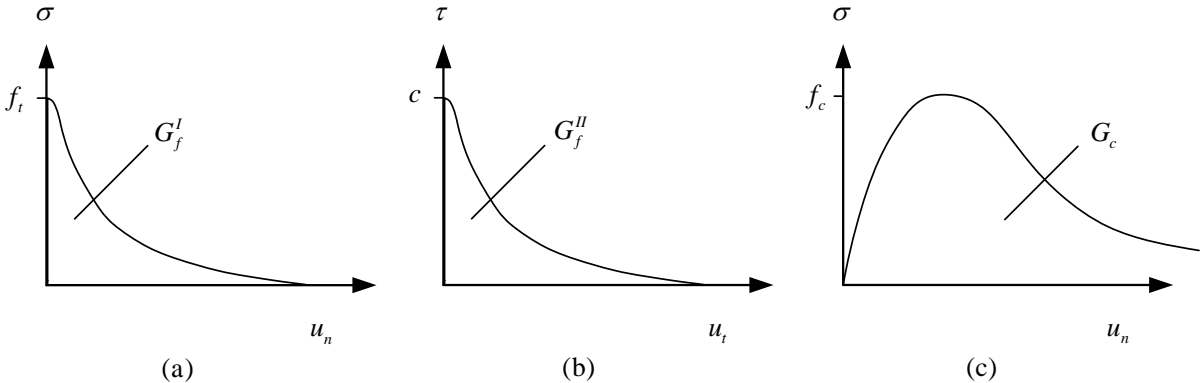
Figure 2-16 Softening relations: mode I tensile softening (a), mode II shear modulus (b),uniaxial compression softening (c).

Combining the three failure modes, a composite failure envelope can be derived that represents the effect that during the nonlinear stage, the stresses are bounded by the failure criteria that the interface represents, i.e. tensile/shear bond failure, diagonal tension cracking of the joint and crushing of the masonry (Figure 2-17). The softening behaviour of masonry is depicted as a shrinkage of the yield surface.
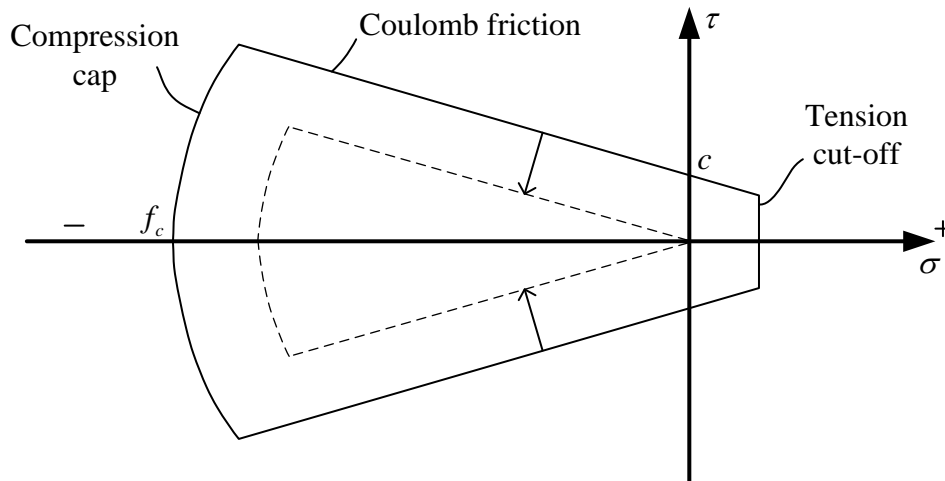
Figure 2-17A composite yield criterion for the interfaces, proposed by Lourenco (1996).

It should be noted that in this interface model accuracy is lost, since the Poisson's ratio effect for the mortar is not included. This can be explained by the fact that the behaviour of the mortar joints and the unit-mortar interface is lumped in zero-thickness discontinuous elements.

2.3.2 Macro-Modelling: an anisotropic continuum model

In the finite element analysis of concrete structures, it has been recognized that the discrete crack approach is not a sound numerical procedure to handle crack propagation in practical applications (Borst & Nauta, 1985). For this reason, researchers developed the smeared crack concept, in which the cracked concrete is modelled as a continuum. For the analysis of the global response of masonry structures it is also not feasible to make a distinction between the unit-mortar interface and the units. For this reason researchers (Rots, 1991) recognized the need for an anisotropic continuum model and extended the smeared crack concept to masonry. In this models, before cracking and depending on the type of masonry, the material is considered as homogeneous and either isotropic elastic-plastic (Lofti & Shing, 1991) or orthotropic linear-elastic (Rots, 1991). A crack, oriented normal to the principal stress direction, is initiated when one of the principal stresses reaches a certain threshold value (e.g. the tensile strength). Once a crack is formed, the cracked solid is considered as an orthotropic material by incorporating a traction-crack strain law using a local n,s,t-coordinate system, oriented in line with the crack (Figure 2-18).
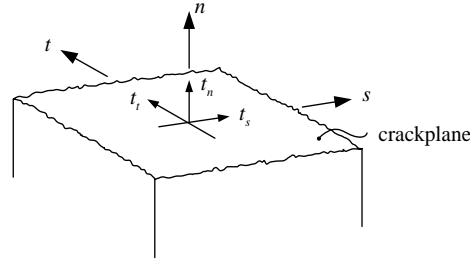
Figure 2-18 Local coordinate system and tractions across the crack (Rots, 1988)

In order to distinguish between the constitutive behaviour of the crack and the solid material in between, the total strain $\Delta\varepsilon$ is decomposed into a masonry strain increment $\Delta\varepsilon^{ma}$ and into a crack strain increment $\Delta\varepsilon^{cr}$:

$$\Delta\varepsilon = \Delta\varepsilon^{cr} + \Delta\varepsilon^{ma} \qquad (2.35)$$

Originally, the decomposition has been designed to enhance earlier versions of the smeared crack concept for concrete. It essentially aims to maintain the similarity between the smeared crack concept and the discrete crack approach, which distinguishes between the crack and the solid material by using separate finite elements (Rots, 1988). The main advantage is that the distinction between the constitutive behaviour of the cracks and the solid material between the cracks (Figure 2-19), facilitates the implementation of sophisticated crack laws that have been developed over the years.
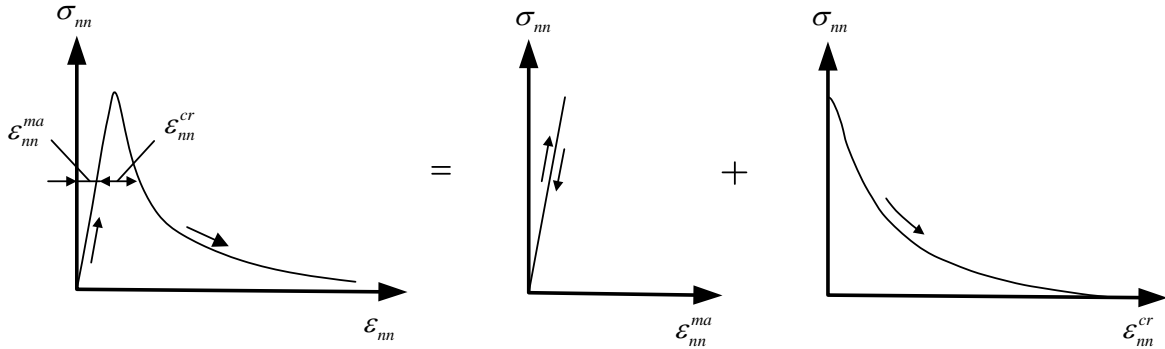
Figure 2-19 The decomposition of the total strain ε_{nn} of a fracture zone into a masonry strain ε_{nn}^{ma} and a crack strain ε_{nn}^{cr} (Rots et al., 1985).

The crack strain vector $\Delta\varepsilon^{cr}$ in (2.35) describes the six strain components related to the three dimensional configuration and is given as:

$$\Delta\varepsilon^{cr} = [\Delta\varepsilon_{xx}^{cr}, \Delta\varepsilon_{yy}^{cr}, \Delta\varepsilon_{zz}^{cr}, \Delta\gamma_{xy}^{cr}, \Delta\gamma_{yz}^{cr}, \Delta\gamma_{zx}^{cr}]^T \qquad (2.36)$$

in which the x,y and z indices refer to global coordinate axes. The local strain vector Δe^{cr} that refers to the local n,s,t-coordinate system can be presented as the following:

$$\Delta e^{cr} = [\Delta e_{nn}^{cr}, \Delta\gamma_{ns}^{cr}, \Delta\gamma_{nt}^{cr}]^T \qquad (2.37)$$

where Δe_{nn}^{cr} relates to the Mode I normal strain and $\Delta \gamma_{ns}^{cr}$, $\Delta \gamma_{nt}^{cr}$ describe the Mode II and Mode III crack shear strains respectively. The global and the local strain vector are related via a transformation vector N that reflects the orientation of the crack, i.e. the inclination angle between the normal of the crack and the global x-axis:

$$\Delta \varepsilon^{cr} = N \Delta e^{cr} \tag{2.38}$$

The same reasoning holds for the relation between the local stress increment Δs^{cr} and the global stress increment $\Delta \sigma$:

$$\Delta s^{cr} = N^T \Delta \sigma \tag{2.39}$$

To complete the set of equations that describes the global stress-strain relation, an incremental constitutive relation for the masonry and the cracked material is assumed:

$$\Delta \sigma = D^{ma} \Delta \varepsilon^{ma} \tag{2.40}$$

$$\Delta s^{cr} = D^{cr} \Delta e^{cr} \tag{2.41}$$

Substituting (2.35), (2.38) and (2.40) in (2.39):

$$\Delta s^{cr} = N^T D^{ma} [\Delta \varepsilon - N \Delta e^{cr}] \tag{2.42}$$

Using equation (2.41) this yields:

$$\Delta e^{cr} = \left[D^{cr} + N^T D^{ma} N \right]^{-1} N^T D^{ma} \Delta \varepsilon \tag{2.43}$$

Substituting equation (2.35) and (2.38) in (2.40) the following relation is obtained:

$$\Delta \sigma = D^{ma} \left[\Delta \varepsilon - N \Delta e^{cr} \right] \tag{2.44}$$

Combining equation (2.43) and (2.44) provides a constitutive relation for the cracked masonry:

$$\Delta \sigma = \left[D^{ma} - D^{ma} N \left(D^{cr} + N^T D^{ma} N \right)^{-1} N^T D^{ma} \right] \Delta \varepsilon \tag{2.45}$$

In general, D^{ma} may reflect material characteristics such as elasticity, plasticity, creep etc. (Rots et al., 1985), but for masonry it is generally assumed to be an orthotropic linear-elastic matrix that reflects the significant influence of the bed and head joints. The matrix D^{cr}, related to the incremental constitutive relation between the interface stresses and local crack strains, describes the cracking characteristics of masonry such as tension-softening and shear cracking. In contrast with concrete, for which the crack matrix does not depend on the orientation of the crack, the crack matrix for masonry is a function of the inclination angle between the normal of the crack and the joints. For this reason, the parameters that primarily influence the softening terms in the crack matrix, become a function of the inclination angle between the crack and the joints, i.e. $f_{ct} = f_{ct}(\alpha)$ and $G_f = G_f(\alpha)$. Optionally, the principal

compression stress parallel to the crack can follow a nonlinear compression-softening model too as shown in Figure 2-20.
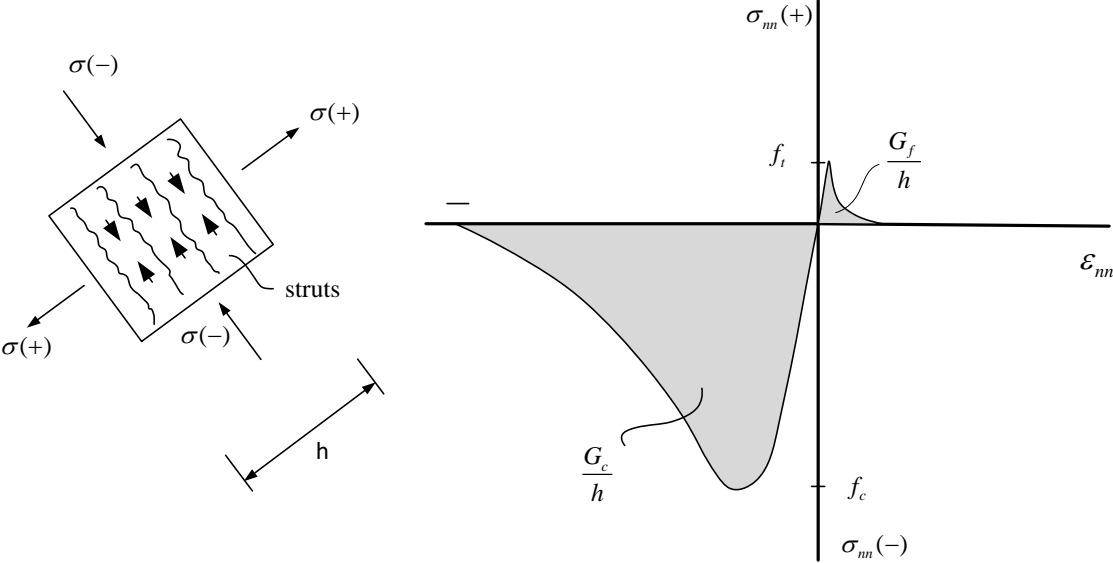
Figure 2-20 Tensile and compression stress versus the crack strain diagrams.

2.3.3 Macro-element model

The idealization of a masonry wall as an assemblage of macro-elements starts from the notion that the observed seismic damage on masonry buildings is primarily concentrated in piers and spandrels. The use of a macro-element discretization has been pursued before and ongoing research resulted into the equivalent frame approach, in which single macro elements are used, representing the structural members of a masonry wall (Figure 2-21a). The extension of the equivalent frame approach to the nonlinear field has mainly been made by Italian researchers (Magenes & Della Fontana, 1998) and was conceived for the global analysis of new and existing masonry buildings. Today's most popular program available, adopting the equivalent frame approach for the nonlinear seismic analysis of masonry buildings is the TREMURI program, developed by S. Lagomarsino, A. Penna, A. Galasco and S. Cattari. The main features of the non-linear beam element implemented in TREMURI for modelling piers and spandrels are hereinafter summarized.

In this method, the deformable elements (i.e. piers and spandrels) are modelled as ideally elastic-plastic beam-column elements, in which the chord rotation θ_u (sum of flexural deformation φ and of shear deformation γ) is limited (Figure 2-21b).
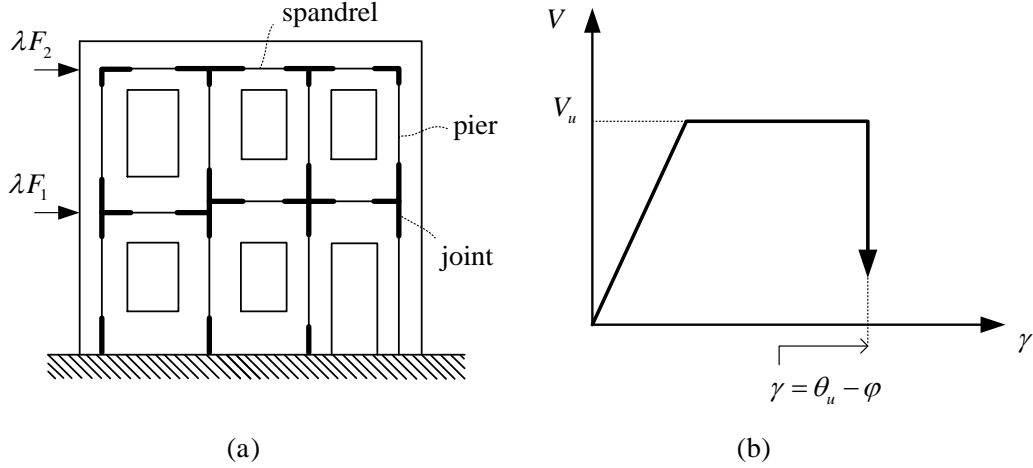
Figure 2-21 Equivalent frame idealization of a masonry wall (a) and idealized nonlinear behaviour of a pier element failing in shear (b) (Magenes, 2000).

The parts which are usually not subjected to damage are modelled by means of infinitely stiff joint elements (Figure 2-21a). As can be seen from (Figure 2-21b), the deformable elements display an ideal plastic behaviour with a maximum deformation (beyond that the element is not able anymore to withstand any lateral load and is, in fact, a truss), whenever the nodal generalized forces of the element (Figure 2-22a) attains one of the limit values M_u or V_u, estimated according to the strength criteria presented in section 2.2.1. The initial stiffness is given by the elastic properties (i.e. geometrical and mechanical) of the panel and assembling the terms associated with axial, shear and flexural deformation the linear elastic stiffness matrix of the two dimensional frame element can be obtained (2.46):

$$
\begin{Bmatrix} T_i \\ N_i \\ M_i \\ T_j \\ N_j \\ M_j \end{Bmatrix} =
\begin{bmatrix}
\dfrac{12EI}{L^3(1+\psi)} & 0 & -\dfrac{6EI}{L^2(1+\psi)} & -\dfrac{12EI}{L^3(1+\psi)} & 0 & -\dfrac{6EI}{L^2(1+\psi)} \\[2ex]
0 & \dfrac{EA}{L} & 0 & 0 & -\dfrac{EA}{L} & 0 \\[2ex]
-\dfrac{6EI}{L^2(1+\psi)} & 0 & -\dfrac{EI(4+\psi)}{L(1+\psi)} & \dfrac{6EI}{L^2(1+\psi)} & 0 & \dfrac{EI(2-\psi)}{L(1+\psi)} \\[2ex]
-\dfrac{12EI}{L^3(1+\psi)} & 0 & \dfrac{6EI}{L^2(1+\psi)} & \dfrac{12EI}{L^3(1+\psi)} & 0 & \dfrac{6EI}{L^2(1+\psi)} \\[2ex]
0 & -\dfrac{EA}{L} & 0 & 0 & \dfrac{EA}{L} & 0 \\[2ex]
-\dfrac{6EI}{L^2(1+\psi)} & 0 & \dfrac{EI(2-\psi)}{L(1+\psi)} & \dfrac{6EI}{L^2(1+\psi)} & 0 & \dfrac{EI(4+\psi)}{L(1+\psi)}
\end{bmatrix}
\begin{Bmatrix} u_i \\ w_i \\ \phi_i \\ u_j \\ w_j \\ \phi_j \end{Bmatrix} \quad (2.46)
$$

where ψ is given as $1.2ED^2/(GL^2)$; E and G are the Young and shear moduli, respectively; A and I are the cross-section and the moment of inertia of the panel, respectively and L and D are the height and width of the panel. In the nonlinear phase a

stiffness degradation is described by a stiffness reduction coefficient (Figure 2-22b) describing the cracked conditions of the panel. Usually, a simplified procedure is adopted, i.e. the elastic stiffness properties are reduced by for example 50%.

(a)   (b)
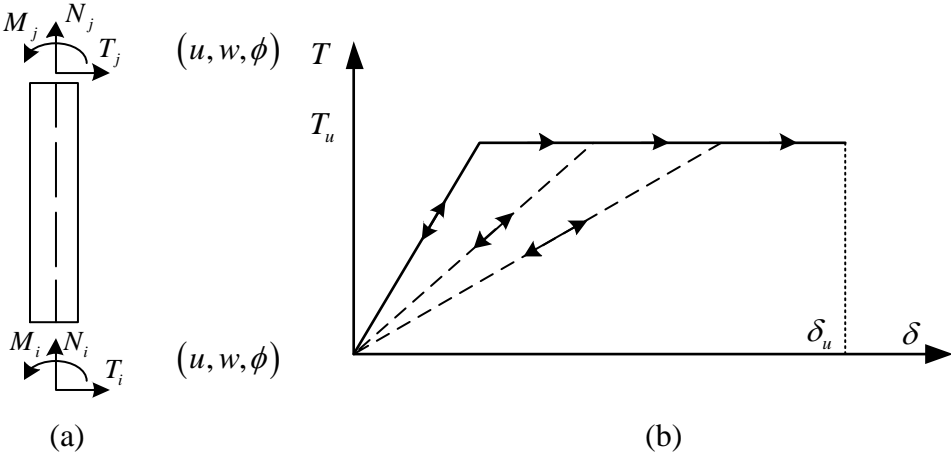
Figure 2-22 Non-linear beam degrading behaviour (S.T.A. DATA, n.d., p. 27)

Compared to the computational strategies mentioned before, the method drastically reduces the number of degrees of freedom and is therefore, especially attractive if a low computational burden is required.

3 THEORETICAL BACKGROUND

In the last section of chapter two various numerical models have been discussed to analyse brick masonry structures. Recently, the main focus of research in numerical modelling strategies for masonry have been devoted to macro-modelling as researchers recognized that the micro-models are not suited to analyse the response of masonry on a global level because of the computational burden. Therefore, in this chapter the theoretical background of three macro-modelling techniques will be considered, namely an isotropic continuum model and an two alternative equivalent frame models. All approaches are based on the material models and finite elements present in the multipurpose finite element software package DIANA.

3.1 An isotropic continuum model

As mentioned above, originally the smeared crack concept has been designed to analyse concrete structures for which the stiffness matrix does not depend on the orientation of the crack. Furthermore, it was argued that for masonry, being anisotropic in nature, the stiffness matrix is dependent on the orientation of the crack, significantly complicating the constitutive relation for the cracked material. However, as recognized by many researchers, its implementation into both analytical and numerical procedures is rather difficult. Besides, Turnšek and Cacovic have proven on the basis of correlation between an analytical isotropic model and experimental data that masonry is anisotropic at material point level but that the response at larger scale can be interpreted as isotropic in case of diagonal cracking failure. Furthermore, compared with the behaviour of concrete subjected to tension, brick masonry is also characterized by a very low tensile strength and a brittle behaviour in tension.

For these reasons, a simple continuum model based on a smeared rotating crack total strain concept and an isotropic material formulation has become more and more popular throughout the years, and has proven to be able to provide reasonably accurate results (especially for monotonic loading) despite its limitations.

3.1.1 Modelling considerations

In this work, the abovementioned rotating total strain crack model is used to model the masonry. The tensile behaviour of the masonry is described via a linear softening curve and the compressive behaviour is based on a parabolic curve (Figure 3-1). Both softening curves are described by the tensile stress, the compressive stress, the Mode-I fracture energy G_f^I and

fracture energy in compression G^I_{f-c}. For quadratic plane stress elements DIANA computes the crack bandwidth equal to the square root of the total area of the finite element ($h = \sqrt{A}$).
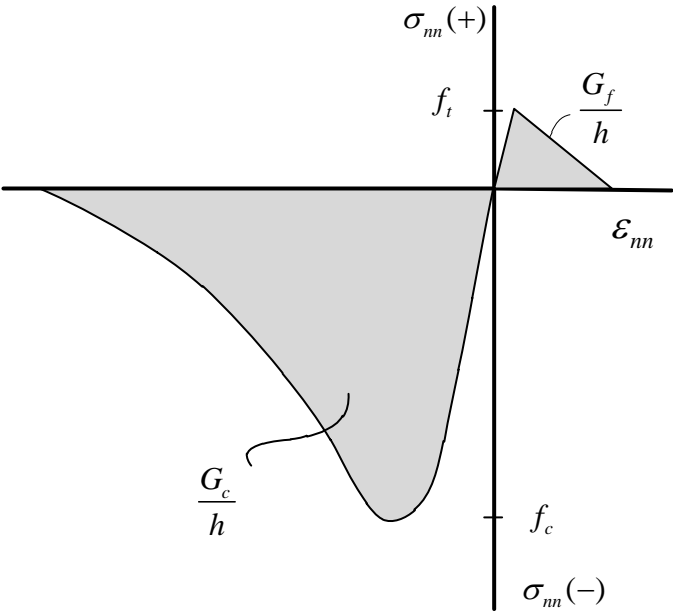
Figure 3-1 Predefined tension and compression behaviour for the total strain crack model.

Two modelling approaches are proposed in this report. In the first model all piers and spandrels are represented by finite elements having the same material properties (Figure 3-2a and Figure 3-2c). In this report it will be referred to as "Continuum Model (CM)". For all finite elements the same joint tensile strength will be assumed, since usually the joints (interface between brick and mortar) are the weakest links in masonry. In the second model horizontal layers are included at both the extremes of the masonry panels (Figure 3-2b/Figure 3-2d). The elements of these layers have lower strength and lower fracture energy than the parent material, to capture the rocking failure mode of piers or spandrels. Hence, the horizontal layers (Figure 3-2b – yellow zone) at the top and bottom represent the flexural behaviour and the parent material (Figure 3-2 – green zone) is adopted in the region in which diagonal cracking may occur. In essence, this approach is an attempt to model the anisotropic and nonhomogeneous nature of masonry and better describes the different failure modes of masonry panels. From this point of the document on, it will be referred as "Three Zoned - Continuum Model (TZ-CM) ".

As mentioned above, the horizontal layers at the top and bottom base are generally those regions were cracking along the bed joints takes place. Therefore, for piers the flexural behaviour is simply characterized by the bed joint tensile strength, the corresponding fracture

energy and the compression strength of masonry. However, for spandrels the flexural behaviour (Figure 3-2d – yellow zone) is more complex than for piers, since in this case the tensile strength is also dependent on the interlocking phenomena between the toe and the adjacent masonry (section 2.2.2.1). Based on the interlocking effect and considering two potential flexural failure modes, Cattari and Lagomarsino (2008) derived an equivalent tensile strength representing the flexural property of a spandrel element:

$$f_{st} = \sigma_x = \min\left(\frac{f_{bt}}{2}, c + \frac{\Delta_x}{2\Delta_y} \mu \sigma_y \right) \tag{3.1}$$

Therefore, in this study equation (3.1) will be adopted to determine the flexural resistance of the spandrels.
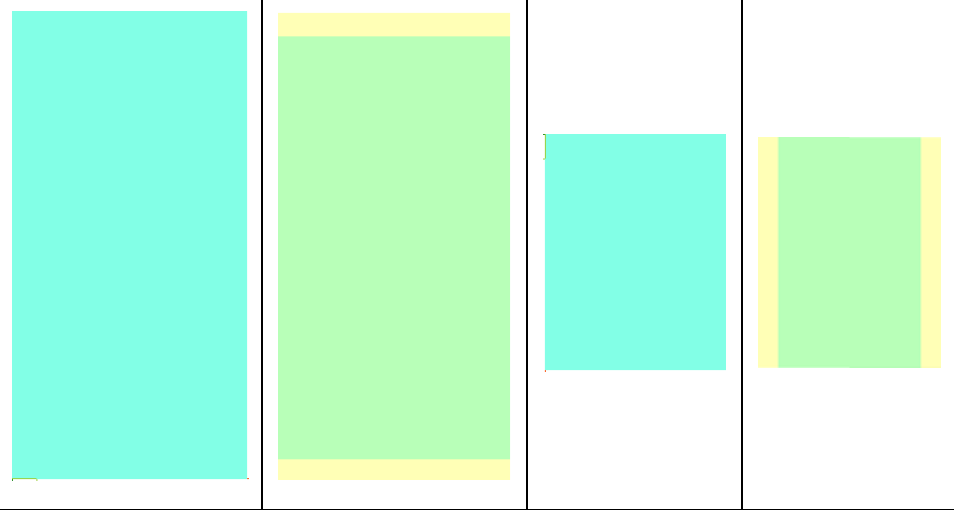
Failure mode	Piers		Spandrels	
	CM	TZ-CM	CM	TZ-CM
Flexural	f_{jt}	f_{jt}	f_{jt}	f_{st}
Diagonal cracking	f_{jt}	f_{tu}	f_{jt}	f_{tu}
	(a)	(b)	(c)	(d)

Figure 3-2 Properties for the continuum model (a &c) and three zoned - continuum model (b & d).

The reference tensile strength that governs the diagonal cracking mode (Figure 3-2/Figure 3-2d – green region) cannot be obtained from the separate material components and should be estimated. The estimation may be based on experiments and the expression developed by Turnšek and Cacovic (1971) to evaluate shear failure of piers associated with diagonal cracking:

$$V_d = Dt \frac{f_{tu}}{k_1} \sqrt{1 + \frac{\sigma_v}{f_{tu}}} \tag{3.2}$$

where k_1 is the shear stress distribution factor depending on the pier aspect ratio $\lambda = H/D$ and f_{tu} represents the reference tensile strength of masonry. A possible criterion for $k_1(\lambda)$ is presented by Benedetti and Tomazevic (1984) :

$$
\begin{aligned}
k_1 &= 1 \quad &for& \quad \lambda < 1 \\
k_1 &= \lambda \quad &for& \quad 1 \le \lambda \le 1.5 \\
k_1 &= 1.5 \quad &for& \quad \lambda > 1.5
\end{aligned}
\tag{3.3}
$$

Inverting equation (3.2) an expression for the reference tensile stress f_{tu} can be obtained:
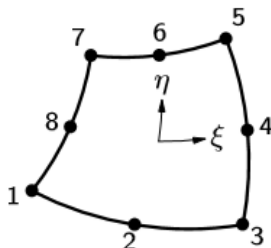
$$
f_{tu} = -\frac{1}{2}\sigma_v + \frac{1}{2}\sqrt{\sigma_v^2 + 4\left(\frac{k_1 V}{Dt}\right)^2}
\tag{3.4}
$$

Consequently, the only parameter that is unknown is the reference tensile fracture energy. In this report the reference fracture energy is estimated to be equal to 0.05 N/mm. It should be noticed that this estimation is on the higher side, to ease the numerical procedure and avoiding convergence problems.

3.1.2 Type of elements (plane stress - quadrilateral)

All continuum models adopt eight-node quadrilateral (CQ16M) isoparametric plane stress elements. These elements are based on quadratic interpolation and the integration scheme is 2x2 Gaussian integration. All features are presented in Table 3-1.

Table 3-1 Features of the element CQ16M.

Figure:	
Type:	CQ16M - quadrilateral isoparametric plane stress element
Degrees of freedom:	u_x, u_y
Nodes:	8
Interpolation polynomials:	$u_i(\xi,\eta) = a_0 + a_1\xi\eta + a_2\eta + a_3\xi\eta + a_4\xi^2 + a_5\eta^2 + a_6\xi^2\eta + a_7\xi\eta^2$ ε_{xx} varies linearly x-direction and quadratically in y-direction ε_{yy} varies linearly y-direction and quadratically in x-direction ε_{xy} varies quadratically in both directions
Integration scheme	2 x 2 Gauss integration

3.2 An alternative equivalent frame model: a Fibre Flexure Model (FFM).

By definition, the equivalent frame method ignores the activation of local failure modes. The method mainly considers the global response of masonry structural components (piers or spandrels) and does not focus on a correct representation of the masonry material. This also entails a crude representation of the cracked condition of the masonry panel (as cited in Marques and Lourenco, 2011, p. 6). Therefore, a modification of the method might be to use displacement-based numerical integrated (fibre) beam finite elements, combined with an appropriate constitutive model that represents the anisotropic behaviour of masonry. A similar approach has recently pursued by Sepe et al. (2014), although in this method the masonry wall behaviour is modelled through fibre section force-based elements within the framework of the Timoshenko beam theory. To analyse the structural behaviour of masonry structures with the numerically integrated beam elements, the finite element package DIANA will be used. Therefore, this section deals with the most important features of the Class III Mindlin beam elements, which include both the flexural and shear deformation.

3.2.1 Modelling considerations

Whereas existing equivalent frame methods are usually based on lumped plasticity models (i.e. non-linear behaviour is limited to the end- and midsection of the element), the approach discussed here considers the entire member (e.g pier or spandrel) as an inelastic element, i.e. distributed inelasticity model. To determine the global nonlinear response of a frame, the members are represented by series of beam elements (Figure 3-3) with two numerically integrated controlling sections along the bar axis (gauss points). The sectional response is evaluated via a fibre discretization in which each fibre (or integration point over the height) may follow a material uniaxial nonlinear stress-strain relation (Figure 3-3).
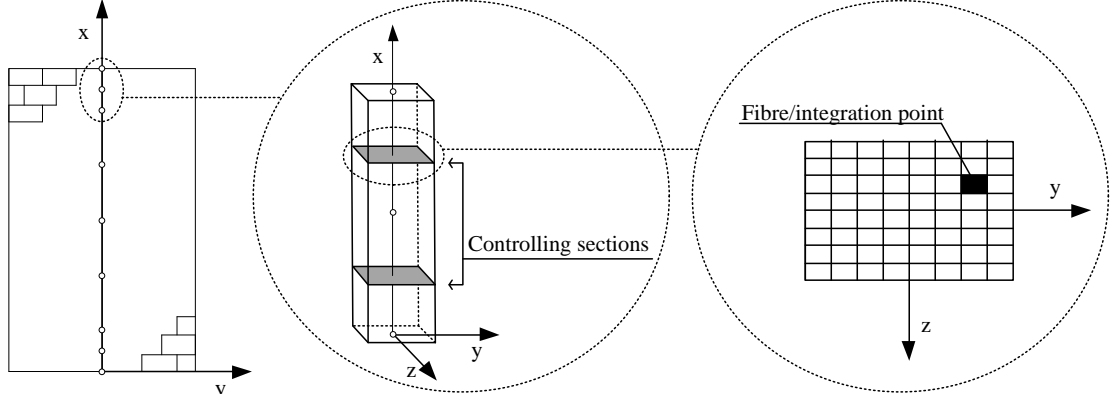
Figure 3-3 Fibre section discretization and controlling sections (gauss points) along the bar axis.

Such an approach could be considered as closer to reality since the inelasticity does not necessarily occur at the end sections, but could also take place at intermediate control sections. Furthermore, as this approach with the fibre discretization still acts on material point level and is in essence dependent on the specified material parameters, it is not required to implement empirical strength domains to determine the ultimate bending strength. A disadvantage is that the shear response is still linear elastic, consequently meaning that the diagonal cracking mode is ignored, as discussed in section 3.3. The proposed model will be hereinafter named Fibre Flexure Model (FFM).

As mentioned before, the flexural response is mainly determined by the uniaxial behaviour of the beam-column element. Therefore, a fibre stress-strain relation needs to be specified so that it correctly describes the uniaxial behaviour of masonry panel subjected to an overturning moment. As the flexural behaviour of masonry is governed by the material properties of the bed joints, the proposed FFM describes the fibre stress-strain of the bed joints via a linear softening curve in tension and a parabolic curve for the behaviour in compression.
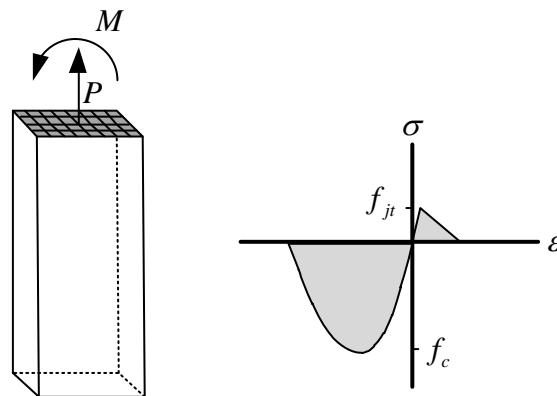
Figure 3-4 Fibre stress strain relation describing the bed joint behaviour in tension and compression.

3.2.2 Type of elements (beam - fibre)

In contrast with the classical beam elements according to the Euler-Bernoulli theory , the Class III elements are based on the Mindlin-Reissner theory, which takes shear deformation into account. They are based on an isoparametric formulation in order to simplify the numerical integration and to allow the higher-order beam elements to be curved. The primary variables are the translations u and the rotations ϕ in the nodes. According to the Mindlin theory, the translation and rotations of the beam axis are independent variables and are respectively interpolated from the nodal quantities. The displacements (3.5) are oriented in the local xyz and in the global XYZ directions for the two-dimensional (Figure 3-5a) and three dimensional beams (Figure 3-5b) respectively.

$$\text{two-dim.}: \quad u_e = \begin{Bmatrix} u_x \\ u_y \\ \phi_z \end{Bmatrix} \qquad \text{three-dim.}: \quad u_e = \begin{Bmatrix} u_X \\ u_Y \\ u_Z \\ \phi_X \\ \phi_Y \\ \phi_Z \end{Bmatrix} \qquad (3.5)$$

<center>(a) two-dimensional   (b) three-dimensional</center>
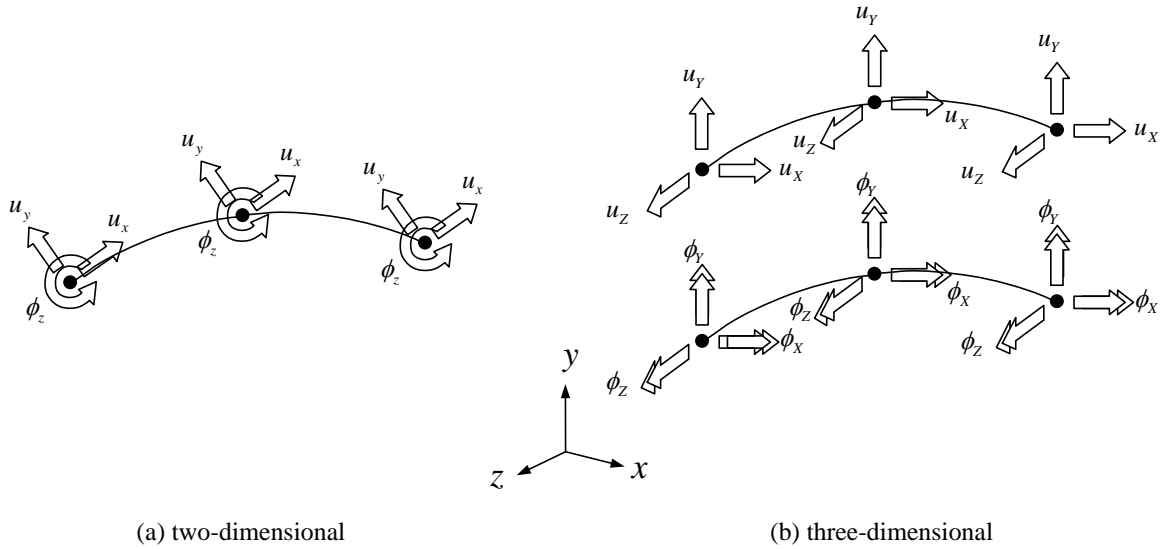
Figure 3-5Displacements for class-III beams (Manie & Kikstra, 2009).

3.2.2.1 Deformation, strains and stresses

The primary strains in an infinitesimal part of the beam are derived from the translations and rotations in the nodes (Figure 3-6). The transverse shear strains γ_{xy} and γ_{zx} are forced to be constant and by default DIANA assumes a correction factor of 1.2 to account for actual quadratic transverse shear stress distribution. For the three-dimensional Class III beam elements the primary strains are the Green Lagrange strains:

$$\varepsilon = \begin{Bmatrix} \varepsilon_{xx} \\ \gamma_{xy} \\ \gamma_{zx} \end{Bmatrix} \qquad (3.6)$$

with:

$$\varepsilon_{xx} = \frac{du_x}{dx} \qquad \gamma_{xy} = \frac{du_x}{dy} + \frac{du_y}{dx} \qquad \gamma_{zx} = \frac{du_x}{dz} + \frac{du_z}{dx} \qquad (3.7)$$
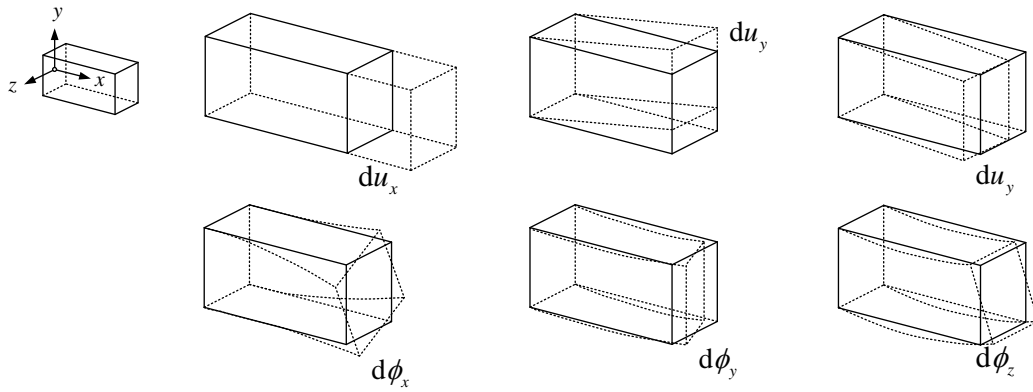
Figure 3-6Deformations for the three dimensional beams (Manie & Kikstra, 2009).

DIANA can calculate the Cauchy stresses resulting from the moments and forces. The primary stresses are:

$$\sigma = \begin{Bmatrix} \sigma_{xx} \\ \sigma_{xy} = \sigma_{yx} \\ \sigma_{zx} = \sigma_{xz} \end{Bmatrix} \tag{3.8}$$

The complete stress situation and sign convention for a three-dimensional beam element is shown in Figure 3-7.
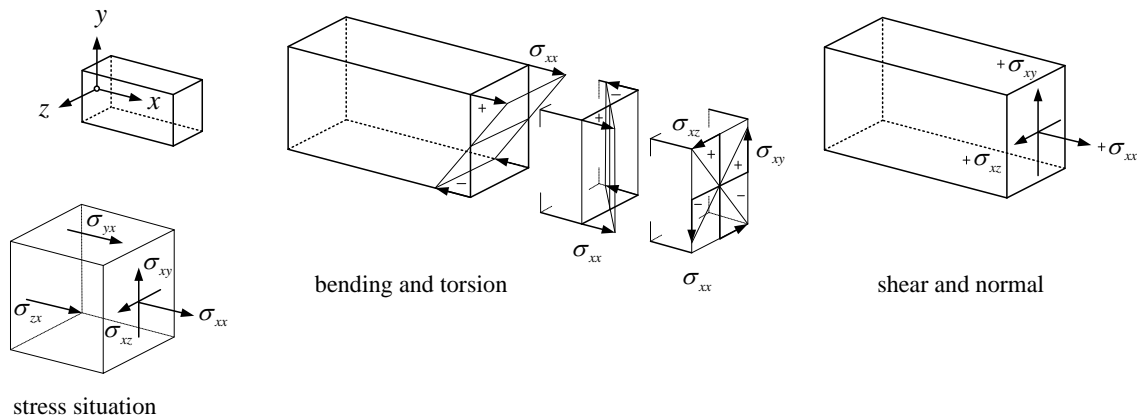
Figure 3-7Cauchy stresses for three-dimensional beams(Manie & Kikstra, 2009).

3.2.2.2 Integration schemes

The three dimensional Class III elements are numerically integrated both along the isoparametric ξ direction that coincides with the bar axis and over the cross sectional area. For the integration in the area of the cross section DIANA divides the cross sectional area into quadrilateral integration zones, adopting an isoparametric η, ς coordinate system. Figure 3-8 presents the possible integration schemes depending on the integration rule.
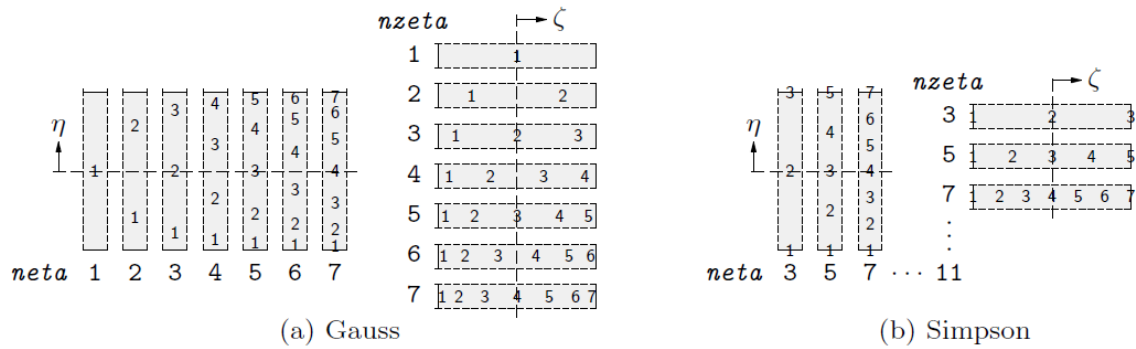
Figure 3-8 Integration schemes in quadrilateral zones in the area of the cross section(Manie & Kikstra, 2009).

3.2.2.3 Interpolation polynomials

DIANA offers several higher order class-III elements. The interpolation polynomials for the displacements of a three-node, three-dimensional class-III element can be expressed as:

$$
\left.\begin{aligned}
u_i(\xi) &= a_{i0} + a_{i1}\xi + a_{i2}\xi^2 \\
\phi_i(\xi) &= b_{i0} + b_{i1}\xi + b_{i2}\xi^2
\end{aligned}\right\} \qquad i = x, y, z \tag{3.9}
$$

From these expressions it can be seen that the strains vary linearly along the centre line of the beam. DIANA offers also a four-node and a five-node three-dimensional class-III elements, resulting in strain fields that vary quadratically and third-order, respectively.

3.3 An alternative equivalent frame model: a Fibre Flexure – Lumped Shear Model (FF-LSM).

As have been pointed out before, the shearing behaviour of the numerically integrated beam elements in DIANA is described linear elastically and therefore, the elements do require a modification to include shearing failure modes. In this work a structural nodal interface has been adopted describing the interface behaviour by means of a relation between normal and shear tractions and normal and shear relative displacements within the interface element (Figure 3-9).
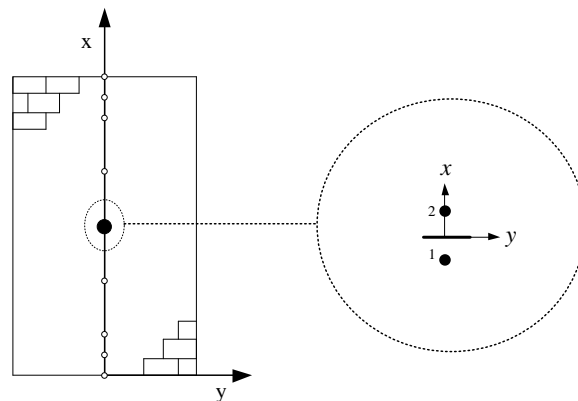
Figure 3-9 Pier discretization over the height and interface element placed between two nodes of adjacent beam elements, located in the centre of the structural component (black dot).

39

Conceptually such an approach can be visualized by considering the flexural and shear response of the structural component (Figure 3-10). Adopting the nodal interface element, placed between two nodes, the axial and bending behaviour is described with the fibre-section discretization and the shear behaviour is modelled via a bilinear shear traction relative displacement $(t_t - \Delta u_t)$ law. The proposed model will be hereinafter named FF-LSM (Fibre Flexure – Lumped Shear model) because it lumps shearing nonlinearities in one single interface element located in the centre of the structural component, whereas flexural and crushing behaviour is evaluated via smeared crack elements. The coulomb friction model that is used to describe the relation between the ultimate traction and the relative displacement and the features of the nodal interface (N4IF) are presented in the next two sections, respectively.
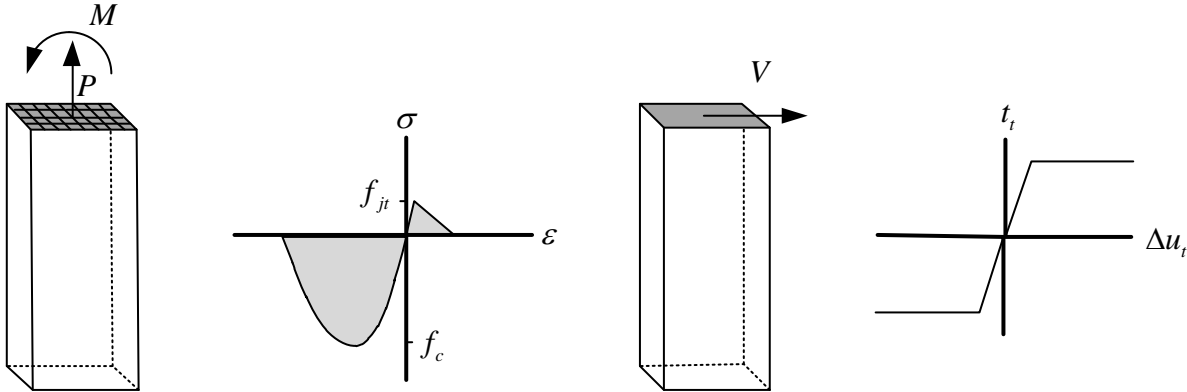
Figure 3-10The flexural response and the shear response modelled by the fibre section discretization and the shear traction relative displacement law, respectively.

3.3.1 Modelling Considerations

In the past, many researchers stressed the relation between the ultimate shear strength of a masonry structural component and a Coulomb friction (Figure 3-11) formulation as shear failure is often initiated by sliding of the bed joints. In such a model the basic assumption is that the ultimate shear strength t_t is influenced by the confining pressure t_n, the cohesion c and the friction angle ϕ (Figure 3-11).
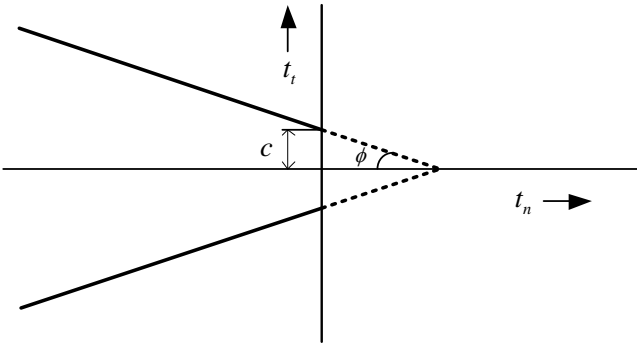
Figure 3-11 The Coulomb friction criterion.

As mentioned above, the interface nonlinearity of the nodal interface element is described with a Coulomb friction model. The perfectly plastic envelope (Figure 3-11), describing the shear-slipping in a 2D configuration, can be mathematically expressed as:

$$f = |t_t| + t_n \mu - c \qquad (3.10)$$

For $f \leq 0$ both tractions behave linear elastically, while for $f \geq 0$ a perfect plastic behaviour for the shear traction is initiated according to equation (3.10). Optionally for both the cohesion and the friction coefficient a softening diagram can be specified, to consider for example an ultimate drift limitation δ_u. The strength degradation model for piers adopted here yields a linear softening diagram for both parameters, initiated when the top displacement of the pier violates the drift capacity belonging to the shearing failure mode (i.e. 0.4% - recommended by Eurocode 8), while for the spandrels no drift limitations are considered. Entering the softening branch, the pier resistance gradually decreases to zero over a distance of approximately 3mm; however, further research would be needed to identify a precise softening diagram for both the parameters.
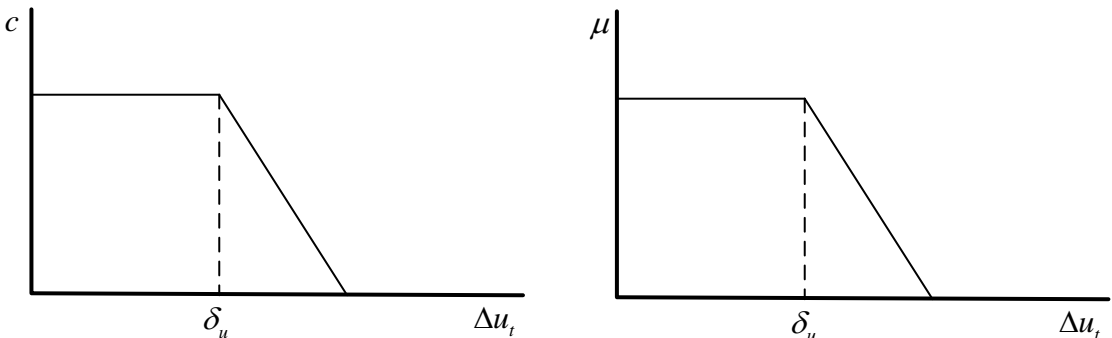
Figure 3-12Assumed softening branches for the cohesion and friction parameter upon violation of the plastic envelope.

Since the shear behaviour of the structural components is lumped into one single nodal interface, the cohesion and the friction angle should be global strength parameters. As pointed out before (section 2.2.1.2.2), adopting the local material parameters (i.e. properties of the bed joints) leads to an overestimation of the strength parameters because of the presence of weak head joints, a nonlinear shear stress distribution and a reduced section length because of tension cracks. Throughout the years researchers have proposed several corrections to account for the presence of weak head joints (Mann and Muller (1982) , to include the shear stress distribution effect (Magenes and Calvi, 1997) and to consider only the effective uncracked section length (Abrams, 1992). Among other possible shear failure criteria (discussed in section 2.2) for both piers and spandrels, all three approaches are summarized in Table 3-2.

Table 3-2Possible strength criteria available for the shear resistance of piers as discussed in section 2.2.1.2.2.

Element type	Failure mode	Strength criterion		
		Mann and Müller $V_d = Dt \min\{\tau_u, \tau_b\}$	Turnšek and Cacovic $V_d = Dt \min\{\tau_u, \tau_b\}$	Magenes and Calvi $V_d = Dt \min\{\tau_u, \tau_b\}$
Piers	Crack through head and bed joints	$\tau_u = \bar{c} + \bar{\mu}\, p$	$\tau_u = \dfrac{f_{tu}}{k_1}\sqrt{1 + \dfrac{p}{f_{tu}}}$	$\tau_u = \dfrac{\bar{c} + \bar{\mu}\, p}{1 + \alpha_v}$
	Crack through head joints and bricks		$\tau_b = \dfrac{f_{bt}}{2.3}\sqrt{1 + \dfrac{p}{f_{bt}}}$	$\tau_b = \dfrac{f_{bt}}{2.3(1+\alpha_v)}\sqrt{1 + \dfrac{p}{f_{bt}}}$
		Abrams (1992)		
	Bed joint sliding	$V_d = Dt\,\tau_s$ with $\tau_s = \left(\dfrac{1.5\bar{c} + \bar{\mu}\, p}{1 + 3\alpha_v \dfrac{\bar{c}}{p}}\right)$		
Spandrels		Beyer (2012)		
	Crack through head and bed joints	$V_{d,s1} = \dfrac{2}{3} h_{sp} t_{sp} \tau_u$ with $\tau_u = c + \mu p_{sp}$		
	Crack through head joints and bricks	$V_{d,s2} = h_{sp} t_{sp} \tau_b$ with $\tau_b = \dfrac{f_{bt}}{2.3(1+\alpha_v)}\sqrt{1 + \dfrac{p_{sp}}{f_{bt}}}$		

Where D = length; t = thickness; p = vertical pressure; $\bar{c} = c/1+\mu\varphi$ and $\bar{\mu} = c/1+\mu\varphi$ are corrected cohesion and friction coefficients dependent on the interlocking parameter $\varphi = 2\Delta y/\Delta x$ in which Δy and Δx are respectively the length and the height of the brick unit; α_v = shear ratio; f_{tu} = reference tensile strength; f_{bt} = brick tensile strength; k_1 = shear stress distribution factor as function of the slenderness and p_{sp} = axial stress in the spandrel

However, to adopt these shear strength criteria in a Coulomb friction model in which only the cohesion and friction coefficient can be specified , the analytical formulations (including the correction factors) should be rewritten into a more suitable format (Table 3-3). Furthermore, as shear-tensile cracking of the bricks only occurs in presence of extremely high normal force and therefore is considered as a relatively seldom failure mode, this failure criterion will be neglected. The contribution of the axial force in the spandrel to the shear strength is ignored also, because experimental results have shown that the spandrel shear equation based on the cohesive strength alone yields remarkably good approximations of the residual spandrel strength (section 2.2.2.2). Table 3-3 presents all the adopted strength criteria for the piers as well as for the spandrels.

Providing that before crack initiation the derived relative displacements within the interface element are negligible and avoiding ill-conditioned matrixes, the elastic normal and shear

moduli of the interface element are taken equal to the elastic normal and shear moduli of the masonry panel multiplied by a factor of 1000, i.e. $k_n = 1000\, E/l$ and $k_t = 1000\, G/D$.

Table 3-3Strength criteria adopted for nodal interface
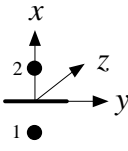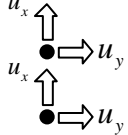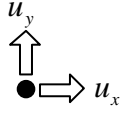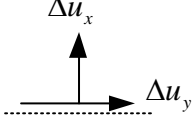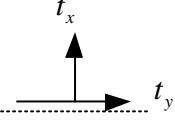
Element type	Failure mode	Coulomb Friction (CF): $V_d = Dt\tau_u$ in the form of $\tau_u = c + \mu p$		
		Mann and Müller (MM)	Magenes and Calvi (MC)	Abrams (A)
Piers	Diagonal cracking and/or sliding	$\tau_u = \overline{c} + \overline{\mu}\, p$ with $\overline{c} = \dfrac{c}{1 + \mu\varphi}$ $\overline{\mu} = \dfrac{\mu}{1 + \mu\varphi}$	$\tau_u = c_{mc} + \mu_{mc}\, p$ with $c_{mc} = \dfrac{\overline{c}}{1 + \alpha_v}$ $\mu_{mc} = \dfrac{\overline{\mu}}{1 + \alpha_v}$	$\tau_u = c_a + \mu_a\, p$ with $c_a = \left(\dfrac{1.5\overline{c}}{1 + 3\alpha_v \dfrac{\overline{c}}{p}} \right)$ $\mu_a = \left(\dfrac{\overline{\mu}}{1 + 3\alpha_v \dfrac{\overline{c}}{p}} \right)$
		Beyer (2012)		
Spandrels	Crack through head and bed joints	$c_{sp} = \dfrac{2}{3} c$		
Where D = length; t = thickness; p = vertical pressure; α_v = shear ratio of piers; $\varphi = 2\Delta y / \Delta x$ the interlocking parameter in which Δy and Δx are respectively the length and the height of the brick unit;				

3.3.2 Type of elements (structural interface – nodal)

The nodal interface element (Table 3-4) is an element placed between two adjacent beam elements. The interface surface and directions are specified by the user. The x and z axis should be oriented such that they are perpendicular to the interface, ensuring the horizontal y-axis being tangential to the interface. In the two dimensional configuration the variables are defined in the local xy axes system, i.e. the nodal displacements u_e being the basic variables and the relative displacements Δu and the tractions t representing the derived values. All features of the nodal interface element are summarized in Table 3-4.

Table 3-4 Features of the element N4IF.

Figure:	(a) topology (b) displacements		
Type:	N4IF – nodal interface element		
Variables :	$u_e = \begin{Bmatrix} u_x \\ u_y \end{Bmatrix}$	$\Delta u = \begin{Bmatrix} \Delta u_x \\ \Delta u_y \end{Bmatrix}$	$t = \begin{Bmatrix} t_x \\ t_y \end{Bmatrix}$
	Nodal displacements	Relative displacements	tractions
Nodes:	2		

4 VALIDATION OF THE MODELS

As chapter 3 was devoted to the description of both an existing continuum and an alternative equivalent frame model, chapter 4 addresses the validation of both models. To this end various types of international well-known benchmarks have been compiled and have been numerically simulated. The validation process starts at structural component level (section 4.1), investigating the in-plane behaviour of masonry piers under quasi static loading conditions, varying the panel geometries and boundary conditions. The model validation ends with simulating the response of an in plane shear test that was performed on a two-storey height full-scale masonry façade (section 4.2) and a comparison with the TREMURI results presented in Lagomarsino et al. (2013).

4.1 Masonry Panels - ISPRA and TU Delft

As mentioned in section 2.2, masonry walls are composed of several smaller piers which actually provide both the horizontal and vertical load bearing system. To investigate the seismic behaviour of the mentioned structural components both experimentally and numerically, Anthoine et al. 1995) performed four tests at the Joint Research Centre of the European community in Pavia for ISPRA (Istituto superiore per la protezione e la ricerca ambientale) on piers under both vertical and horizontal loads, reflecting the complex loading condition during an earthquake. To this purpose, while the horizontal displacement at the top was increased, servo-controlled actuators kept the vertical load constant and the top parallel to the bottom base. To investigate the strength degradation the walls have been quasi-statically exposed to alternated lateral displacements of increasing amplitude.
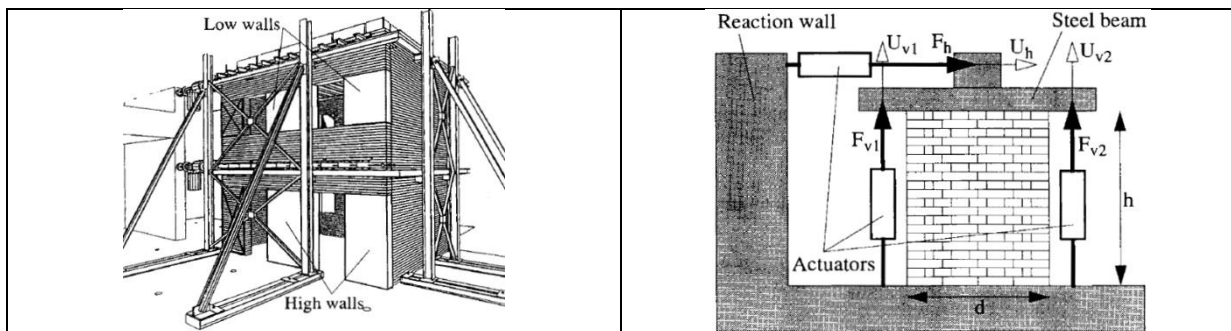
Figure 4-1Schematic view of the testing set-up (Anthoine, Magenes & Magonette, 1995).

In order to characterise Dutch masonry, a similar laboratory-based experimental program, comprising in-plane tests on replicated masonry walls was performed at the TU Delft in 2015. In the following three sections both experimental results will be used to examine the behaviour of the numerically integrated Mindlin-Reissner class III beam elements. The first

section gives a complete description of the geometries, adopted material properties and mesh input data, whereas the other two sections are devoted to the examination of the numerical results of both benchmarks, first on the results of the ISPRA tests, then the TU Delft tests. Both results sections are subdivided into three parts, subsequently addressing a number of aspects of the behaviour of the TZ-CM and the FFM, some sensitivity analyses and the obtained results adopting the FF-LSM.

4.1.1 Input

The dimensions and features of the ISPRA and TU Delft test samples including the ultimate load and the failure mode are presented in Table 4-1. Furthermore, the boundary conditions and the vertical load applied by the actuators are given. For a more detailed description of the tests set-up and test specimens is referred to Anthoine et al. (1995) and Ravenshorst and Messali (2016) for the ISPRA tests and TU Delft tests, respectively.

Table 4-1Input data

Specimen	BC	D	H	t	p	V^+	Prevailing failure mode
		m	m	m	MPa	kN	
Case 1: ISPRA tests							
I - high wall	DC	1.0	2.0	0.250	0.6	72	Rocking
I - low wall	DC	1.0	1.35	0.250	0.6	84	Diagonal cracking
Case 2: TU Delft tests							
TUD-0a	DC	1.1	2.7	0.102	0.7	27.7	Combined: • Rocking (flexure and crushing) • Sliding
TUD-2	C	1.1	2.7	0.102	0.5	9.40	Combined: • Rocking (flexure without crushing) • Sliding
TUD-3	DC	1.1	2.7	0.102	0.4	15.0	Combined: • Rocking (flexure and crushing) • Sliding
TUD-4	DC	4.0	2.7	0.102	0.5	119	Shear diagonal cracks along joints
TUD-5	DC	4.0	2.7	0.102	0.3	102	Sliding along the bottom joints
TUD-6	C	4.0	2.7	0.102	0.5	110	Shear diagonal cracks along joints and crushing of corners

Where BC = boundary conditions; D = length; H = height; t = thickness; p = vertical pressure; V^+ = shear strength for positive displacements; DC = double clamped; C = cantilever wall.

The mechanical parameters adopted in the numerical analyses are presented in Table 4-2. The reference tensile strength of masonry f_{tu}, is calculated on the basis of the experimental ultimate shear strength of TUD-4 for the TU Delft tests and I-low wall for the ISPRA tests. The tensile mode-I fracture energies have been deduced from Van der Pluijm (1992), who has

performed deformation controlled tension test on small masonry specimens of solid clay and calcium-silicate units. With the exception of the estimated tensile mode-I fracture energies (G_{f-jt}^{I} and G_{f-tu}^{I}) all other values in Table 4-2 are provided in Magenes (1997) for the ISPRA tests and in Esposito et al. (2016) for the TU Delft tests.

Table 4-2 Material properties ISPRA and TU Delft tests.

Property	Symbol	Unit	Case 1: TU Delft tests	Case 2: ISPRA tests
Joint tensile strength	f_{jt}	MPa	0.18	0.04
Reference tensile strength of masonry (1)	f_{tu}	MPa	0.13	0.24
Compressive strength of masonry in the direction perpendicular to bed joints	f_{c}	MPa	5.93	6.2
Young's modulus	E_{2}	MPa	5091	1410
Poisson ratio	ν	-	0.14	0.15
Reference fracture energy tensile mode-I (2)	G_{f-tu}^{I}	N/mm	0.05	0.05
Bed joint fracture energy tensile mode-I (3)	G_{f-jt}^{I}	N/mm	0.005	0.005
Fracture energy in compression for loading perpendicular to bed joints	G_{f-c}	N/mm	31.5	31.5
Note: (1) estimated on the basis of test results of TUD-4 for the TU Delft tests and I-low wall for the ISPRA tests (2) estimation (3) tensile bond behaviour of masonry: estimation based on Van der Pluijm (1992)				

Since mesh regions undergoing cracking are not know in advance, regular distributed quadrilateral meshes are generated for the CM (Figure 4-2a) and TZ-CM (Figure 4-2b). Generally, in case of the FFM (Figure 4-2c), the piers are discretized by two small beam elements located at the extreme sections of the masonry panel combined with four or five equally sized beam elements representing the middle part (Table 4-3). Maintaining the similarity with the CM and the TZ-CM, initially all beam elements in FFM have the same bed joint properties as adopted in the CM (this model is hereinafter named FFM-a). Second, a variation study on the FFM-a has been performed by reducing the bed joint fracture energy G_{f-jt}^{I} of both small beam elements (located at top and bottom) from 0.05 to 0.005 N/mm (Figure 4-2d). It will be referred to as FFM-b.

For both cantilever and double clamped walls the rotations and the translations at the bottom are fixed. A rigid link is adopted to prevent rotation of the top base in case of a double clamped boundary conditions and to keep the top nodes parallel to the nodes at the bottom base. For the beam elements this type of constrained is obtained by constraining the rotation

around the z-axis of the top node. Table 4-3 summarizes for both the continuum and fibre beam models the mesh input data.
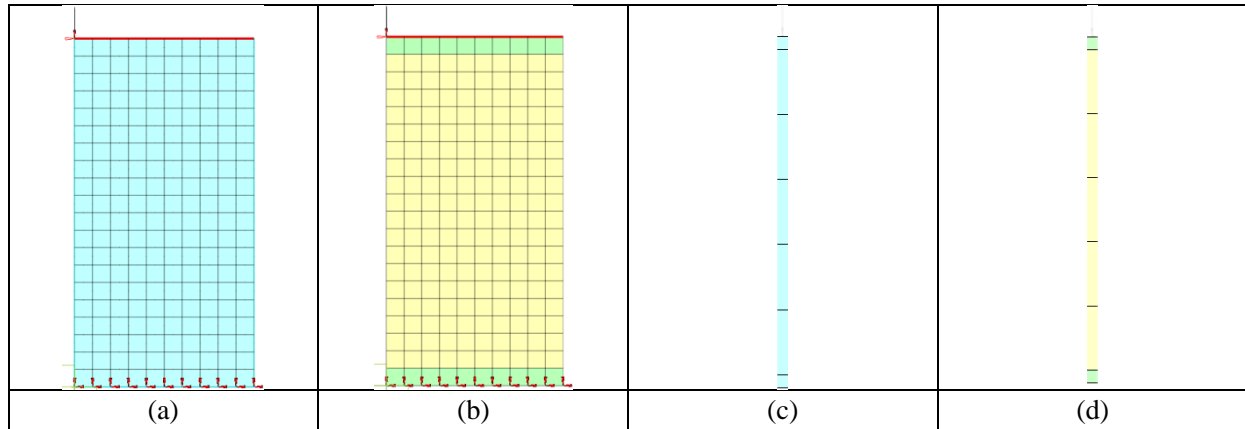
Figure 4-2 Representative meshes for the CM (a), TZ-CM (b) FFM-a (c) and FFM-b (d).

All masonry panels are subjected to pushover analyses in which the lateral displacements are gradually increased until the masonry panels fails and/or reaches the ultimate prescribed displacement $d_{r,f}$. The nonlinear set of equations is solved by means of the regular (or full) Newton-Raphson method, which means that the tangent stiffness matrix is derived at every iteration. During a specific load step not more than 100 iterations are allowed. In order to ensure DIANA to provide the correct solution, the force norm[1] as well as the displacement norm[2] are simultaneously checked.

Table 4-3 Mesh input data

Specimen		BC	Mesh size				Plane stress
			Beam				Plane stress
			Size	QTY	Size	QTY	Size
			[mm]		[mm]		[mm]
Case 1:	I - high wall	DC	100	2	450	4	100
ISPRA tests	I - low wall	DC	67.5	2	303.75	4	67.5
Case 2: **TU Delft tests**	TUD-0a	DC	100	2	500	5	100
	TUD-2	C	100	1	520	6	100
	TUD-3	DC	100	2	500	5	100
	TUD-4	DC	150	2	480	5	150
	TUD-5	DC	150	2	480	5	150
	TUD-6	C	150	1	480	5	150
Where BC = boundary conditions; DC = double clamped; C = cantilever wall; QTY = quantity							

---

[1] The ratio of the out-of-balanced force vector of the current iteration and the force unbalance at the beginning of that step.

[2] The ratio of the current displacement increment and the first displacement prediction of that step.

4.1.2 Results – masonry panels ISPRA

In this section the numerical results of the ISPRA tests will be compared with the experimental data. Besides, a control parameter has been added by using the analytical expression for the rocking failure mode. This can be interpreted as being a lower bound for the rocking failure mode, since it is based on a zero tensile strength assumption. Furthermore, the influence of the beam finite element mesh, the integration scheme in the area of the cross section, the impact of the reference fracture energy on the TZ-CM and the results of the FF-LSM are discussed.

4.1.2.1 Continuum and Fibre flexure models

The basic problem of adopting a total strain model and assuming masonry to be isotropic and homogeneous remains the selection of an appropriate tensile strength. It might be assumed that this should be equal to the joint tensile strength, since tests for the characterization of the constituting components of masonry have shown that the interface between the mortar and brick is very brittle and weak. However, Figure 4-3 (CM) shows very clearly that this approach results in the wrong failure mode of the high wall and consequently in a wrong force-displacement curve (blue line). Apparently, since such a diagonal crack was not found in the experiment, the tensile resistance for the regions undergoing diagonal cracking is higher than the assumed bed joint tensile strength. The problem can be solved by considering a TZ-CM, as this model is designed to account for such an effect. Indeed, with this modelling approach the correct failure mode Figure 4-3 (TZ-CM) is found and an almost perfect fit with the experiment data is obtained (red line). A similar phenomenon is found for the low wall, since in this case the CM shows the correct failure mode but along with the diagonal crack almost all other integration points cracked (Figure 4-4 – CM). Again, the TZ-CM results in the correct failure mode and fits better with the experimental data, although the corresponding drift at peak strength does not coincide with the one obtained from experiments. The FFM-a as well as the FFM-b performed extremely well for the high wall (Figure 4-3). The similarity between these two beam models can be explained by the fact that the tensile stress is as such, that the difference with the zero tensile stress assumption is almost negligible and the lower bed joint fracture energy adopted in FFM-b is of no influence. Figure 4-4 illustrates the overestimation of the member strength and the incapability of the beam elements of modelling the strength degradation that coincides with the diagonal crack. The reason therefore lay in the fact that the Class III beam elements only simulate failure in bending and only restrict the bending (axial) stresses.

ISPRA – high wall				**Scale 1:35**

Model	Mesh size	f_{jt}	G^I_{f-jt}	f_{tu}	G^I_{f-tu}
	mm	MPa	N/mm	MPa	N/mm
CM and FFM-a	100	0.04	0.05	-	-
TZ-CM and FFM-b	100	0.04	0.005	0.24	0.05
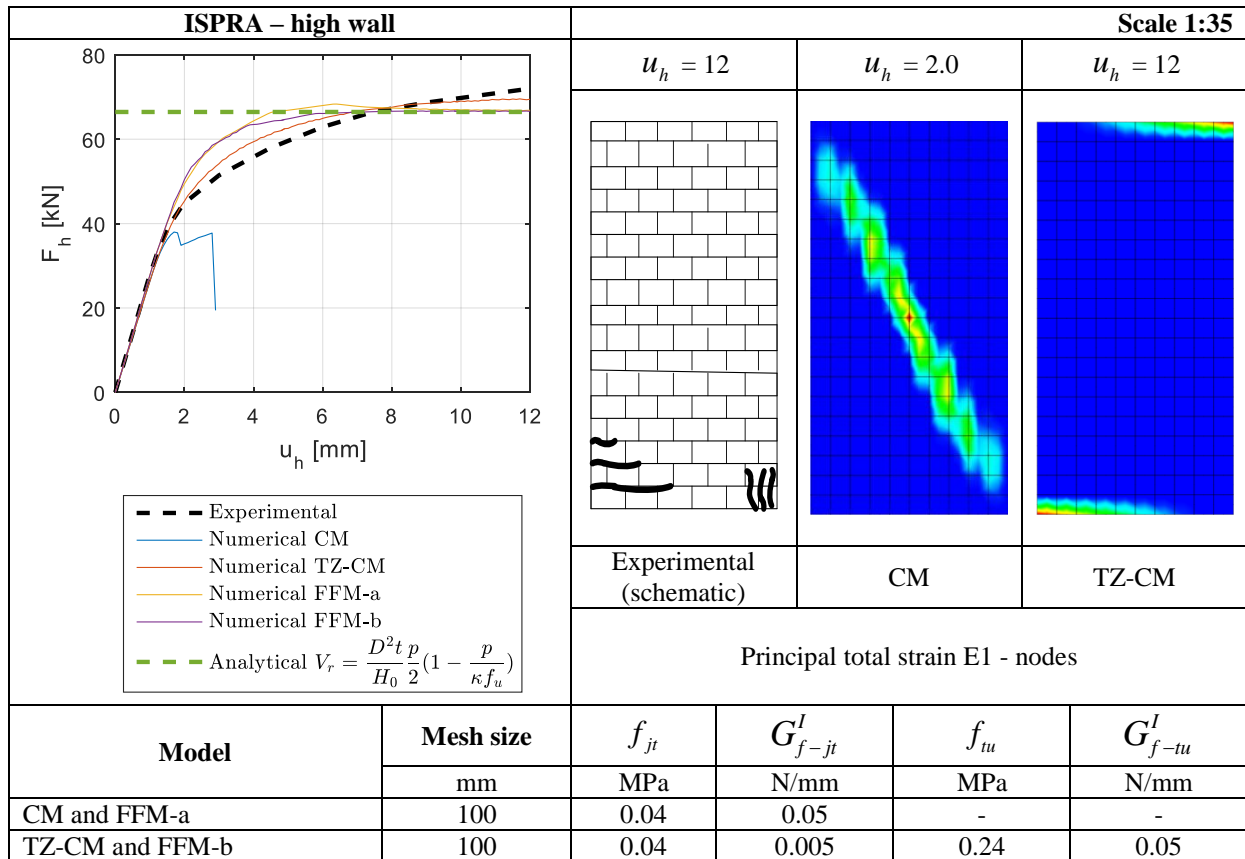
Figure 4-3 Force-displacement curve of the high wall and prevailing failure modes at the ultimate capacity for the CM and TZ-CM.

ISPRA – low wall				**Scale 1:35**

Model	Mesh size	f_{jt}	G^I_{f-jt}	f_{tu}	G^I_{f-tu}
	mm	MPa	N/mm	MPa	N/mm
CM and FFM-a	100	0.04	0.05	-	-
TZ-CM and FFM-b	100	0.04	0.005	0.24	0.05
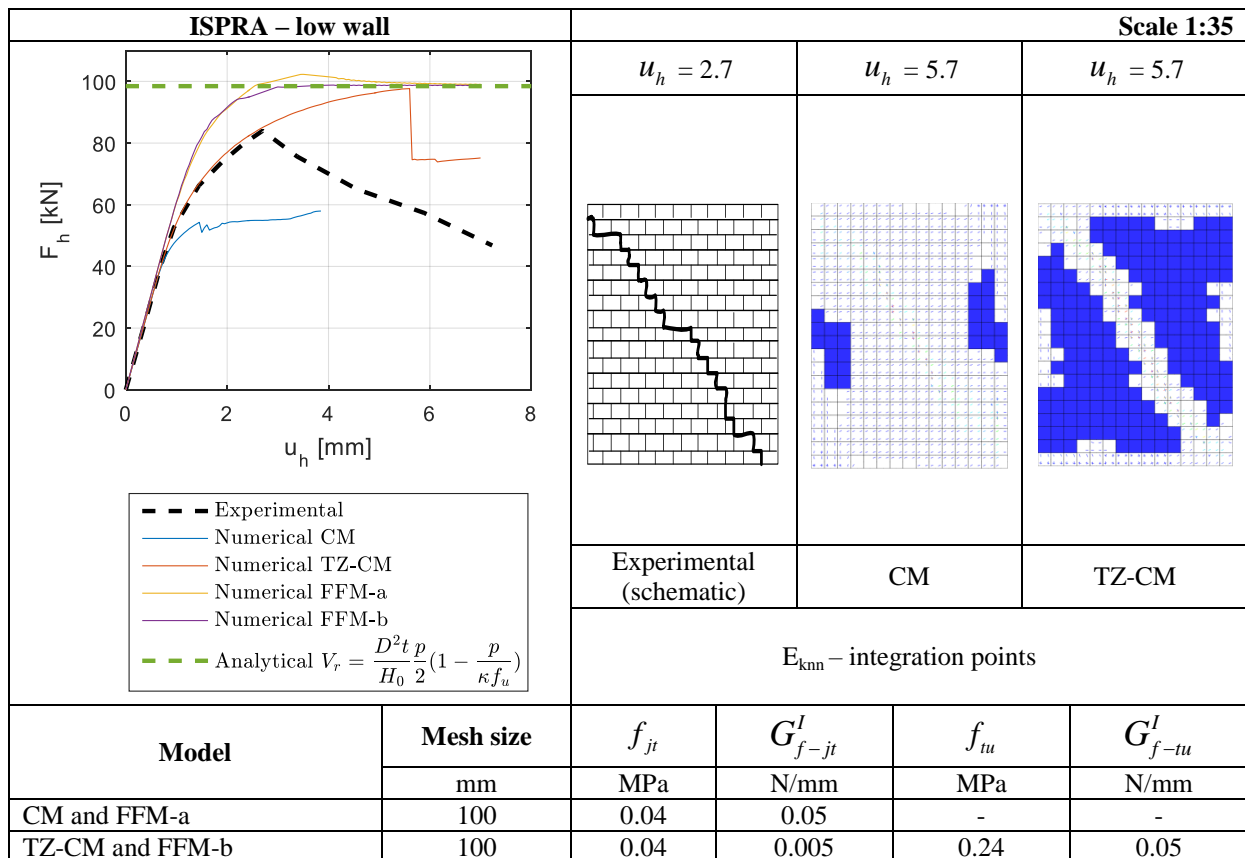
Figure 4-4 Force-displacement curve of the low wall and crack patterns at the ultimate capacity for the CM and TZ-CM.

In Figure 4-5 the crack propagation for increasing values of lateral displacement is shown by plotting the total principal tensile strains for the TZ-CM. The results are in good agreement with the failure modes observed in experiments, which implies that the high wall fails in rocking and the low wall by diagonal cracking.
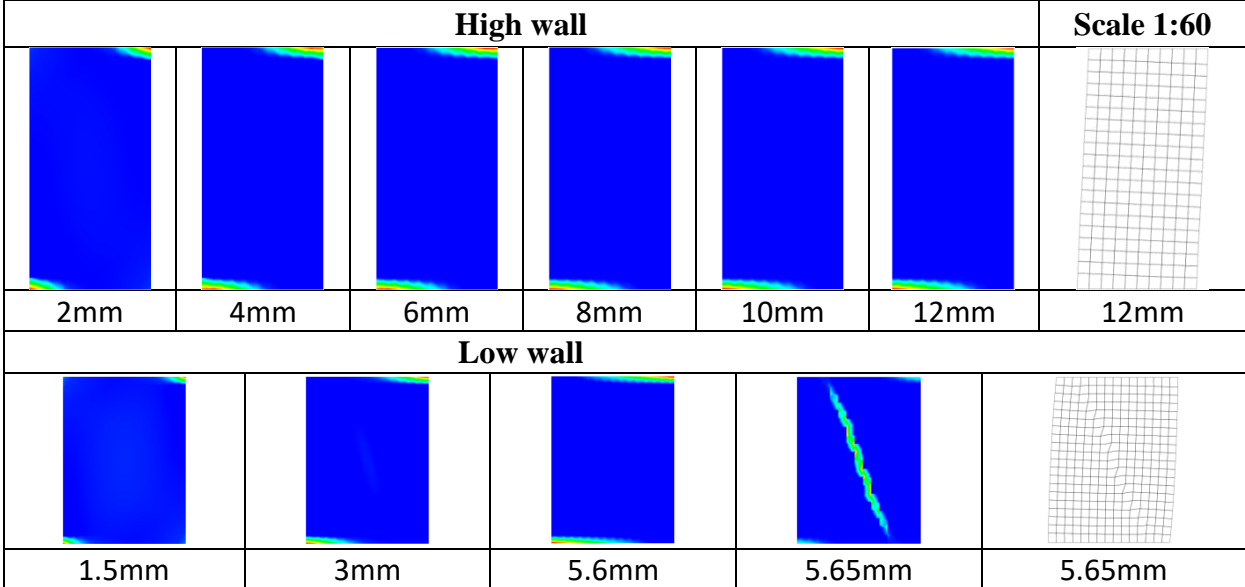
Figure 4-5 Crack propagation for increasing values of lateral displacement and final deformed shapes of the walls.

For the FFM, the crack propagation during the nonlinear analysis can be visualized by monitoring the axial stresses at the integration points located at the extreme sections of the panel. In section 4.1.3.1 this has been done for a short wall failing in flexure (TUD_COMP-0a) and a long wall (TUD_COMP-4) failing in shear. To demonstrate the incapability of the beam elements to capture the shearing failure mode the obtained stress distributions at the extreme section have been compared with those obtained with the TZ-CM (section 4.1.3.1).

4.1.2.2 Sensitivity analyses

Two types of sensitivity analyses are performed, first the influence of the mesh size and the integration scheme in the area of the cross section on the FFM is analysed and second, the effect of the estimated reference masonry fracture energy on the TZ-CM will be discussed.

4.1.2.2.1 Influence of mesh size and integration scheme on fibre flexure model

For the beam elements a variation study is made between one beam element, two beam elements and three beam elements, distributed over the height of the masonry panel and representing the high wall tested in Pavia for ISPRA. Only FFM-a has been considered, as this model allows easily a mesh sensitivity analysis (i.e. all finite elements have the same material properties). To investigate the effect of the integration scheme in the area of the cross

section, the adopted Simpson integration rule in the area of the two control sections ranges from 3 to 11 integration points over the cross sectional height. The effect on the peak strength and ultimate displacements will be illustrated by displaying both the force-displacement curves and stress distributions at extreme sections.

Figure 4-6 present the force-displacement curves for the ISPRA high wall adopting one beam element, two beam elements and three beam elements. The picture clearly shows that the 3 point Simpson integration scheme is not suitable for a nonlinear analysis, as it dramatically overestimates the peak strength of the masonry panel. Furthermore, one beam elements overestimates the member strength (Figure 4-6a), since the Gaussian integration scheme does not include the end sections in which the highest forces are present.

Material properties	Model	f_{jt}	G^I_{f-jt}
	FFM-a	0.04	0.05
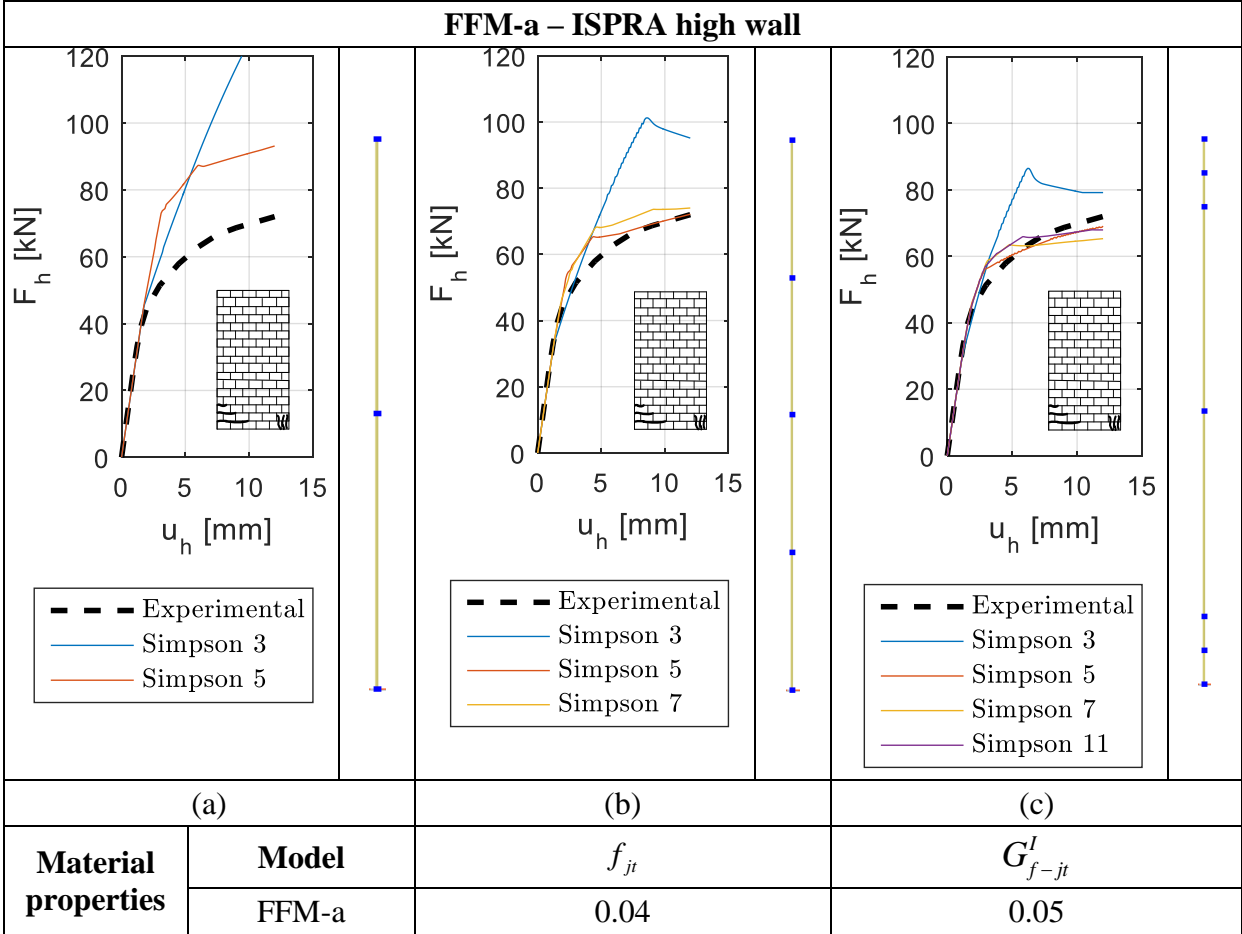
Figure 4-6 Influence of the mesh size and the adopted Simpson numerical integration scheme on the FFM accuracy: 1 beam element (a), 2 beam elements (b) and 3 unequally distributed beam elements (c).

By selecting two beam elements over the height of the masonry panel the result is improved (Figure 4-6b). This is explained by the fact that the control sections of the beam elements are closer to the top and bottom base. Another mesh refinement in which two smaller beam elements at the top and bottom are combined with one greater beam element in the middle result in an almost perfect fit with the experimental results. Figure 4-6 it can be concluded

that an increase in the number of integration points over the height of the beam elements and the localized mesh refinement technique provides better results.

In order to visualize the effect of the number of integration points over the height of the beam element, the section stress distribution for both the 3 points and 11 points Simpson integration rule has been examined. To this end, at each load step the stresses along the beam axis in each fibre (integration point) have been extracted from DIANA and were plotted in MATLAB (Figure 4-7).
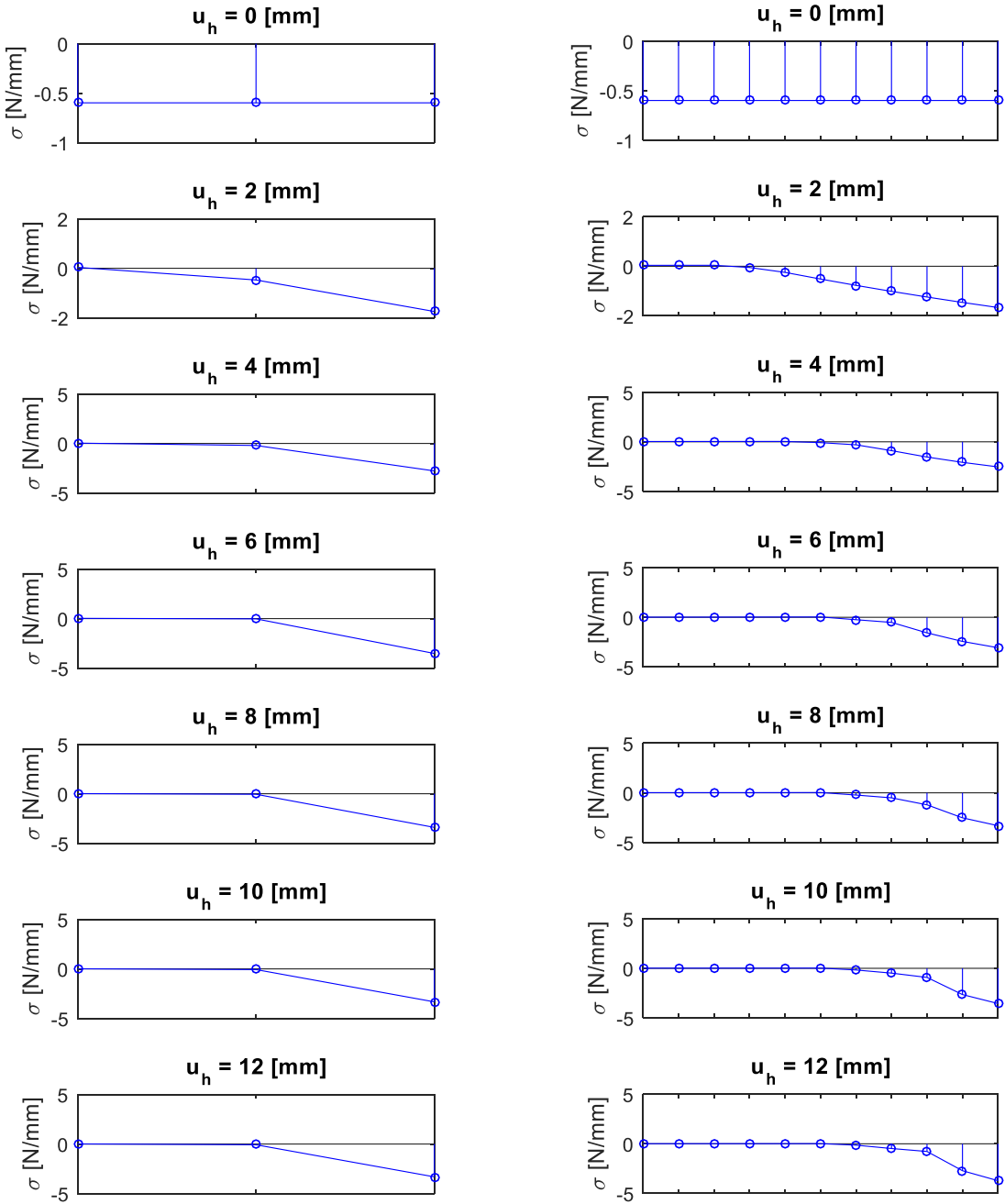
Figure 4-7 Section stress distribution at the base of the masonry wall for respectively 3 and 11 integration points over the height of the beam element – ISPRA high wall using 3 beam elements.

The figure graphically demonstrates how the stresses are distributed over the cross section and why a 3 points Simpson integration rule in the area of the cross section is not suitable in a nonlinear analysis.

4.1.2.2.2 Influence reference fracture energy on three zoned - continuum model

In the preceding section (4.1.2.1) it has been shown that on the one hand the TZ-CM shows good agreement with experiments but on the other hand resulted in an incorrect combination of lateral displacement and peak strength for the low wall. It appears to be that this combination is closely related to the estimated reference fracture energy, which physically means that it is related to the amount of energy that can be dissipated in the diagonal crack. Figure 4-8 graphically illustrates the effect of a decreasing reference fracture energy. It clearly displays that for a decreasing fracture energy the lateral drift at peak strength decreases and comes closer to the experimental data.

TZ-CM – ISPRA low wall				1:35	
				$u_h = 2.7$ Experimental (schematic)	
Model	**Mesh size**	f_{jt}	G^I_{f-jt}	f_{tu}	G^I_{f-tu}
	mm	MPa	N/mm	MPa	N/mm
TZ-CM	67.5	0.04	0.005	0.24	0.05-0.005
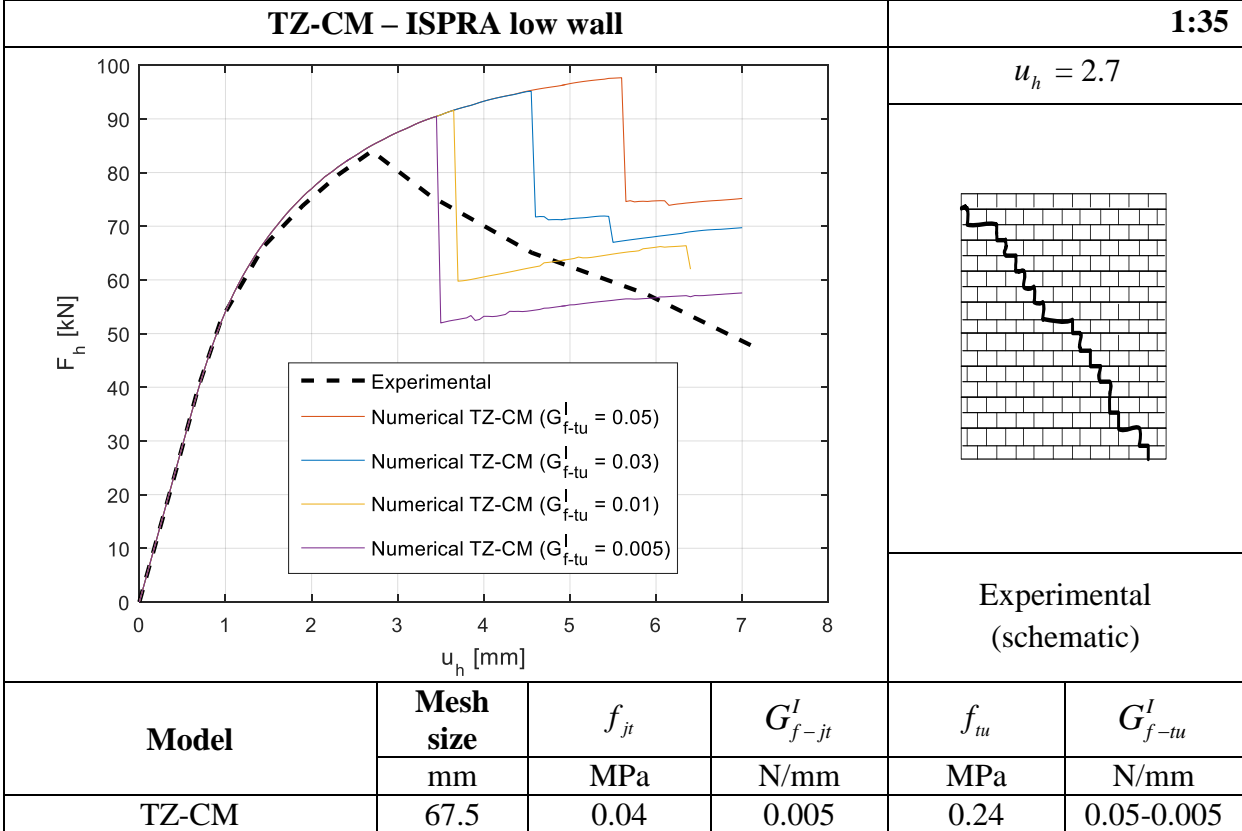
Figure 4-8 Influence of the unknown parameter of the TZ-CM, namely the reference masonry fracture energy.

4.1.2.3 Fibre flexure – lumped shear model

As discussed in section 3.3 the beam elements do require a modification to account for the shear failure mode. It was proposed to adopt a structural nodal interface in combination with a Coulomb friction model in which the material parameters (i.e. the shear strength c and friction μ) were modified and linked to the global strength parameters of the masonry panel.

Table 4-4 present the mentioned parameters, modified by the criteria presented in Table 3-3, referring to the Mann and Muller (1982) criterion $(\bar{c}, \bar{\mu})$, the correction (c_{mc}, μ_{mc}) proposed by Magenes and Calvi (1997) and the modification according to Abrams (1992) (c_a, μ_a).

Table 4-4 Input data for piers dominated by failure in shear. Parameters are calculated according to the equations presented in Table 3-3.

Name	$\dfrac{H_0}{H}$	α_v	p	Δx^*	Δy	φ	c	μ	$\bar{c}$	$\bar{\mu}$	c_{mc}	μ_{mc}	c_a	μ_a
	-	-	MPa	mm	mm	-	MPa	MPa	MPa	MPa	MPa	MPa	MPa	MPa
I-low wall	0.5	1.0	0.6	185*	55	0.59	0.23	0.58	0.17	0.43	0.10	0.26	0.16	0.27
* Δx is taken as the mean between the stretcher (250 mm) and the header (120), since the Ispra walls were built in English bond (alternate stretcher and header courses)														
H = height; H_0 = distance to zero moment; α_v = shear ratio; p = vertical pressure; Δ x = unit length; Δ y = unit height; φ = the interlocking parameter $\left(2\Delta_y / \Delta_x\right)$;														

As mentioned before, the structural nodal interface is placed between two adjacent beam elements and is located in the middle of the panel (Figure 4-9). When the Coulomb friction failure envelope is violated (section 3.3.1), a perfect plastic behaviour for the shear traction and consequently for the shear force is initiated (Figure 4-9).

FF-LSM – ISPRA low wall	**1:35**
	$u_h = 2.7$

	Numerical	Experimental (schematic)

Material properties	**Model**	f_{jt}	G_{f-jt}^{I}
	FF-LSM	MPa	N/mm
		0.04	0.05
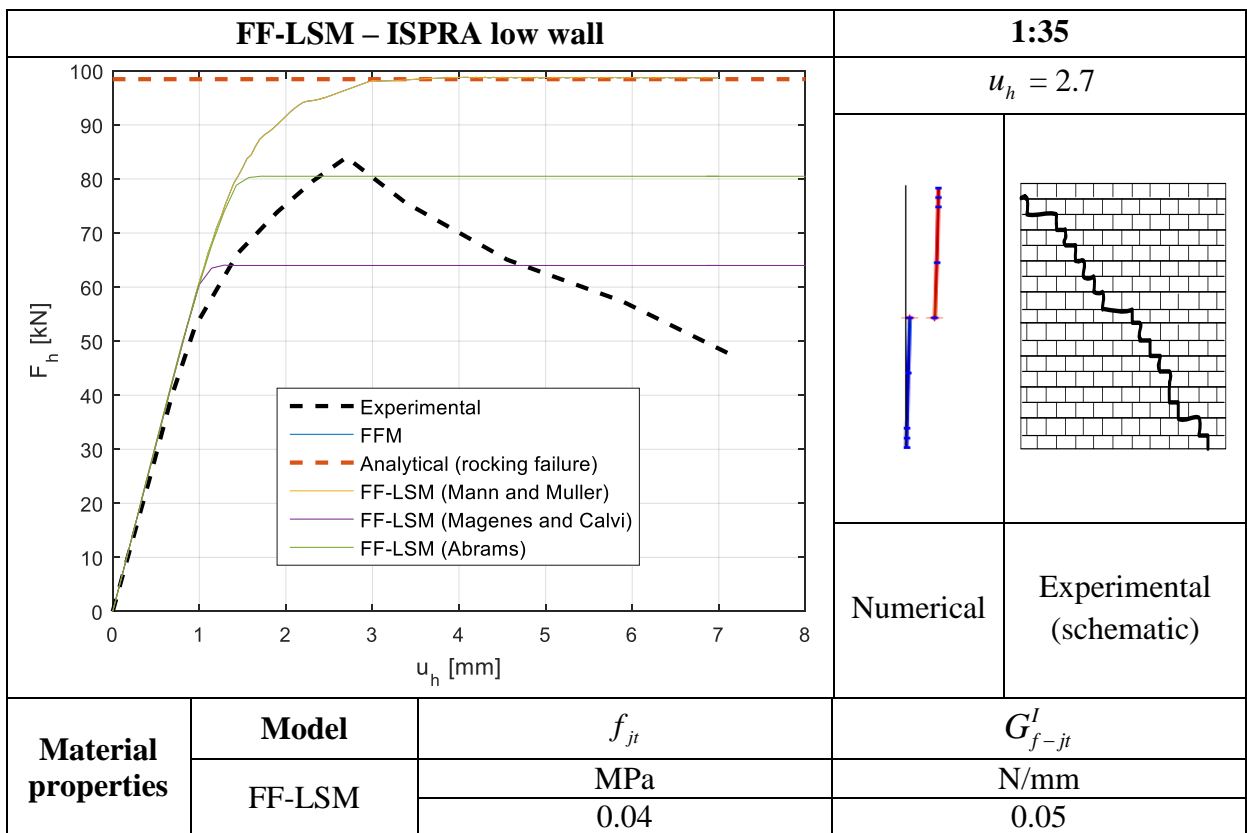
Figure 4-9 Force-displacement curves and lateral displacements for the FF-LSM – ISPRA low wall.

Figure 4-9 shows that the implementation of the above mentioned analytical shear strength criteria (section 3.3.1) yields reasonable predictions of the shear strength (numerical percent error within 20%), although in this case the shearing strength according to the Mann and Muller criterion was greater than the rocking strength, as shearing failure was not initiated adopting this criterion (Figure 4-9 – yellow line).

Optionally a panel collapse can be considered by a limitation of the ultimate drift. Specifying a linear softening diagram for both the shear strength and friction parameters, the element resistance gradually decreases to zero when a maximum deformation is violated (Figure 4-10). The maximum allowable deformation is generally referred to as the drift capacity (δ_u) and is dependent on the failure mode (e.g. piers failing in shear or flexure) and the shear aspect ratio of the pier. The limit value δ_u adopted here is 0.4 % (recommended by Eurocode 8 for piers failing in shear).

FF-LSM – ISPRA low wall		1:35

$u_h = 2.7$

| Numerical | Experimental (schematic) |

Material properties	Model	f_{jt}	G^I_{f-jt}	δ_u
		MPa	N/mm	%
	FF-LSM	0.04	0.05	0.4
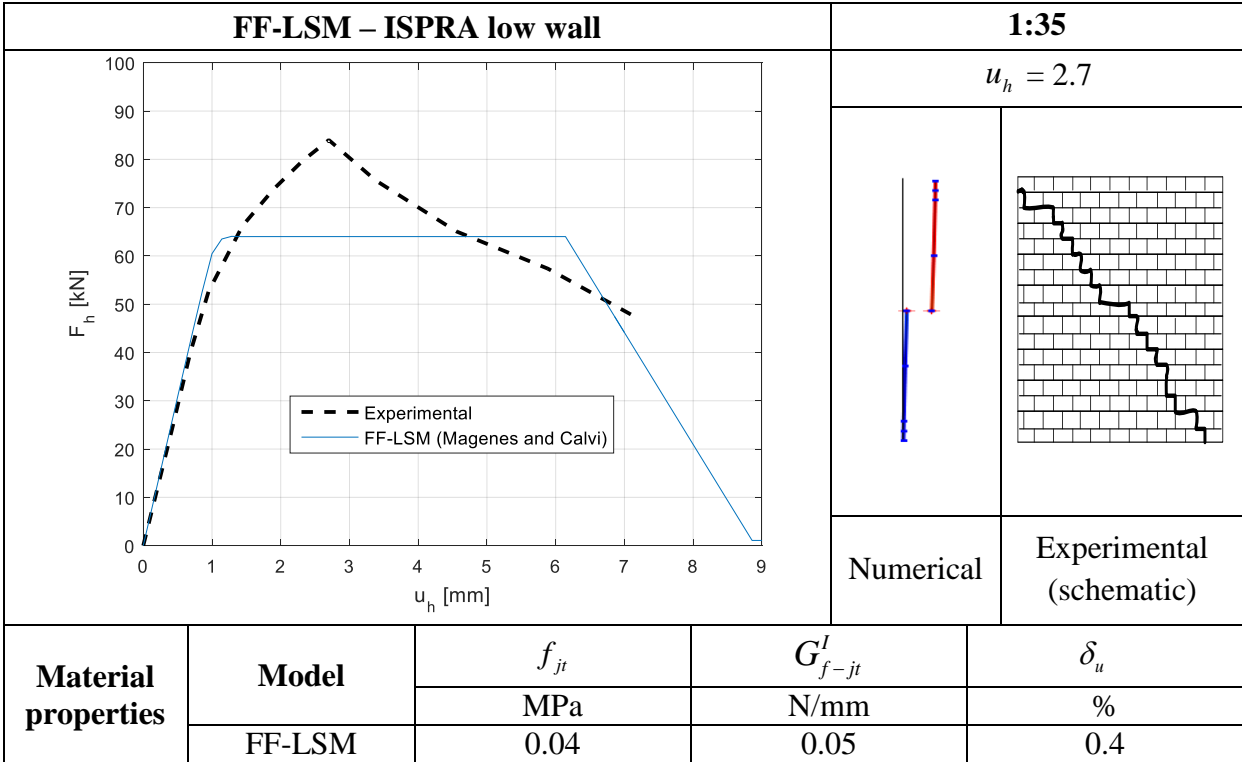
Figure 4-10 Force-displacement curves and lateral displacements for the FF-LSM combined with a drift limitation.

4.1.3 Results – masonry panels TU Delft

This section presents the numerical results of the TU Delft tests. The numerical prevailing failure modes and force-displacement curves will be compared with experimental data. Again, the analytical expression for the rocking failure mode has been added to the numerical load-displacement curves. Additionally, the stress distributions at the base of the masonry

56

panels for both the plane stress elements and beam elements are analysed. In order to find a range of application for the FFM, the numerical error as a function of the shear ratio will be investigated.

4.1.3.1 Continuum and Fibre flexure models

Figure 4-11 presents the numerical as well as the experimental backbone force-displacement curves for the short and long walls respectively. The experimental backbone curves are derived from the original cyclic curves and are created by combining the positive shear forces at the positive final displacement of each load cycle.

The analytical expression for the rocking failure mode (Figure 4-11 – green line) provides for most panels a lower bound, although for the cantilever walls (TUD_COMP 2 and TUD_COMP 6) some deviations are observed. Since the shear capacity according to the analytical formulation is based, among other things, on the assumption of an equivalent rectangular stress block with $\kappa = 0.85$, it may be concluded that this value may vary for different shear ratios, and should be slightly adjusted for walls with high slenderness (such as the tested cantilever walls).

As will be discussed later, the CM and TZ-CM resulted in the same prevailing failure modes. Consequently, no important deviations between these models in terms of final forces and final displacements were detected. However, especially for the FFM-a (Figure 4-11 – yellow line) differences between the cracking moment and the ultimate moment capacity can be observed. Because of a lower bed joint fracture energy for the top and bottom beam elements adopted in the FFM-b, these differences usually disappeared. In line with what has been observed for the ISPRA tests, for a decreasing shear ratio the numerical error of the FFM is becoming larger. Physically it can be explained by the fact that for a decreasing shear ratio, generally the masonry panels becomes more squat and shear failure will be governing. Since the beam elements are only capable of simulating failure in bending, the use of this type of elements has led to a dramatic overestimation for the long walls. In section 4.1.3.1.1 the influence of the shear ratio on the numerical error of the FFM will be examined in greater depth.

Figure 4-11 Force-displacement curves and schematic failure patterns for both the short and long walls.
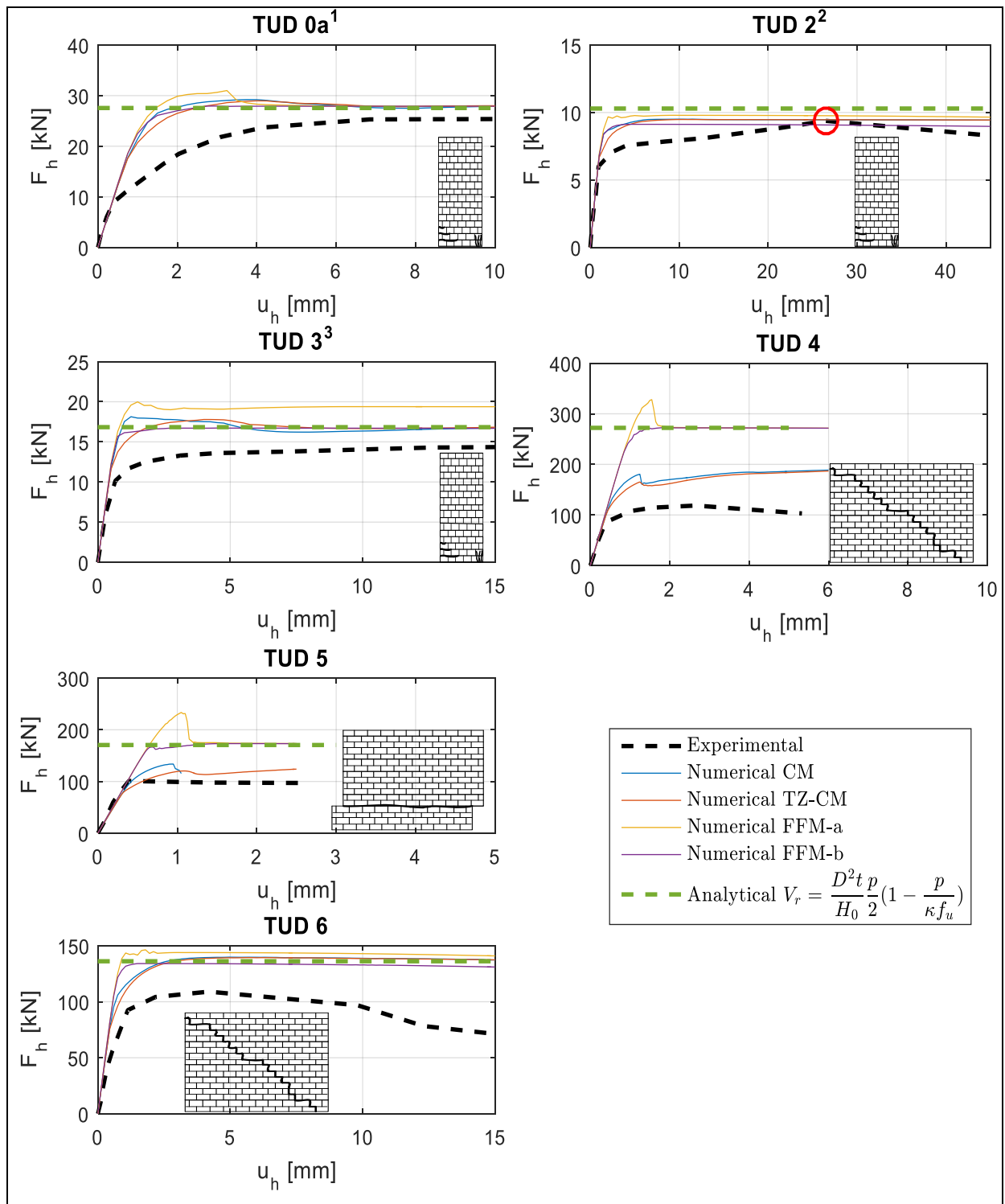
[1] x-axis is cut off to enhance the visualisation of the results.

[2] The red circle locates some values of forces obtained in the experiment which cannot be considered reliable (Ravenshorst & Messali, 2016).

[3] x-axis is cut off to enhance the visualisation of the results.

Model	Mesh size	f_{jt}	G_{f-jt}^I	f_{tu}	G_{f-tu}^I
	mm	MPa	N/mm	MPa	N/mm
CM and FFM-a	150	0.18	0.05	-	-
TZ-CM and FFM-b	150	0.18	0.005	0.13	0.05

Figure 4-12 provides the principal total tensile strains E1 at the last load step for the TZ-CM. With the exception of TUD_COMP-5 and TUD_COMP-6, all other failure modes shared similarities with those observed in the experiments. TUD_COMP-5 showed diagonal cracks instead of a sliding failure along the bottom joints in the test and TUD_COMP-6 demonstrated a rocking failure, while in the experimental test a diagonal crack along the joints was observed. For the TU Delft tests, the CM produced for all case exactly the same prevailing failure mode as found with the TZ-CM. Apparently, in this case the tensile resistance of the regions undergoing diagonal cracking is almost equal to the tensile resistance of the bed joints. This conclusion is also supported by the fact that the ratio between the reference masonry tensile stress and the bed joint tensile stress is equal to $0.13/0.18 = 0.72$, whereas for the ISPRA tests this ratio is much higher, namely $0.24/0.04 = 6$.
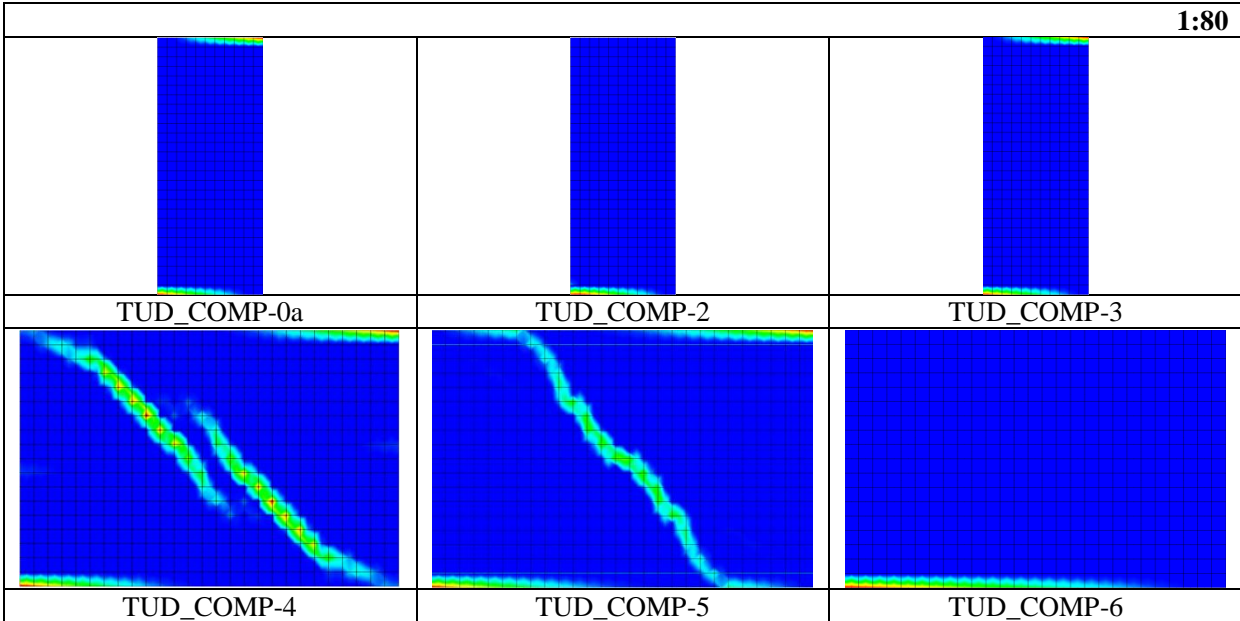
Figure 4-12 Experimental failure modes and principal total strains E1 at the last load step – undeformed shapes.

One significant property that easily visualizes the differences between plane stress elements and fibre beam elements is the vertical stress distribution (σ_{yy}) at the base of a masonry panel (Figure 4-13). Besides, as previously stated, it can be used as a tool to depicture the crack propagation during the nonlinear analyses and clearly demonstrates that the axial stresses in the FFM are not affected by the stresses in the lateral direction. The pictures are created by extracting the vertical stresses at the location of the integration points for the beam elements, whereas for the plane stress elements they are extracted at the location of the nodes. The black line and the red line represent the stress distribution of the TZ-CM and FFM, respectively.
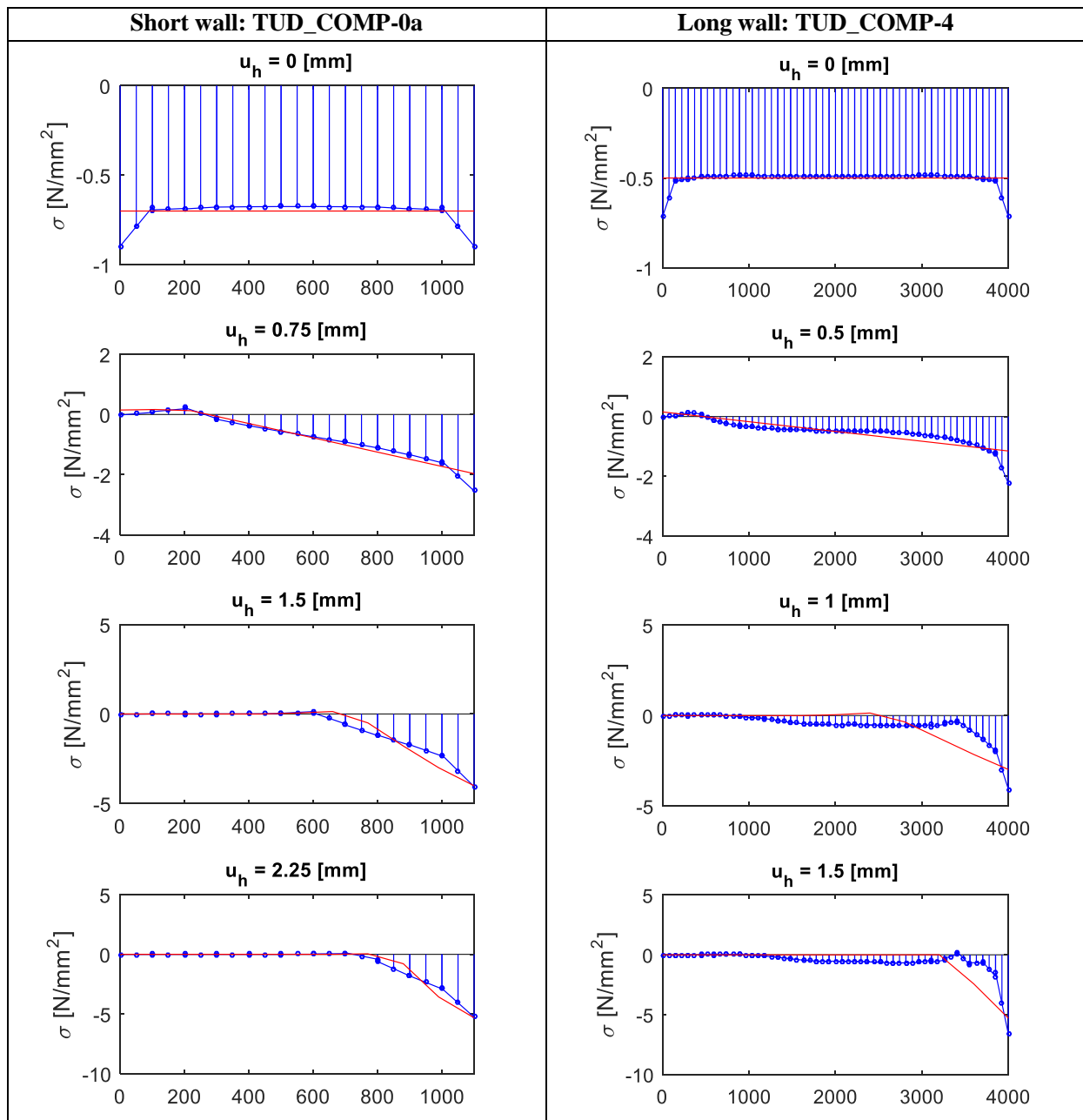
Figure 4-13 Section stress distribution at the base of the masonry wall TUD_COMP-0a and TUD_COMP-4 for the FFM (red line) and TZ-CM (blue).

From this figure it can be seen that the beam elements describe the stress distribution at the base properly and are in good agreement with the plane stress results in case of flexural failure (Figure 4-13 - TUD_COMP-0a). However, in case of the long wall, once the panel fails in shear and the diagonal crack shows up, some distortions of the stress distribution (Figure 4-13 - TUD_COMP-4) can be observed for the plane stress elements. As a result of a critical combination of shear and tensile stresses the integrations points at the lower right corner are cracked and consequently, the vertical stress (σ_{yy}) has dropped to zero. Figure 4-13 clearly shows that this phenome cannot be simulated by the beam elements, as they show a stress distribution that belongs to a rocking failure mode (red line).

4.1.3.1.1 Influence of the shear ratio

As experimental tests on unreinforced masonry panels are expensive, and usually comprise no other type of boundary conditions than cantilever or fixed-fixed, Gambarotta and Lagomarsino (1996) developed a constitutive model for solid brick masonry that showed good agreements with measurements and therefore allows a parametric investigation. Adopting this model and performing many finite element calculations in which the mechanical parameters, the boundary conditons (fixed-fixed or cantilever), the dimensions and the magnitude of the axial stress were varied, Magenes and Calvi (1997) discovered that it is especially the shear ratio $\alpha_v = M/(VD) = H_0/D$ that influences the shear capacity of a masonry panel subjected to a shear-compression state of stress. Varying the shear ratio and keeping all the other parameters constant it was proven that, somehow, the shear capacity is not affected by the type of failure mode. In this way it was shown that the relation between the shear ratio and the reciprocal of the shear strength $\tau_u = V_u/(Dt)$ is almost perfectly linear. However, the test samples within the TU Delft physical testing program were epxosed to different levels of vertical pressure. Nevertheless, by dividing the shear strength with the vertical pressure an attempt is made to find a better correlation between the shear ratio and the shear strength of the masonry panels. Therefore, whereas Magenes and Calvi (1997) presented the mean shear strength (Table 4-5) as the characterization of the shear capacity of a masonry panel, in this section also the normalized mean shear strength (Table 4-5) will be proposed. Together with all the other parameters the definition of the normalized mean shear strength is presented in Table 4-5. In this section only the TZ-CM and the FFM-b were used, since it were these model that best predicts the true behaviour of masonry.

Table 4-5 Definitions

Property	Symbol	Definition	Unit
Shear ratio	α_v	H_0/D	-
Mean shear strength	τ_u	V_u/Dt	MPa
Reciprocal mean shear strength	τ_u^{-1}	$1/\tau_u$	mm^2/N
Normalized mean shear strength	-	τ_u/p	MPa
Reciprocal normalized mean shear strength	-	p/τ_u	MPa
Numerical percent error	δ	$\left|(\tau_u - \tau_{u;beam})/\tau_u\right| \times 100\%$	%

In Figure 4-14 both the reciprocal of the experimental mean shear strength and the reciprocal of the normalized experimental mean shear strength are plotted against the shear ratio. The figure clearly demonstrates that this relation is not independent of the applied vertical

pressure, which is in fact in line with existing analytical theories. However, the picture also illustrates how an almost perfect correlation is found for the reciprocal of the normalized experimental mean shear strength. There are two conclusions to be drawn from this: first, the shear strength is almost linear related to the vertical pressure and second, the influence of the shear ratio on the shear strength is not affected by the type of damage propagation.
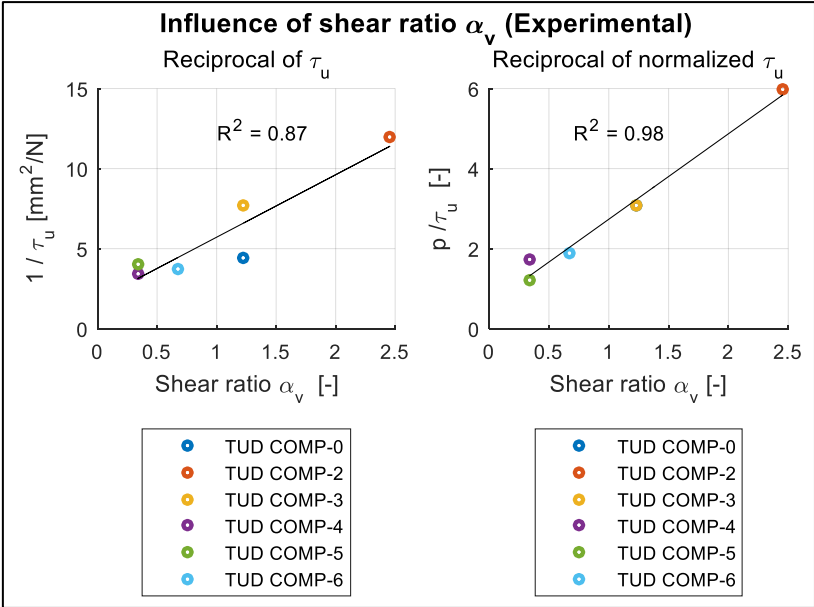
Figure 4-14 Relation between the shear ratio α_v and the reciprocal of the (normalized) experimental mean shear stress τ_u .

Figure 4-15 illustrate that this relation also exist for the relatively simple TZ-CM and FFM, something that will be used to depicture the numerical error of both models.
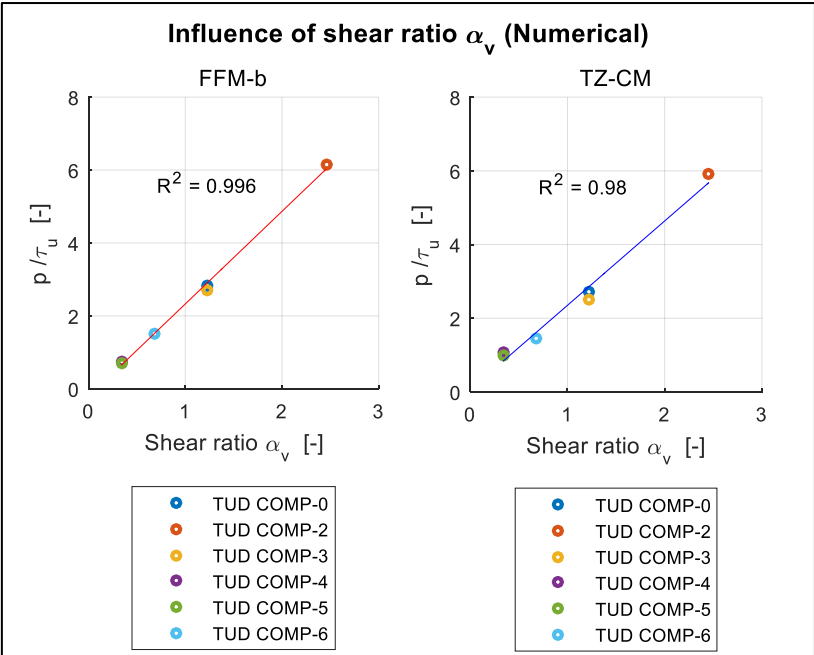
Figure 4-15 Relation between the shear ratio α_v and the reciprocal of the normalized numerical mean shear stress τ_u .

The combination of the regression lines of the experimental, the numerical TZ-CM and the numerical FFM-b results provides a good insight into the behaviour of the latter two models (Figure 4-16). Especially from the quadratic regression lines (Figure 4-16b), which were obtained by taking the reciprocal of the linear regression functions (Figure 4-16a), it can be seen that for a decreasing shear ratio the numerical error of the FFM amplifies explosively.
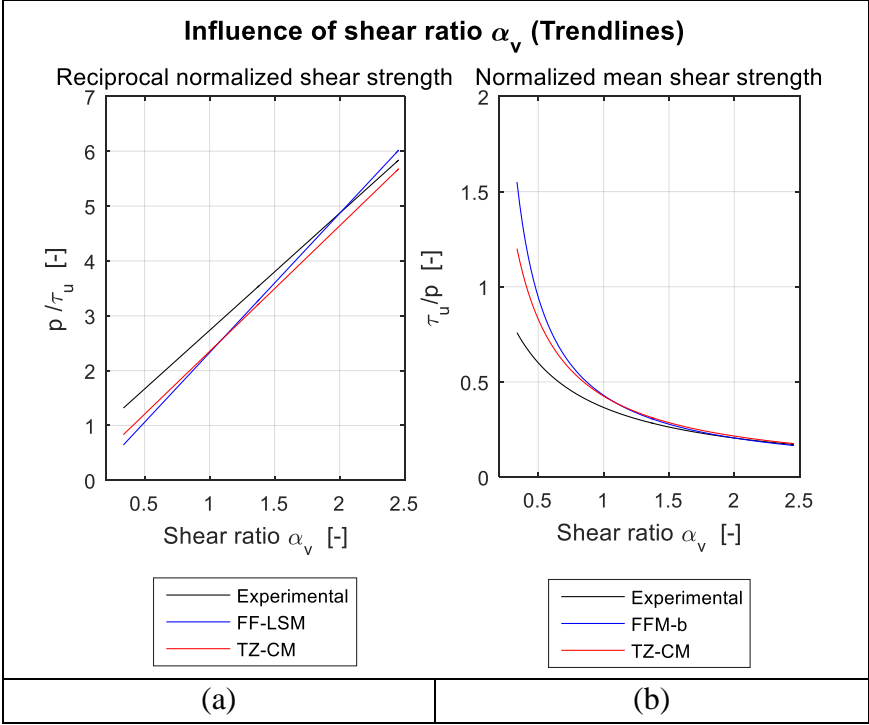
Figure 4-16 Relation between the shear ratio α_v, the experimental mean shear stress and the normalized numerical (beam and continuum) mean shear stress.

The calculation of the numerical percent error, making use of the quadratic regression functions of the black and blue line (Figure 4-16), representing the numerical and the beam element data respectively, provides insight into the size of the numerical percent error (Figure 4-17a). Since the FFM-b model tends to underestimate the shear strength for high shear ratios, the linear regression lines have a point of intersection (Figure 4-16a). For this reason it seems that at some point the numerical error is equal to zero (Figure 4-17a), which of course is not the case in reality. The problem could be solved by calculating the numerical percent error for every masonry panel separately. Fitting a quadratic regression model to the data points (Figure 4-17b), representing the numerical percent error, a similar picture can be obtained. Both pictures clearly show that there is a critical shear ratio below which the FFM should not be used to avoid a dramatic overestimation of the shear strength.
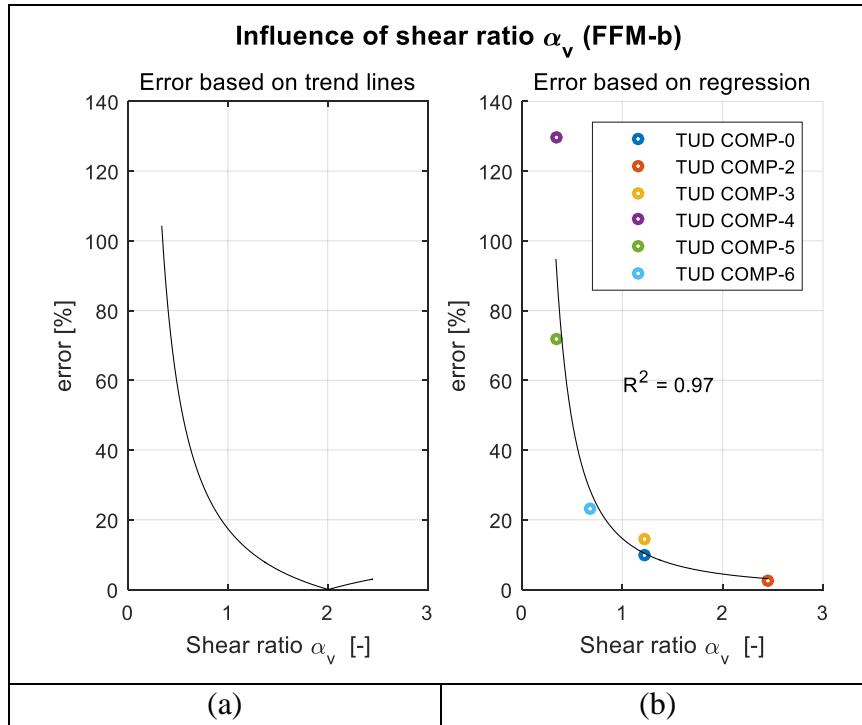
Figure 4-17 The numerical percent error of the beam element model as a function of the shear ratio based on the trend lines (Figure 4-16) and on regression.

4.1.3.2 Fibre flexure – lumped shear model

Again, the structural nodal interface in combination with a Coulomb friction model has been adopted to obtain a better correlation between the FFM and experimental results. Table 4-6 presents the material parameters, modified by the criteria presented in Table 3-3, referring to the Mann and Muller (1982) criterion $(\bar{c}, \bar{\mu})$, the correction (c_{mc}, μ_{mc}) proposed by Magenes and Calvi (1997) and the modification according to Abrams (1992) (c_a, μ_a).

Table 4-6 Input data for TU Delft panels dominated by failure in shear. Parameters are calculated according to the equations presented in Table 3-3.

Name	$\frac{H_0}{H}$	α_v	p	Δx	Δy	φ	c	μ	$\bar{c}$	$\bar{\mu}$	c_{mc}	μ_{mc}	c_a	μ_a
	-	-	MPa	mm	mm	-	MPa	MPa	MPa	MPa	MPa	MPa	MPa	MPa
TUD-4	0.5	0.3	0.5	212	70	0.66	0.14	0.43	0.11	0.33	0.08	0.25	0.13	0.27
TUD-5	0.5	0.3	0.3	212	70	0.66	0.14	0.43	0.11	0.33	0.08	0.25	0.12	0.24
TUD-6	1.0	0.7	0.5	212	70	0.66	0.14	0.43	0.11	0.33	0.07	0.20	0.11	0.23

Figure 4-18 depictures the force displacement curves adopting the FF-LSM to account for possible shear failure modes. Only those masonry panels have been considered for which shear failure was governing and drift limitations have been omitted for the sake of simplicity. While the FFM without the nodal interface simply determines the ultimate rocking strength of the masonry panel (Figure 4-18 – blue and red line) and consequently overestimates the

64

ultimate shear strength, the FF-LSM including the nodal interface is able to correctly predict the shear capacity of the masonry panel, although the observed level of accuracy is highly dependent on the adopted shear failure criterion.
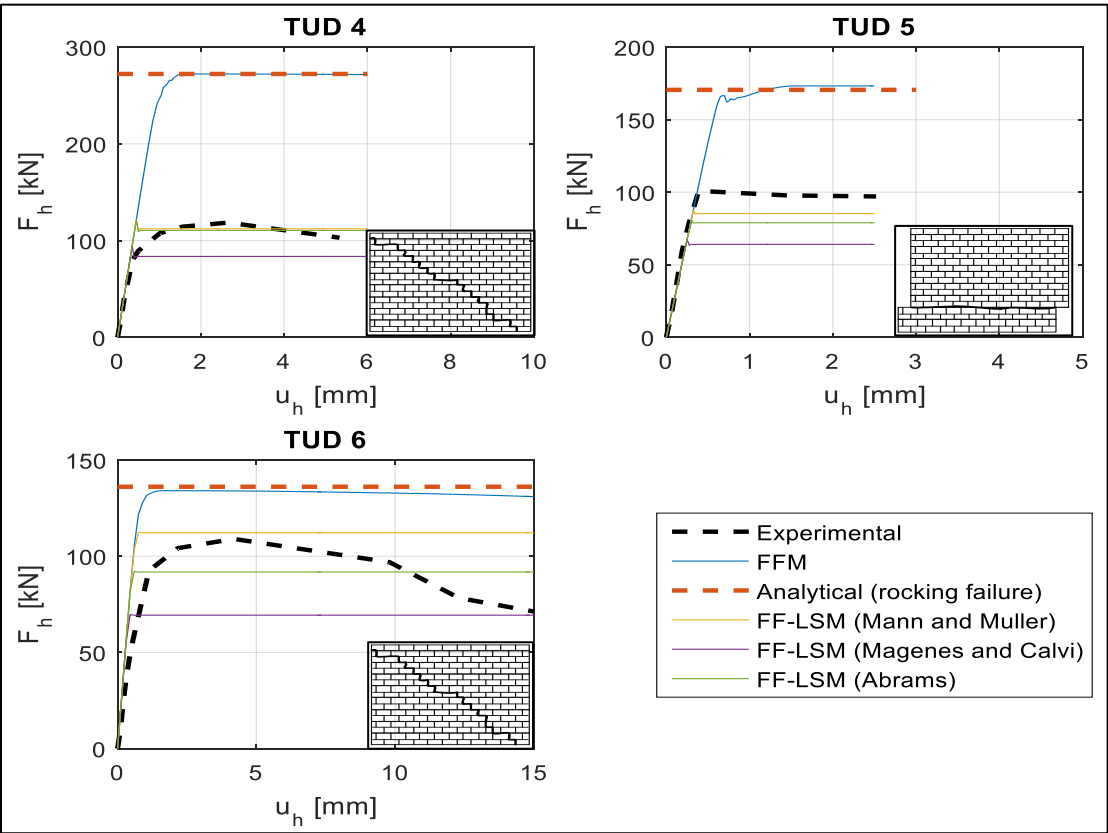
Figure 4-18 Force-displacement curves and schematic failure patterns for the FF-LSM – TU Delft long walls.

4.1.3.2.1 Influence of the shear ratio

As outlined above, the accuracy of the FF-LSM is mainly determined by the adopted shear failure criterion. Therefore, to assess the accuracy of the adopted models, again the influence of the shear ratio upon the numerical percent error has been investigated. Considering the normalized mean shear strength (Figure 4-19) and the numerical percent error (Figure 4-20) as functions of the shear ratio it can be observed that both the Mann and Muller and the Abrams criteria are rather accurate (percent error within 20%), although the Mann and Muller criterion is somewhat unconservative (Figure 4-19). Especially for a decreasing shear ratio the criterion developed by Magenes and Calvi appeared to be less precise (Figure 4-20), although the criterion can be safely adopted in engineering practice as it is relatively conservative (Figure 4-19).

Mann and Muller criterion	**Magenes and Calvi criterion**	**Abrams criterion**
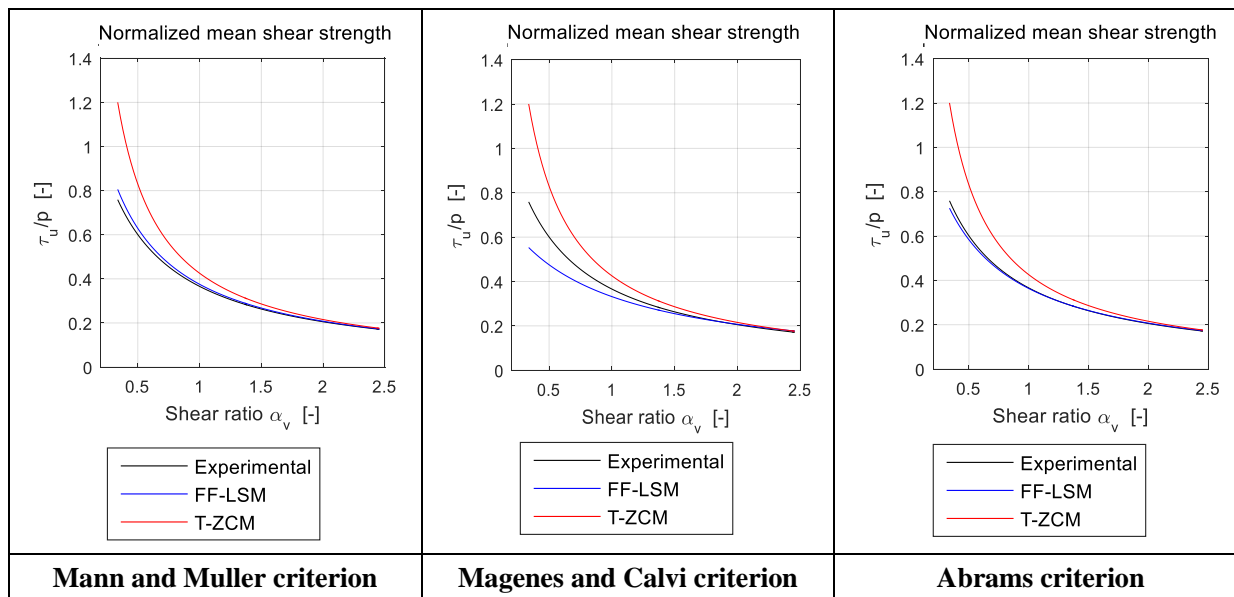
Figure 4-19 Relation between the shear ratio α_v, the experimental mean shear stress and the normalized numerical (FF-LS and TZ-CM) mean shear stress

Mann and Muller criterion	**Magenes and Calvi criterion**	**Abrams criterion**
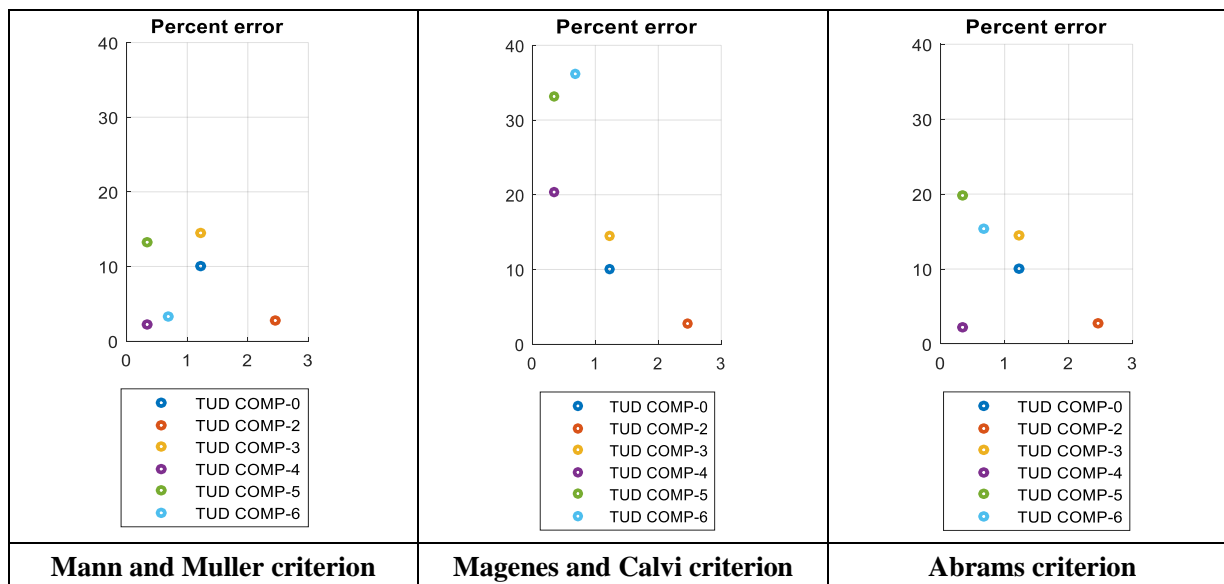
Figure 4-20 The numerical percent error of the FF-LSM model as a function of the shear ratio.

66

4.2 Two-storey masonry façade Pavia

In order to assess the numerical model capabilities in analyses of full-scale brick masonry walls with openings, a two storey building experimented by Magenes and Calvi (1994) at the University of Pavia will be considered. The URM building, having a rectangular shaped floor plan of 6 x 4.4 m and a height of 6.4 m, consists of two longitudinal walls (''wall D'' – or ''door wall'' – and ''wall B'' or ''window wall'') and to transverse walls (''wall A'' and ''wall C''). While the window wall (wall B) is connected to the adjacent transverse walls by means of an interlocking brick pattern around the corner, the door wall (wall D) is disconnected from both transverse walls and can therefore be interpreted as being an independent in-plane test.

The longitudinal walls are subjected to four concentrated cyclic horizontal forces located at the floor level by means of four displacement-controlled screw jacks, representing the seismic forces activated during seismic action. The horizontal displacements that had to be applied at each jack were deduced from an earlier shake table test on a scaled version of the building. Given that the two floors carry approximately 60% of the total mass of the building, the total response of the scale model was governed by the behaviour of the two floor diaphragms. As both floors were subjected to the same vertical load, the horizontal peak accelerations at these positions tended to be equal. Consequently, the forces generated at level of the mass of the building (at the two floor levels) had the same magnitude. For this reason, while the top displacement was controlled, the four horizontal point loads representing the seismic action (Figure 4-21) were kept equal during the full-scale experiment.
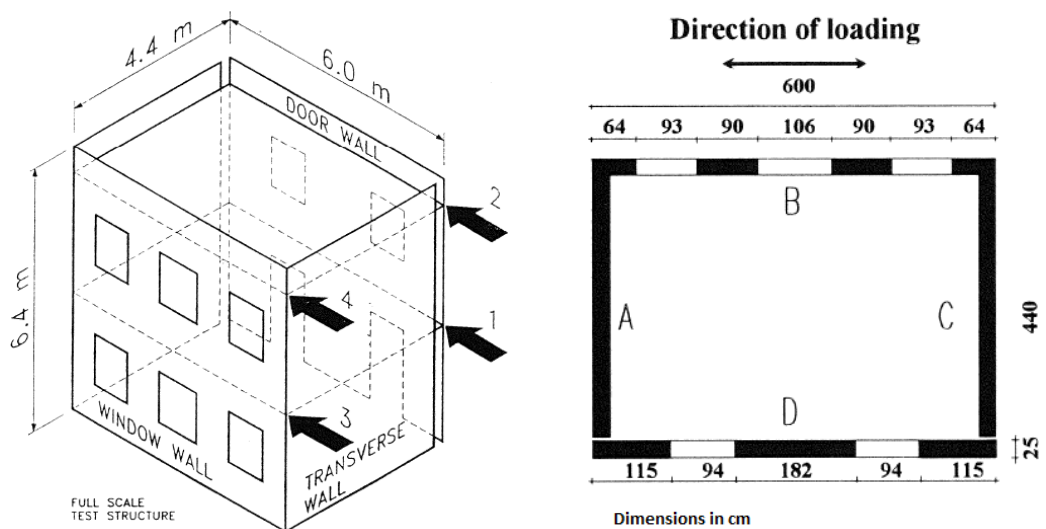
Figure 4-21 The full scale test structure including loading conditions (a) and the floor plan (b).

Besides, in order to produce a vertical stress ranging from 0.4-0.5 MPa at the reduced section between the openings level at the ground floor, concrete blocks were applied, producing a vertical load of 10 kN/m^2 on both the first and second floor.

Since the work was initially restricted two the in-plane behaviour of masonry and involved exclusively the analysis of two-dimensional structures, only the door wall (wall D) will be considered as a benchmark to evaluate the behaviour of the continuum as well as the equivalent frame models.

4.2.1 Input

In line with Chapter 3 three models will be adopted for the analysis of the Pavia door wall, the CM, the TZ-CM and the FFM in which the structural members (e.g. piers and spandrels) are represented by series of beam elements having the same tensile strength and corresponding fracture energy. The application of the FF-LSM, including interface elements to describe shear failure, will be discussed later in this section. Whereas for the continuum models the finite element mesh reproduces the original in-plane geometry of wall D, for the equivalent frame models the in-plane geometry of wall D is idealized as a frame consisting of piers, spandrels and rigid nodes (section 2.3.3). By the damage survey after earthquakes and experimental campaigns certain criteria can be assumed to identify the main structural components: i.e. piers and spandrels. Regardless of the method the equivalent frame idealization is based on three steps, from the identification of spandrels (step 1) to the identification of piers (step 2) to that of nodes (step 3) (Figure 4-22).
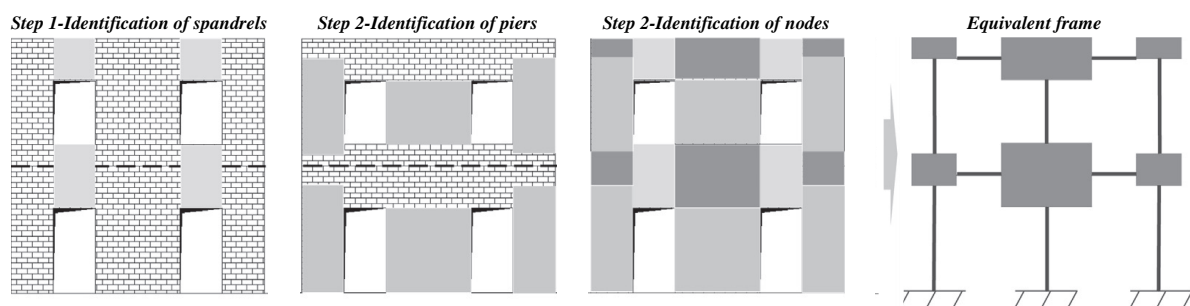
Figure 4-22 Equivalent frame idealization of the door wall. (Lagomarsino, 2013).

In this work a commonly adopted criterion for the pier height is assumed (Dolce, 1989): a maximum 30 degrees inclination of the cracks starting from the opening corners and consistently providing an increased height for the external piers. If the adjacent openings are at the same level, as in the case of the internal pier and the spandrels, the height is assumed to be equal to that of the opening. The original geometry, applied loads, the equivalent frame

idealization and cross sectional properties are presented in Figure 4-23. Furthermore, the pier heights calculated according to the theory of Dolce (1989), the assumed shear span $\left(H_0/H\right)$ and the resulting shear ratios necessary for the shear failure implementation are given. Initially it is assumed that the piers are situated in a double clamped condition $\left(H_0/H = 0.5\right)$, although it is expected that especially if spandrel failure is initiated this assumption is not totally correct and should be slightly adjusted. Therefore, to study the effect of the shear ratio, several analyses will be performed in which the shear span will be determined in a posteriori process which in turn can be used as input for an updated analysis.

Pier Label	D	t	h	λ	$\frac{H_0}{H}$	α_v
	[mm]	[mm]	[mm]	-	-	-
P1	1150	250	2477	2.15	0.50	1.08
P2	1820	250	2145	1.18	0.50	0.59
P3	1150	250	2477	2.15	0.50	1.08
P4	1150	250	1899	1.65	0.50	0.83
P5	1820	250	1235	0.68	0.50	0.34
P6	1150	250	1899	1.65	0.50	0.83
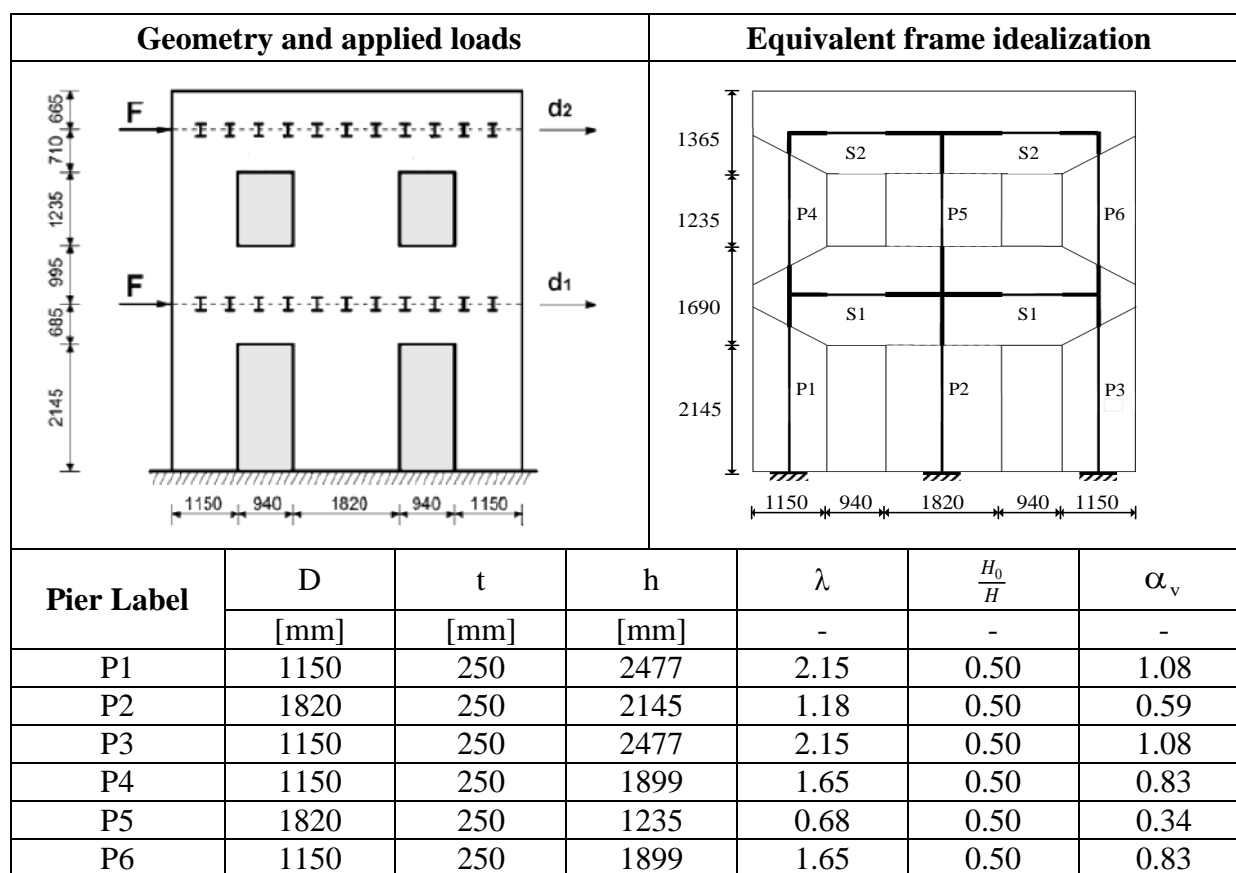
Figure 4-23 Geometry and applied loads (a) and equivalent frame idealization of the door wall (b); pier height determination according to Dolce (1989) for the Pavia door wall (Demirel, 2010).

The finite element meshes of the TZ-CM and the FFM, reproducing the in-plane geometry of the façade and the equivalent frame idealization respectively, are presented in Figure 4-24. The TZ-CM consists of 973 quadrilateral (Figure 4-24-green) and 168 trilateral plane stress elements (Figure 4-24-yellow), respectively representing the areas in which diagonal and flexure cracking may occur. The average finite element mesh size is approximately equal to 200 mm. For simplicity it is assumed that the impact of the wooden lintels located above the openings on the total wall resistance can be neglected and therefore they are not modelled.

The FFM is composed by 82 numerically integrated beam elements, consequently idealizing the structural response as purely flexural. The structural components (e.g. piers and spandrels) are represented by series of nonlinear beam elements; i.e. one smaller beam element at top and bottom and equally sized elements in between (Figure 4-24). The rigid nodes are modelled by means of relatively stiff beam elements, ensuring that these areas behave as rigid bodies. For the continuum models the displacements of the nodes along the base line are horizontally and vertically restrained, while the horizontal displacements of the nodes located at each floor are coupled, describing the clamped boundary conditions at the bottom and the force transmission, respectively. For the equivalent frame models this type of boundary condition is simply obtained by restraining the three nodes at the bottom edge horizontally, vertically and rotationally (Figure 4-24).

Imposed loads on the structure initially include the masonry dead load and the uniformly distributed loads at first and second floor resulting from the gravity loads on the first and second floor (p_1=20.7 kN/m and p_2 = 19.8 kN/m). A steel beam, horizontally tied at each floor and subjected to an imposed lateral monotonically increasing displacement at midspan is adopted, maintaining the resulting forces at the two floor levels equal during the displacement controlled analysis (Figure 4-24).
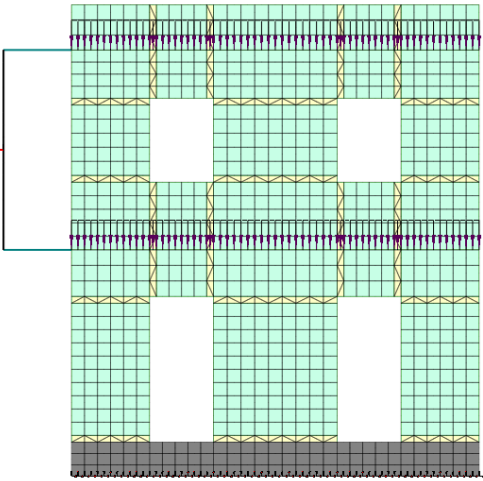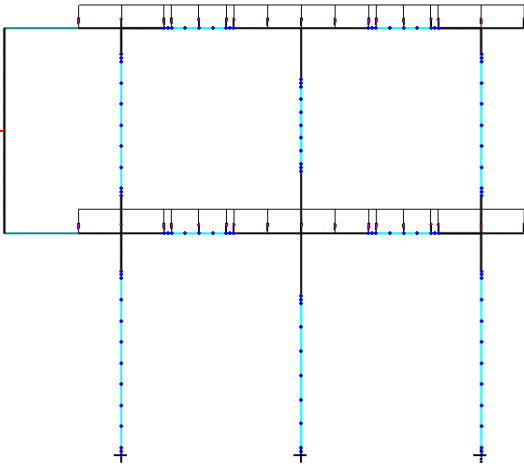
Three zoned - continuum model (TZ-CM)					Fibre flexure model (FFM)				
Piers	flexure	yellow	f_{jt}	G^I_{f-jt}	Piers	flexure	blue	f_{jt}	G^I_{f-jt}
	shear	green	f_{tu}	G^I_{f-tu}					
Spandrels	flexure	yellow	f_{ts}	G^I_{f-tu}	Spandrels	flexure	blue	f_{ts}	G^I_{f-tu}
	shear	green	f_{tu}	G^I_{f-tu}					

Figure 4-24 Finite element meshes for the TZ-CM as well as for the FFM and adopted parameters.

The material parameters considered for the numerical analyses are presented in Table 4-7 and have been partially obtained from Magenes et al. (1995) and partially from Magenes and Calvi (1997). The equivalent tensile strength of the spandrels f_{ts} located at first and second floor, representing the flexural property of the spandrel element, are calculated being the cohesion and friction coefficient equal to 0.23 and 0.58 MPa, respectively; the interlocking parameter for the spandrels is equal to 0.86 and obtained from Cattari and Beyer (2015); the mean vertical stress is equal to 0.2 MPa at first floor and 0.1 MPa at second floor; the clamping stress is estimated to be 65 % of the mean vertical stress present at first and second floor $(\gamma = 0.65)$. Since no experimental information for the reference masonry tensile strength f_{tu} was available, different values of f_{tu} have been assumed to perform a thorough examination of the parameter sensitivity.

Table 4-7 Material properties Pavia building.

Property	Symbol	Unit	Case 3: University of Pavia tests Mean
Joint tensile strength	f_{jt}	MPa	0.04
Bed joint initial shear strength (cohesion)	c	MPa	0.23
Bed joint shear friction coefficient	μ	-	0.58
Reference masonry tensile strength (1)	f_{tu}	MPa	-
Compressive strength of mortar	f_m	MPa	3.0
Spandrel tensile strength (2)	f_{ts}	MPa	0.32/0.26
Young's modulus	E_2	MPa	1410
Poisson ratio	ν	-	0.2
Reference masonry fracture energy tensile mode-I (3)	G_{f-tu}^{I}	N/mm	0.02
Fracture energy tensile mode-I (4)	G_{f-jt}^{I}	N/mm	0.005
Fracture energy in compression for loading perpendicular to bed joints (5)	G_{f-m}	N/mm	10

Note:
  (1) unknown for Pavia full scale test
  (2) calculated being the cohesion and friction coefficient equal to 0.23 and 0.58 MPa, respectively; the interlocking parameter for the spandrels is equal to 0.86 and obtained from Cattari and Beyer (2015); the mean vertical stress is equal to 0.2 MPa at first floor and 0.1 MPa at second floor; the clamping stress is estimated to be 65 % of the mean vertical stress ($\gamma = 0.65$)
  (3) estimation
  (4) tensile bond behaviour of masonry: estimation based on Van der Pluijm (1992)
  (5) evaluated 500 times larger than the tensile fracture energy G_{f-t}^{I}

4.2.2 Results

In this section a comparison is made between numerical and experimental failure patterns and load-displacement curves. All four models proposed in Chapter 3, the CM, the TZ-CM, the FFM and the FF-LSM are considered and examined thoroughly. Besides, a mesh sensitivity analysis on the FFM is performed.

As this work is limited to examining the masonry structure response by means of nonlinear static monotonic (pushover) analyses and the experimental results are cyclically obtained, a backbone curve for the Pavia door wall is derived. The backbone curve is created by assembling and connecting the base shear load H at the extreme displacement d_2 of each cycle (Figure 4-25 – black line).
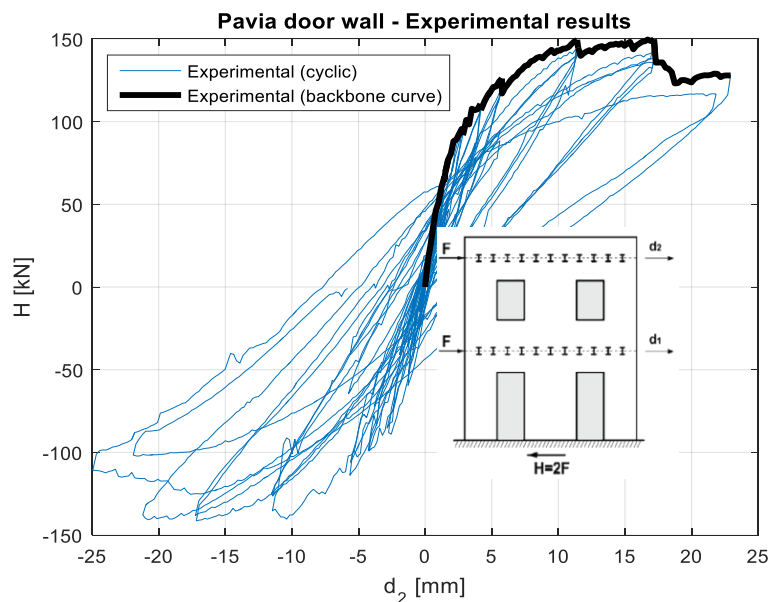
Figure 4-25 Cyclic and corresponding experimental backbone curve for the Pavia door wall.

4.2.2.1 Continuum models and Fibre flexure model

Figure 4-26 shows the force-displacement envelopes for the TZ-CM as well as for the FFM, describing the relation between the base shear force H and the lateral displacement at second floor d_2. Experimental and numerical crack patterns, bending moment (Mz), shear force (Qy) and normal force (Nx) diagrams have been extracted (if possible) at six loading stages (Figure 4-26), namely d_2 being equal to 5.76 mm (line A), 11.4 mm (line B), 15.3 mm (line C), 17.2 mm (line D), 22.9 mm (line E) and 32.1 mm (line F). While for the continuum models the crack propagation pattern is shown by means of the principal total tensile strains, the main tensile cracks of the FFM are presented by extracting and plotting the axial $\left(\sigma_{yy}\right)$ stress

distribution at the location of the bottom controlling section of pier P2 and P3. All of the above mentioned data is presented in Table 4-8.

Material properties	Model	Mesh size	f_{jt}	G_{f-t}^{I}	f_{tu}	G_{f-tu}^{I}
		mm	MPa	N/mm	MPa	N/mm
	CM	200	0.04	0.02	0.04	0.02
	TZ-CM	200	0.04	0.005	0.14/0.24	0.05
	FFM	200	0.04	0.005	-	-
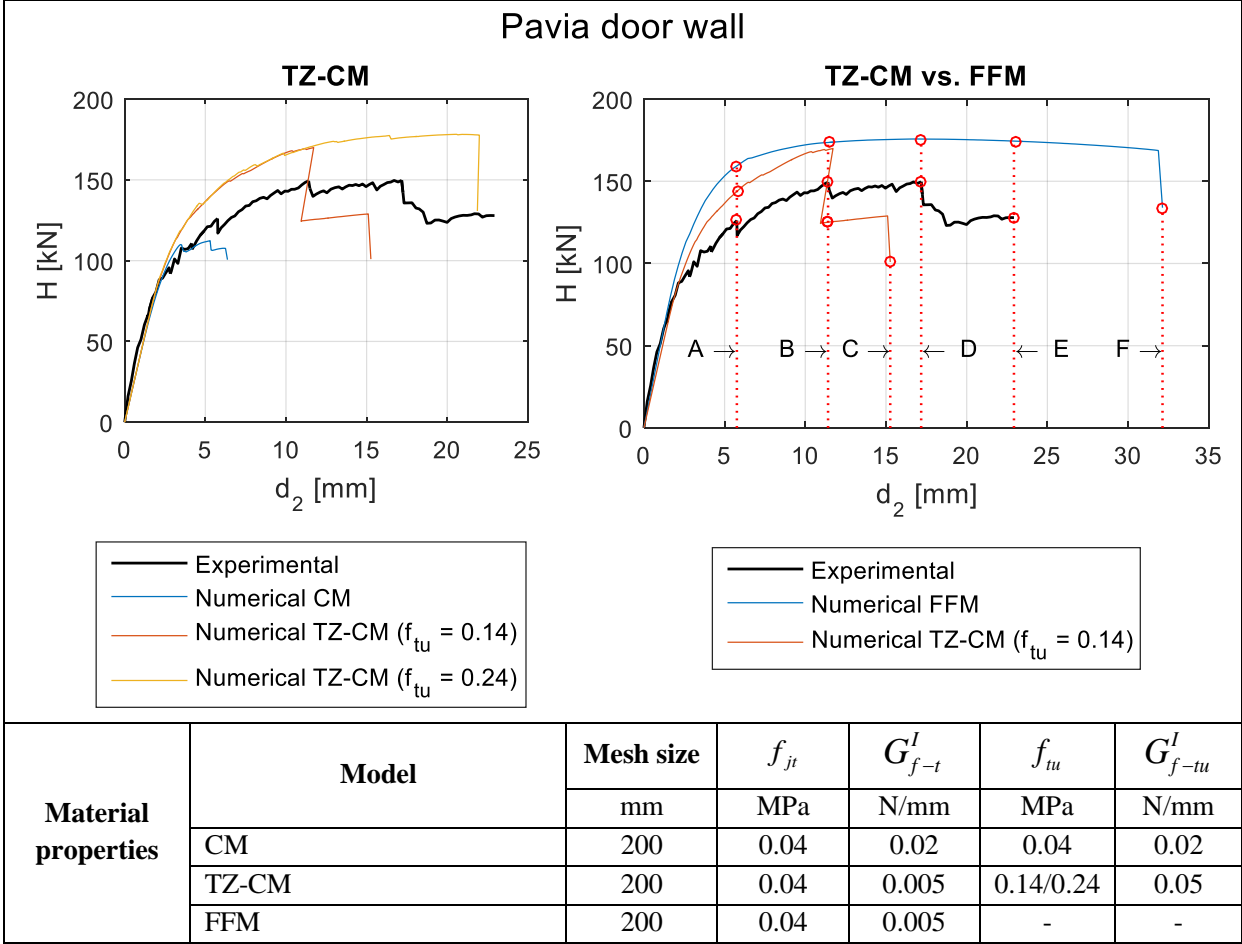
Figure 4-26 Force-displacement curves for the CM, the TZ-CM and FFM.

Again, the parameter sensitivity study on the TZ-CM clearly illustrates that an isotropic model in combination with homogeneous bed joint material properties for all continuum elements (CM) cannot describe the correct masonry behaviour (Figure 4-26 – blue line). However, adopting the TZ-CM approach as presented in Chapter 3 a more correct relation between the base shear load H and the lateral displacement at second floor d_2 is found (Figure 4-26 – red/yellow line), although the determination of the reference masonry tensile strength f_{tu} remains questionable if no experimental information is available. Another observation that can be made is that the influence of the parameter f_{tu} is characterized by an effect on the deformation capacity of the masonry façade, which is explained by considering the fact that this parameter is closely related to the relatively brittle shearing failure mode. Depicting the principal total tensile strains E1 of the TZ-CM for f_{tu} = 0.14 N/mm^2 it is observed that, entering the inelastic branch, the stiffness reduction is mainly caused by flexural cracks in the piers as well as in the spandrels at ground floor (Figure 4-26 and Table

4-8 – point A). The peak resistance reached its maximum at the lateral displacement of about $d_2 = 11.4$ mm (Figure 4-26 – point B)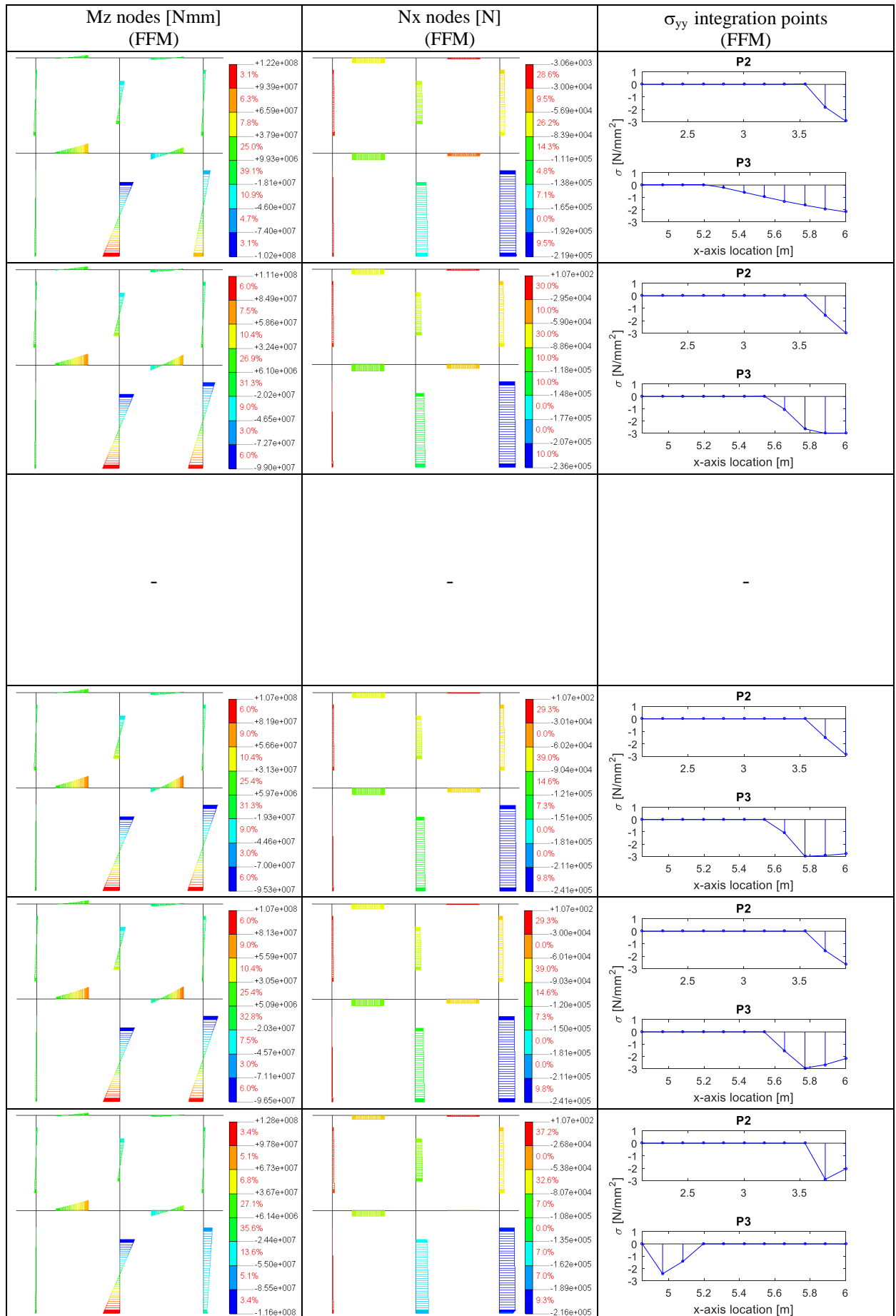, underestimating the lateral displacement at peak strength in the experimental simulation (Figure 4-26 – point D). As observed in the experiments, for the TZ-CM a sudden overall failure is associated with diagonal cracking of both the external and internal piers (Figure 4-26 and Table 4-8 – point B and C).

As highlighted in the previous paragraph, due to the limitations of the FFM regarding the shearing failure mode, the overall structural response is essentially flexural. Investigating the axial stress distributions at the extreme sections of the piers, it was observed that the stiffness reduction was mainly caused by flexural cracks formed at top and bottom sections of the internal and right-external pier at ground floor (Table 4-8 - σ_{yy} integration points). As hardly any flexural damage was observed in the spandrels, the above mentioned piers responded as double-clamped columns (symmetric bending), consequently giving identical crack patterns at top and bottom sections (Table 4-8 – Mz nodes). Considering the flexural cracks present in spandrels of the TZ-CM, consequently giving non-symmetric bending and non-identical flexural crack patterns in the main load bearing piers P2 and P3 (Table 4-8 – point A), this also explains the difference between the FFM and the TZ-CM in terms of the force-displacement diagram; i.e. a lower rate of stiffness reduction and a higher peak strength. Then, for an increasing lateral displacement the axial normal force in pier P3 gradually increases (Table 4-8 – Nx nodes), initiating pier failure in compression (Table 4-8 – σ_{yy} integration points) and activating a gradual decrease in strength (Figure 4-26 – point D). The progressive compression crushing in pier P3 (Table 4-8 – σ_{yy} integration points – point D/E/F) eventually leads to a sudden decline in base shear load H and finally the ultimate lateral displacement is reached (Figure 4-26 – point F).

As can be observed from Figure 4-26, the TZ-CM as well as the FFM underestimates the global stiffness reduction due to flexural cracking. There are two main reasons why. First, the static monotonic (pushover) analyses adopted in this work are less damaging than the cyclic approach carried out in experiments. Second, modelling the seismic masonry behaviour on the basis of isotropic material assumptions, the determination of the strength parameters is still open to question.

Table 4-8 Experimental and numerical crack propagation patterns, shear force, bending moment and normal force diagrams for the Pavia door wall.

Point	d_2	Crack pattern (experimental)	Principal Total Strain E1 (TZ-CM ($f_{tu} = 0.14$))	Qy nodes [N] (FFM)
A	5.76			
B	11.4			
C	15.3	-		-
D	17.2		-	
E	22.9		-	
F	32.1	-	-	

75

Mz nodes [Nmm] (FFM)	Nx nodes [N] (FFM)	σ_{yy} integration points (FFM)

Although the FFM has shown its limitations regarding the shearing failure mode and consequently in the post-peak behaviour, an acceptable accuracy in terms of initial stiffness, stiffness reduction and peak strength is attained. However, the main goal was to minimize the computational effort significantly, simultaneously maximizing the robustness of the computational process. Table 4-9 clearly shows that the number of elements, nodes, integrations points and calculation time of the FFM is significantly reduced compared with that of the TZ-CM. Besides, for the FFM hardly any convergence problems were observed, meaning that a higher robustness is achieved.

Table 4-9 Mesh data and computational effort for both the TZ-CM and FFM.

Model	Total elements	Total nodes	Total integration points	Load steps	Maximum number of iterations	Calculation time
TZ-CM (f_{tu} =0.14)	1141	3379	4564	0.01(181)	500	20:48
FFM	82	160	1804	0.01(137)	500	2:33

4.2.2.2 Sensitivity Analyses

In this section the influence of the mesh size on the accuracy and calculation time of the FFM is discussed. Four different mesh sizes are investigated in which the piers and spandrels are represented by: one beam element (Finite element mesh 1), three equally sized beam elements (Finite element mesh 2), a localized mesh refinement located at the extreme sections combined with one greater beam element in the middle (Finite element mesh 3) and a variation in which the middle part is represent by four equally sized beam elements (Finite element mesh 4). All previously mentioned finite element meshes are presented in Figure 4-27 and the total number of elements, nodes, load steps, maximum number of iterations and calculation times are given in Table 4-10.

The resulting numerical force-displacement curves for all four finite element meshes and main strength parameters are shown in Figure 4-28. The figure clearly shows that the finite element approximation eventually converges to a convergence limit, although the effect of the last refinement is limited. Therefore, it should be concluded that the localized mesh refinement adopted in the Finite element mesh 3 is a powerful technique finding the right balance between necessary accuracy and precision and the efficiency (computational time).

Finite element mesh 1	Finite element mesh 2

Finite element mesh 3	Finite element mesh 4
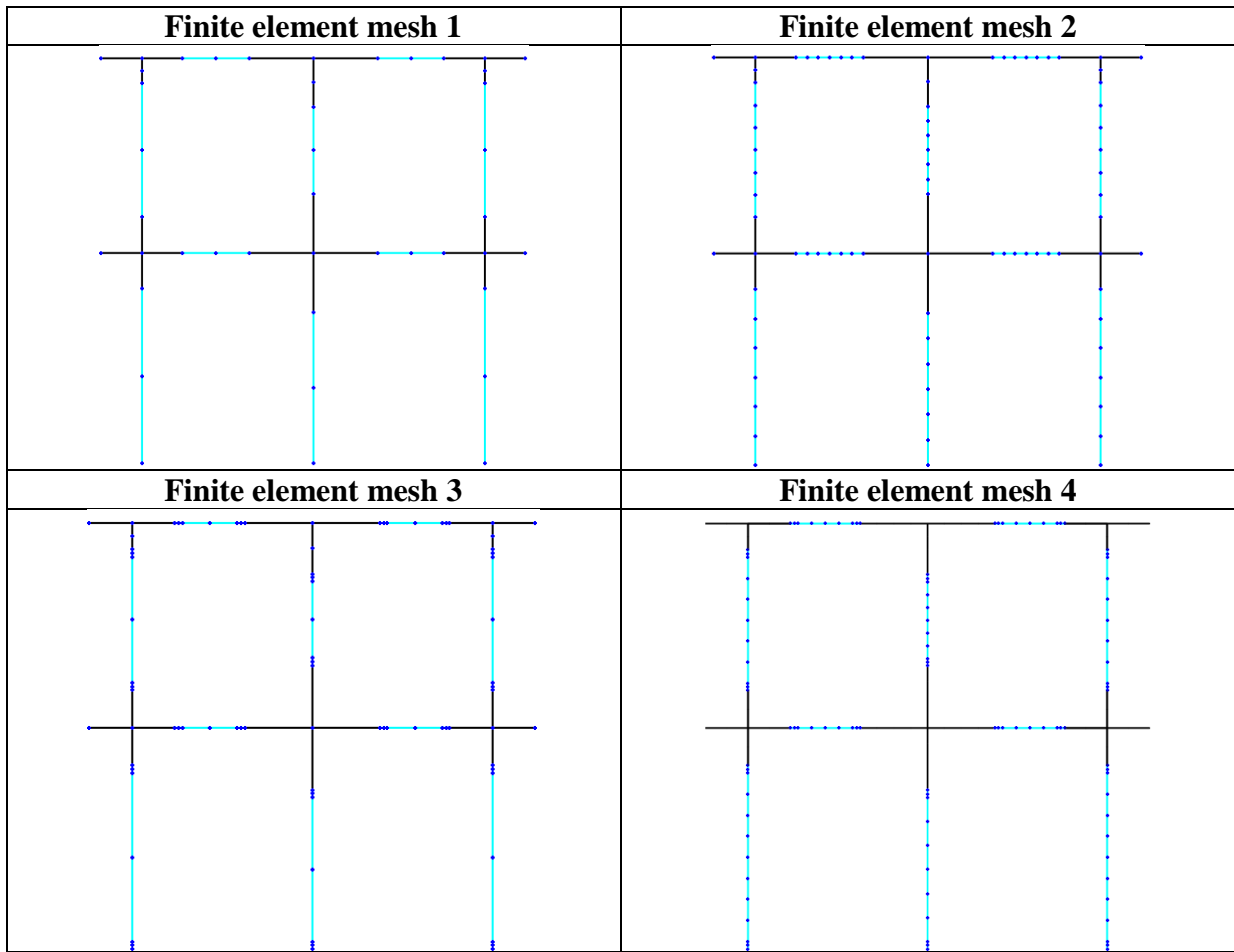
Figure 4-27 Finite element meshes with adopted in the mesh sensitivity analysis.

FFM – mesh sensitivity – Pavia door wall | **1:35**

Equivalent frame idealization

Material properties	Model	f_{jt}	G^{I}_{f-jt}
		MPa	N/mm
	FFM	0.04	0.005
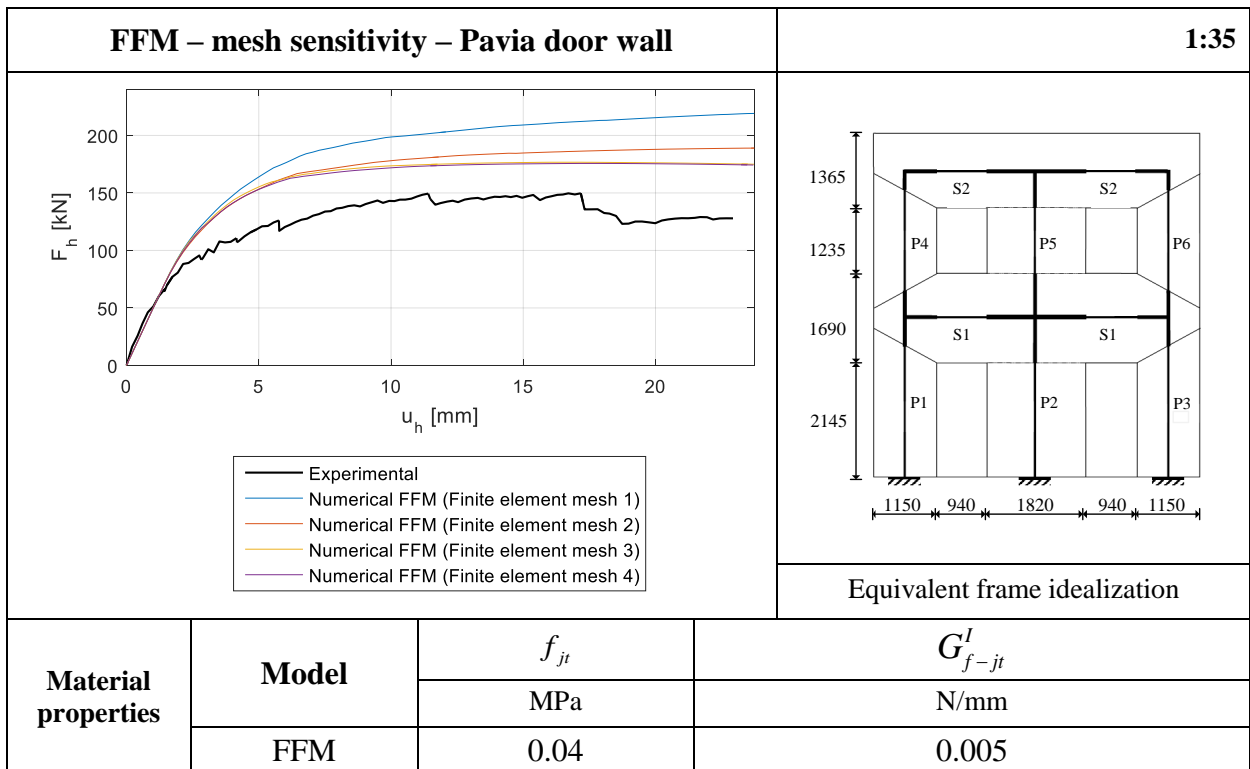
Figure 4-28 Force-displacement curves for all four finite element meshes (FFM).

Finite element mesh	Total elements	Total nodes	Load steps	Maximum number of iterations	Calculation time
1	26	48	0.01(100)	50	0:12
2	46	88	0.01(100)	50	0:23
3	46	88	0.01(100)	50	0:36
4	82	160	0.01(100)	50	1:20

4.2.2.3 Fibre flexure – lumped shear model

The FFM considered in the preceding section idealized the structural response as purely flexural. As shear failure (i.e. diagonal cracking and sliding) is a typical failure mode in masonry and should be accounted for especially in case of squat wall panels (e.g. spandrels), in the finite element model considered here, both the flexural and shear failure mode have been evaluated by means of the FF-LSM presented in section 3.3. The finite element mesh shown in Figure 4-29 consist of 66 numerically integrated beam elements (Figure 4-29 – blue) and 10 nodal interface elements (Figure 4-29 – red), respectively describing the flexural and shear behaviour of each structural component. The most relevant adopted input parameters for the flexural as well as the shearing failure mode are presented in the table below.

FF-LSM				
Piers	flexure	blue	f_{jt}	G^I_{f-jt}
	shear	red	c	μ
Spandrels	flexure	blue	f_{ts}	G^I_{f-tu}
	shear	red	c	(μ)

Figure 4-29 The finite element mesh and adopted parameters for FF-LSM.

As mentioned in section 4.2.1, initially it will be assumed that all piers have double fixed boundary conditions resulting into a shear span $H_0/H = 0.5$ (referred to as ''priori''). Second, as the shear spans are highly affected by spandrel failure initiation, the resulting shear spans of the main load bearing piers (P2, P3 and P5), present at the last load step of the analysis, are evaluated and implemented in an updated analysis (referred to as ''posteriori''). As a result seven configurations have been examined being a function of the adopted shear strength criterion for piers, the shear strength criterion adopted for spandrels, the priori/posteriori input of the shear span parameter and the assumed softening behaviour for both the cohesion and friction parameter (Table 4-11). A more elaborated description of the analyses configurations including the input values for each pier separately can be found in Appendix A.

Table 4-11Analysed configurations for the Pavia door wall with the FF-LSM.

Analysis	Shear strength criterion			Softening	
	Pier	Shear span	Spandrel	Pier	Spandrel
1	-	-	-	-	-
2a	Mann and Müller	P	Mann and Müller	-	-
2b	Mann and Müller	P	Beyer	-	-
3a	Magenes and Calvi	P	Beyer	-	-
3b	Magenes and Calvi	PS	Beyer	-	-
3c	Magenes and Calvi	PS	Beyer	LS+DL	-
4a	Abrams	P	Beyer	-	-
4b	Abrams	PS	Beyer	-	-
LS+DL = Linear Softening + Drift Limitation; P = priori; PS = posteriori;					

Figure 4-30 compares the force-displacement curve obtained with the FFM (purely flexural response) and that obtained with the FF-LSM describing flexural as well as shearing failure. Additionally, both the deformed shapes and bending moment diagrams at a lateral displacement d_2 of approximately 30mm are shown in Table 4-12.

Comparing the results of analysis 3a/3b and 4a/4b with analysis 2b and observing that close similarity exist in terms of force displacement diagrams, it is concluded that it is especially the spandrel-pier interaction that dominates the load bearing capacity of the entire masonry wall. This is also supported by the fact that, despite the pier shear failure initiation in analysis 3b and 4b (Table 4-12), the pier strength reductions hardly affect the force-displacement

curves (Figure 4-30 – Analysis 3a and 4a vs. Analysis 3b and 4b). There are two reasons for this. The first is that for all analyses configurations spandrel failure usually initiated at an early stage, inducing a boundary effect on the main load bearing piers P2 and P3, increasing the shear spans (e.g. Table 4-12 – Analysis 1 vs. Analysis 2b) and consequently decreasing the flexural resistance of the piers mentioned. As a result, comparing the peak resistance with that obtained with the FFM (Figure 4-30 – Analysis 1 vs. Analysis 2b), a significant strength reduction is observed, thereby enhancing the numerical model predictions. Second, the posteriori determined shear ratios of the main load bearing piers are as such that the shear resistance is close to but somewhat smaller than the flexural resistance, causing a slight reduction in peak strength (Figure 4-30 – Analysis 3b and 4b).
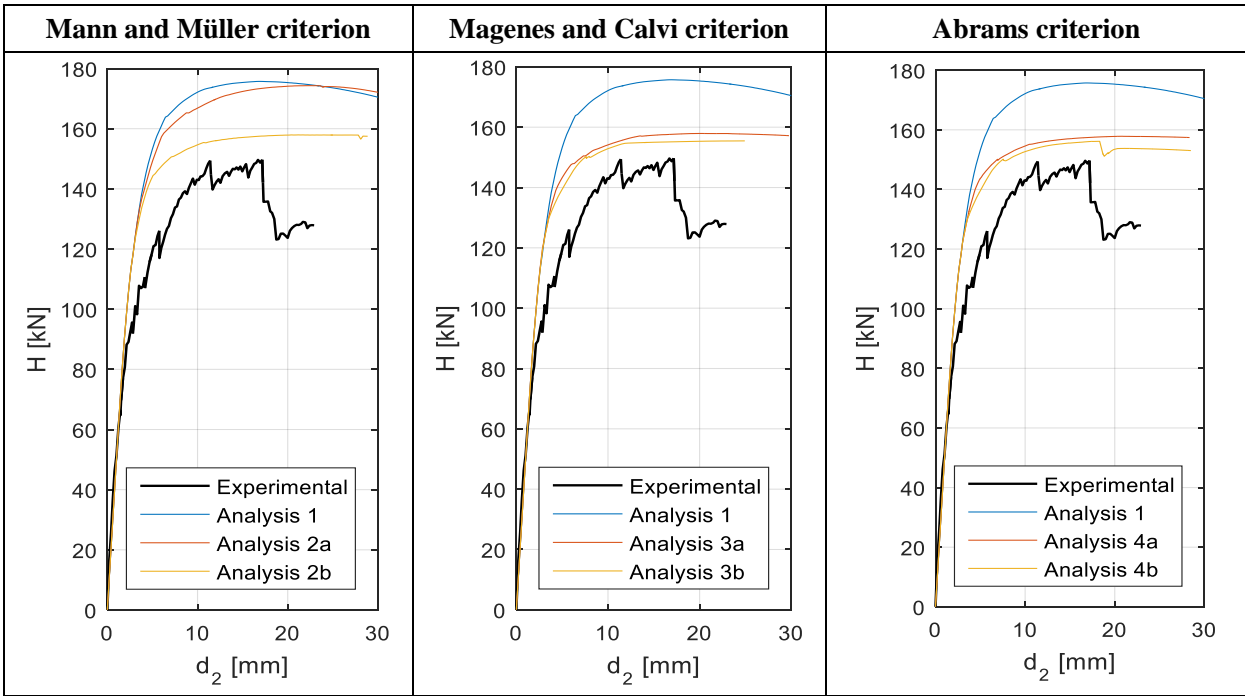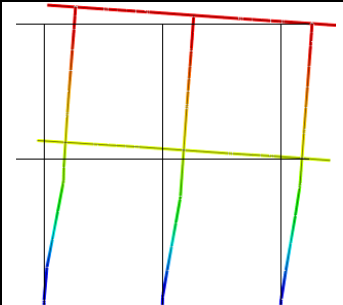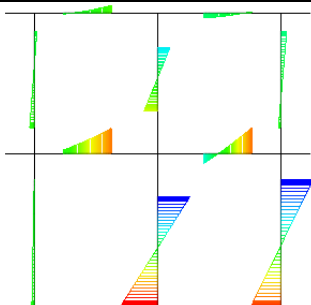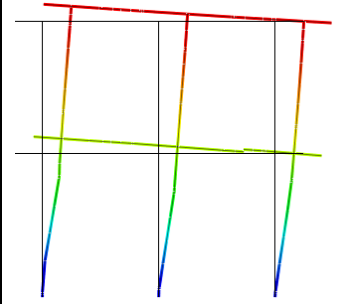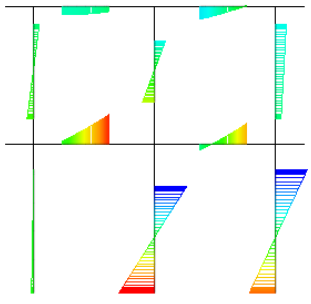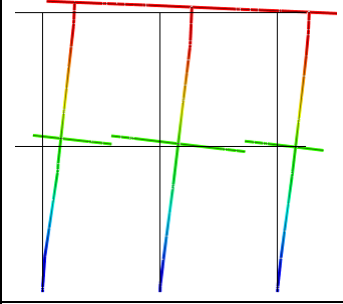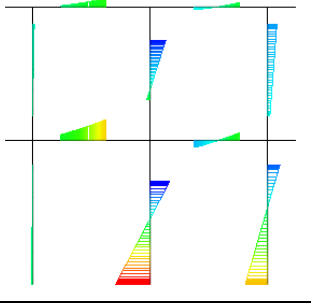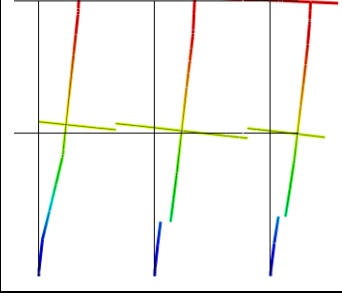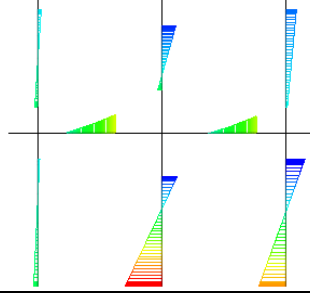

Figure 4-30 Experimental and numerical force displacement curves of the FFM (Analysis 1) and the FF-LSM (Analysis 2-4) for the Pavia door wall.

Comparing the lateral displacements (Table 4-12) with the experimental observations and considering the adopted failure criteria, the observations and conclusions are in line with what have been observed in section 4.1.2.3 and 4.1.3.2. Again, the Mann and Müller ((Table 4-12 – Analysis 2b) criterion appeared to be somewhat unconservative as no pier shear failure was initiated, whereas the Magenes and Calvi criterion (Table 4-12 – Analysis 3b) correctly described the experimentally observed failu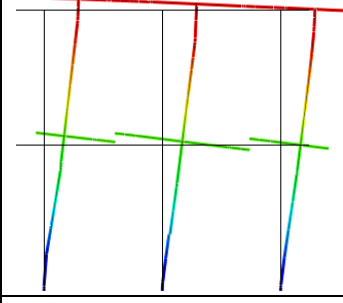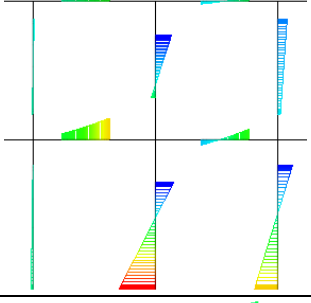re modes; i.e. shearing failure of pier P2, pier P3 and both spandrels at first floor. The adopted criterion in Abrams (Table 4-12 – Analysis 4b) correctly described shearing failure of pier P2 and both spandrels at second floor, but predicted a shear failure of pier P5 that has not been observed in the experiment and failed to capture the correct response of pier P3.

Table 4-12 Deformed shape and bending moment diagram for the Pavia door wall with the FFM and FF-LSM.

Analysis	Lateral displacements [mm]	Mz nodes [Nmm]
1		
2a		
2b		
3a		
3b		

| 4a | | | | |
| 4b | | | | |

Table 4-13 examines the trade-offs between the computational costs and accuracy for the TZ-CM, the FFM and the FF-LSM. The table clearly shows that the implementation of the shearing failure mode enhanced substantially the model accuracy, although the improvement comes at a price, as with the implementation convergence problems were much more often observed. The problem at hand is solved by specifying automatic adaptive displacement increments, maximizing the robustness of the computational process and maintaining an acceptable balance between computational cost and accuracy (Table 4-13).

Table 4-13 Mesh data and computational effort for the TZ-CM, the FFM and FF-LSM.

Model	Total elements	Total nodes	Total integration points	Load steps	Maximum number of iterations	Running time	Error
	[-]	[-]	[-]	[-]	[-]	[min]	[%]
TZ-CM (f_{tu} =0.14)	1141	3379	4564	0.01(181)	500	20:48	14
FFM (analysis 1)	82	160	1804	0.01(137)	500	2:33	17
FF-LSM (analysis 3b)	76	118	1672	Automatic step sizes	500	2:00	5

Again, optionally a panel collapse can be considered by a limitation of the ultimate drift. Hence, the violation of the maximum allowable structural component deformation incorporates a strength degradation of one or more structural components. The strength degradation model adopted here yields a linear softening diagram for the shear strength as well as the friction parameter, initiated when top displacement of pier P2 or P3 violates the drift capacity belonging to the shearing failure mode (i.e. 0.4%).

Figure 4-31 discusses the force-displacement curve of the elaborated and extended FFM that considers both the shearing failure mode and a panel collapse via a drift limitation (FF-LSM). Analysing the lateral top displacements of both pier P2 and P3, it was observed that it was pier P2 for which the strength degradation was initiated, reducing the overall strength of the masonry wall (Figure 4-31 - red circle).

Considering again the balance between computational costs and accuracy, there are two conclusions to draw here. On the one hand, with the implemented linear softening behaviour a more realistic relation between ultimate forces and displacements is obtained, but on the other hand, great convergence problems arise when a structural component enters the softening branch. Therefore, the mention technique can be a powerful technique to consider panel drift limitations, but if the influence of panel softening behaviour needs to be studied, deeper investigation into the convergence problem is necessary.

Material properties	Model	f_{jt}	G^I_{f-jt}	δ_u
		MPa	N/mm	%
	FF-LSM	0.04	0.005	0.4
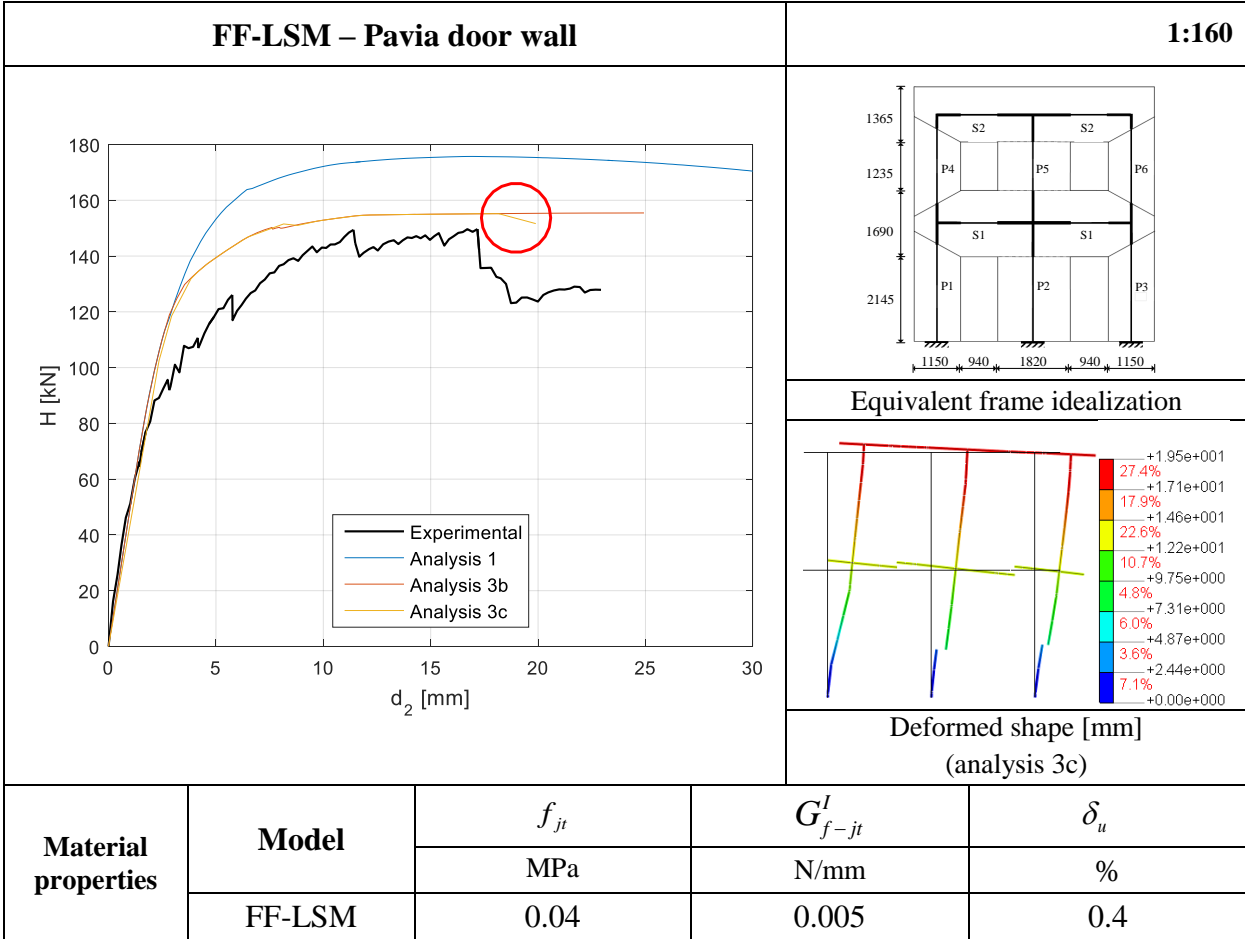
Figure 4-31 Experimental and numerical force displacement curves of the FFM (Analysis 1) and the FF-LSM including an ultimate drift limitation (Analysis 3c) for the Pavia door wall.

4.2.3 Comparison with TREMURI

Existing equivalent frame methods (e.g. the commercial version of TREMURI) are usually based on lumped plasticity models (i.e. non-linear behaviour is limited to the end- and midsection of the element). In such models the cracked condition of the panel is evaluated via analytical failure criteria and an ideal plastic behaviour is assumed whenever the nodal generalized forces of the macro element attains one of the analytical predicted limit values. In the previous sections it has been shown that the distributed inelasticity approach discussed in this work is able to provide a better representation of the cracked condition of the masonry panel, as the flexural response is evaluated by summing up all the individual responses (tensile or compressive stresses) at material point level. As a consequence, the structural component is no longer defined as either ''cracked'' or ''not cracked'' (this leading to a simplified bilinear behaviour), but a progressive stiffness reduction (due to flexural cracks) of the masonry panel is simulated until the maximum resistance of the component is reached.

The software TREMURI has been used to model the two-storey masonry façade analysed in section 4.2, as reported by Lagomarsino et al. (2013).

The comparison between the results obtained with TREMURI and those with the FFM/FF-LSM (Figure 4-32) highlights the differences in the pre-peak stiffness reduction: while the TREMURI result is characterized by sharp bends (caused by the activation of ideal plastic behaviour), the force-displacement curve found with DIANA results in a more smoothed-line graph bringing the data closer to experimental results. Furthermore, analysing the section stress distributions of the FF-LSM at a number of heights for the internal pier at first floor (Appendix B), it is observed that inelasticity is not strictly limited to the end-sections. Again, this should be interpreted as closer to reality, as masonry panels failing in bending are typically characterised by several flexure cracks distributed over the height.

Finally, it should be noted that just as in existing equivalent frame methods the FF-LSM uses a lumped approach for possible shearing modes, making use of analytical strength predictions. In preceding sections it has been shown that peak load estimations were rather accurate, but that the approach entails a crude representation of the cracked condition of a masonry panel in case of shearing failure modes. Therefore, despite the improvements made by adopting fibre beam elements, there are still opportunities for further enhancements.

TREMURI – Pavia door wall	DIANA – Pavia door wall
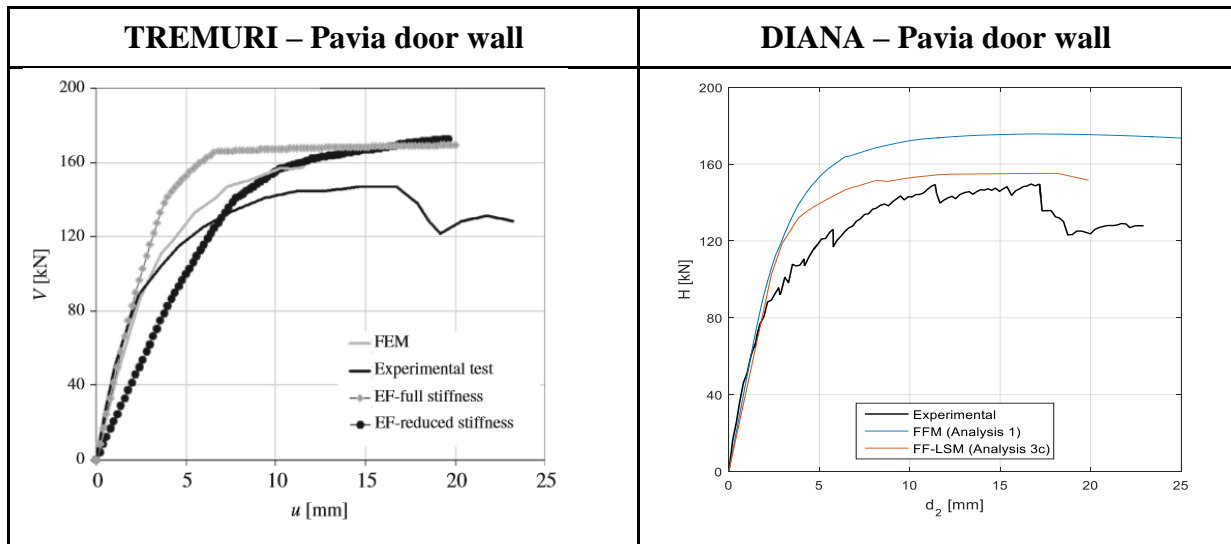
Figure 4-32 Numerically simulated force-displacement diagrams simulated through TREMURI (on the left , Lagomarsino et al. (2013)) and DIANA (on the right).

5 CONCLUSIONS AND RECOMMENDATIONS

5.1 Conclusions

Academic interest in researching equivalent frame methods have been growing in recent years, as researchers recognized the need for simpler and computationally more attractive concepts to analyse masonry structures. In line with this trend, this work focused on a comparison between the results obtained by the application of a continuous model and an equivalent frame model (named *fibre flexure model*) for the assessment of the global response of masonry structures, adopting numerically integrated plane stress and fibre beam elements, respectively. Furthermore, the paper addressed an extension of the fibre flexure model that includes the use of nodal interface elements to describe shear failure (in this work referred to as *fibre flexure – lumped shear model*). To validate the numerical models two different types of benchmarks have been investigated, respectively representing the behaviour of either a single structural component (masonry pier) or a composite façade. The following conclusions can be drawn from the study:

1. Under the assumptions of isotropic and homogenous bed joint material properties for all plane stress elements the *Continuum Model (CM)* is not able to estimate correctly the structural failure of the structural component when shear failure modes are expected. Adopting the *Three Zoned - Continuum Model (TZ-CM)* in which each structural component is subdivided into three different zones where both the flexural and shear behaviour are separately described, the correlation between numerical and experimental results is significantly improved. An important parameter that indicates the need for the zoned approach is the ratio between the reference masonry tensile strength and the bed joint tensile strength, since for values significantly different from one, the tensile resistance of the shearing zone differs considerably from the tensile resistance of the flexural zone. However, the estimation of the properties that belong to the shearing zone (reference masonry tensile strength and fracture energy) remains a difficult process and experimental information is hardly available, while it highly affects the ultimate drift capacity.

2. The *Fibre Flexure Model (FFM)*, idealizing the structural response as purely flexural, is capable of simulating the rocking failure mode of a structural component, whereas it fails to simulate shearing modes such as diagonal cracking and sliding. Although the

FFM shows limitations regarding the shearing failure mode and the prediction of the post-peak behaviour, an acceptable accuracy in terms of initial stiffness (pre-peak), stiffness reduction and peak strength is attained for masonry structures containing relatively slender structural components (e.g. the composite façade tested in Pavia). Besides, compared with the continuum models, the FFM significantly reduces the number of elements, nodes and integration points, consequently minimizing the computational effort and maximizing the computational robustness. In comparison with the corresponding continuum models the computation time decreases by a factor of approximately 10. The best strategy for generating the beam finite element mesh (component discretization) is the localized mesh refinement technique (two smaller beam elements at the top and bottom and one greater beam element in the middle), combined with an integration scheme that consist of two Gaussian integration points along the bar axis and eleven integration points (or fibres) in the area of the cross section.

3. The experimental results of the in-plane tests on replicated masonry walls performed at the TU Delft show that the reciprocal of the experimental mean shear strength divided by the applied vertical pressure increased linearly with the shear ratio; i.e. the influence of the shear ratio is not affected by the type of damage propagation. For the TZ-CM as well as the FFM significant deviations between the experimental and numerical dependency on the shear ratio were observed and for decreasing shear ratios the numerical error of especially the FFM amplifies dramatically. Therefore, both models are not suitable for the analysis of masonry structures containing relatively squat structural components, although the limitation is much stronger for the FFM and calibration of the parameters of the TZ-CM may lead to enhanced results.

4. The shortcoming of the FFM regarding the shearing failure mode can be overcome by adopting the *Fibre Flexure – Lumped Shear Model (FF-LSM)* that considers both the nonlinear flexural and nonlinear shear response of the structural component. While the FFM without the nodal interface simply determines the ultimate rocking strength of the masonry panel and, consequently, overestimates the ultimate shear strength in case of squat members, the FF-LSM is able to properly predict the shear capacity of both slender and squat walls (although the observed level of accuracy depends largely on the adopted shear failure criterion). The FF-LSM is capable of correctly predicting the pre-peak behaviour (i.e. initial stiffness, stiffness reduction and peak strength) of a composite façade and detects correctly both flexural and shearing failure modes in

piers and spandrels. Analyzing a composite façade, compared with the FFM, the FF-LSM slightly reduces the computational robustness, but computationally it is still very attractive as the computational time is significantly reduced (in a similar degree mentioned for the FFM). Optionally, the structural failure of the components (panel collapse) can be considered by specifying softening diagrams for the shear strength parameters, which activates when the structural component violates an ultimate drift capacity. This solution improves the post-peak behaviour of the model, but it is computationally not very attractive as great convergence problems arise when a structural component enters a softening branch.

5.2 Recommendations

The FF-LSM shows promising potential for the analysis of masonry structures, minimizing computational effort and maximizing the computational robustness on one hand, maintaining an acceptable degree of accuracy on the other. However, a number of steps are required before the method can be safely adopted in engineering practice:

- While the fibre section discretization, describing the flexural response, acts on material point level and is in essence dependent on local material properties, the nodal interface simplifies the description of the nonlinear shear behaviour into one single relation between analytically described global strength parameters. In chapter 3 it was shown that these global strength parameters were dependent on local material properties, but had to be modified preventing the model from over-predictions. Pursuing an equivalent frame model that is consistent with regards to the material input for both failure modes, it is recommended to design a ''structural masonry nodal interface'' that exclusively requires local material properties and allows the user to easily select different type of failure criterions. Then, the interface element should calculate the global shear resistance dependent on the selected failure criterion (Table -2), on the base of the local material parameters, the confining pressure and the shear ratio (i.e. boundary conditions). As the boundary conditions and the confining pressures are constantly changing during the analysis, the global shear resistance should be updated after each load step. Once the shear resistance is violated a perfect plastic behaviour can be assumed combined with a softening behaviour for the shear strength, activated when a panel drift limitation is reached.

- The drift capacity of rocking unreinforced masonry walls is currently investigated throughout empirical and mechanical models. Also the application of the proposed numerical model may provide suitable estimations of the ultimate displacement capacity of a rocking pier.

- The behaviour of spandrels is still not completely understood and is part of on-going research in several laboratories all over the world: so far, contradictory findings have been observed, and also the stiffness effect provided by different types of lintels is still not completely understood. To broaden the applicability of the FF-LSM available analytical spandrel failure criteria for different type of masonry spandrels should be listed, validated experimentally and numerically (i.e. with existing continuum and equivalent frame methods) and implemented into the DIANA code.

- For the structural analysis of complex 3D structures, a fully three-dimensional extension of the FF-LSM is necessary. For dealing with 3D structures the capabilities of the numerically integrated beam elements with regards the out of plane behaviour of masonry, the effect of different floor systems (modelling of diaphragms) and the 3D assembling of masonry walls should be discussed and examined thoroughly.

- Extensions of the model should offer the possibility to consider the response of masonry under cyclic static or dynamic loading conditions. Cyclic nonlinear tensile and shear stress-strain relations should be derived and implemented into the FEM code, accurately describing the strength and stiffness degradation of the input parameters.

- In recent years a considerable amount of effort has been devoted to the development of shear-flexural fibre beams for the design and assessment of reinforced concrete beams (Ferreira et al., 2013). Discretizing the cross section into two types of fibres, non-shear resistance fibres subjected to 1D axial stresses only and shear resistant fibres submitted to a multiaxial stress-strain state, the elements have shown promising results in achieving a right balance between computational effort and accuracy. The approach of using both non-shear and shear resistance fibers is still in its infancy, but it is recommended to consider these types of elements also in seeking the optimal solution for modelling flexural as well as shearing failure modes within the fibre beam element formulations.

REFERENCES

Atkinson, R. H., Noland, J. L., & Abrams, D. P. (1985). A deformation failure theory for stack-bond brick masonry prisms in compression. In *7th International Brick and Block Masonry Conference* (Vol. 1, pp. 577-592). Melbourne, Australia.

Beyer, K. 2012. Peak and residual strengths of brick masonry spandrels, *Engineering Structures, 41*, 533-547.

Beyer K., Dazio A. 2012. Quasi-static cyclic tests on masonry spandrels. *Earthquake Spectra 28(3)*, 907-929.

Beyer, K., & Mangalathu, S. (2012). Review of strength models for masonry spandrels. *Bulletin of Earthquake Engineering, 11(2)*, 521-542.

Beyer, K., & Mangalathu, S. (2014). Numerical Study on the Peak Strength of Masonry Spandrels with Arches. *Journal of Earthquake Engineering, 18(2)*, 169-186.

Calderini, C., Cattari, S., & Lagomarsino, S. (2010). The use of the diagonal compression test to identify the shear mechanical parameters of masonry. *Construction and Building Materials*, 24(5), 677-685.

Cattari, S., & Beyer, K. (2015). Influence of spandrel modelling on the seismic assessment of existing masonry buildings. In *Proceedings of the Tenth Pacific Conference on Earthquake Engineering Building an Earthquake-Resilient Pacific.* Sydney, Australia.

Cattari, S. (2007). *Modellazione a telaio equivalente di strutture esistenti in muratura e miste muratura-c.a.: formulazione di modelli sintetici.* (Doctoral dissertation, University of Genoa, 2007). Genoa, Italy.

Cattari, S., & Lagomarsino, S. (2008). A strength criterion for the flexural behaviour of spandrel in un-reinforced masonry walls. In *Proceedings of the 14th World Conference on Earthquake Engineering.* Beijing, China.

Crisafulli, F. J. (1997). *Seismic behaviour of reinforced concrete structures with masonry infills.* (Master's thesis, University of Canterbury, 1997). Christchurch, New-Zealand.

De Borst, R., & Nauta, P. (1985). Non-orthogonal cracks in a smeared finite element model. *Engineering Computations*, 2(1), 35-46.

Hilsdorf, H. K. (1969). Investigation into the Failure Mechanisms of Brick Masonry Loaded in Axial Compression. In F. B. Johnson (Ed.), *Designing, engineering, and constructing with masonry products; proceedings* (pp. 34-41). Houston, Texas: Gulf Publishing.

Lagomarsino, S., Penna, A., Galasco, A., & Cattari, S. (2013). TREMURI program: An equivalent frame model for the nonlinear seismic analysis of masonry buildings. *Engineering Structures, 56*, 1787-1799.

Lofti, H. R., & Shing, P. B. (1991). An appraisal of smeared crack models for masonry shear wall analysis. *Computers & Structures*, 41(3), 413-425.

Lourenço, P. J. (1996). *Computational strategies for masonry structures* (Master's thesis, Delft University of Technology, 1996). Delft: Delft University Press.

Magenes, G., & Calvi, G. M. (1997). In-plane seismic response of brick masonry walls. *Earthquake Engineering and Structural Dynamics*, 26(11), 1091-1112.

Magenes, G., & Della Fontana, A. (1998). Simplified non-linear seismic analysis of masonry buildings. In *Proceedings of the British Masonry Society* (pp. 190-195). London, England.

Magenes, G. (2000). A method for pushover analysis in seismic assessment of masonry buildings. In *Proceedings of the 12th world conference on earthquake engineering* (pp. 1-8). Auckland, New Zealand.

Manie, J., & Kikstra, W. P. (Eds.). (2009). *DIANA - Finite Element Analysis - User's Manual - Element Library* (1st ed., Vol. 9.4). Delft, The Netherlands: TNO DIANA.

Mann, W., & Muller, H. (1982). Failure of Shear-Stressed Masonry. An Enlarged Theory, Tests and Application to Shear Walls. In *Proceedings of the British Ceramic Society* (pp. 223-235). Stoke-on-Trent, England.

Marques, R., & Lourenço, P. B. (2011). Possibilities and comparison of structural component models for the seismic assessment of modern unreinforced masonry buildings. *Computers & Structures*, 89(21-22), 2079-2091.

Matsagar, V. (Ed.). (2016). *ADVANCES IN STRUCTURAL ENGINEERING* (Vol. 2). doi:10.1007/978-81-322-2193-7

Mcnary, W. S., & Abrams, D. P. (1985). Mechanics of Masonry in Compression. *Journal of Structural Engineering J. Struct. Eng., 111*(4), 857-870.

Messali, F. (2015). *Hollow brick masonry walls: In-plane seismic response and strengthening techniques with reinforced high-performance mortar coating.* (Unpublished doctoral dissertation). University of Brescia, Italy.

Page, A.W. (1981). The Biaxial Compressive Strength Of Brick Masonry. *Proceedings of the Institution of Civil Engineers*, 71(3), 893-906.

Page, A. W. (1982). An Experimental Investigation of the Biaxial Strength of Brick Masonry. In *6th International Brick and Block Masonry Conference* (pp. 3-15). Rome, Italy.

Rots, J. G. (1988). Computational modeling of concrete fracture (Doctoral dissertation, Delft University of Technology, 1988). Delft, The Netherlands.

Rots, J. G. (1991). , Numerical Simulation of Cracking in Structural Masonry. *Heron*, 36(2), 49-63.

Rots, J. G., & Blaauwendraad, J. (1989). Crack Models for Concrete, Discrete or Smeared? Fixed, Multi-Directional or Rotating? *Heron*, 34(1), 1-59.

Rots, J. G., Nauta, P., G.M.A., K., & Blaauwendraad, J. (1985). Smeared Crack Approach and Fracture Localization in Concrete. *Heron*, 30(1), 1-48.

Sepe, V., Spacone, E., Raka, E., & Camata, G. (2014). Seismic analysis of masonry buildings: equivalent frame approach with fiber beam elements. *In Proceedings of the 9th International Conference on Structural Dynamics* (pp. 237-244). Porto, Portugal.

Turnsek, V., & Cacovic, F. (1971). Some Experimental Results on the Strength of Brick Masonry Walls. In *2nd International Brick and Block Masonry Conference* (pp. 149-156). Stoke-on-Trent, England.

Turnsek, V., & Sheppard, P. (1980). The Shear and Flexural Resistance of Masonry Walls. In *Proceedings of the International Research Conference on Earthquake Engineering* (pp. 517-573). Skopje, Yugoslavia.

Van Der Pluijm, R. (1992). Material properties of masonry and its components under tension

and shear. In *Proc. 6th Canadian Masonry Symposium* (pp. 675-686). Saskatoon, Saskatchewan.

Van Der Pluijm, R. (1993). Shear behaviour of bed joints. In *Proc. 6th North American Masonry Conference* (pp. 125-136). Philadelphia, Pennsylvania.

Van Der Pluijm, R. (1993). Shear behaviour of bed joints. In *Proc. 6th North American Masonry Conference* (pp. 125-136). Philadelphia, Pennsylvania.

APPENDIX A

In the table below the adopted shear failure criteria for piers as well as for spandrels are shown. As mentioned before, among other things, the Magenes and Calvi and Abrams criterion for piers are dependent on the resulting shear span and both the resulting normal force and shear span, respectively. Both parameters are highly affected by the spandrel behaviour and tend to stabilize when spandrels fail in shear (usually at an early stage of the pushover analysis). Making use of the above mentioned phenomena and detecting the normal force and shear span present in the concerning piers present just after spandrel failure occurrence a better estimation of the pier shear strength has been pursued. The input variables including those posteriori implemented (given in grey) are presented in the table below.

Analysis	Shear strength criterion							Post peak behaviour of piers and spandrels	
1	-							-	
2a	**Pier**		Mann and Müller		**Spandrel**	$\bar{c}$	$\bar{\mu}$	**Pier**	**Spandrel**
			$\bar{c}$	$\bar{\mu}$					
	P1-P6		0.18	0.45	S1-S2	0.15	0.39	EPP	EPP
2b	**Pier**		Mann and Müller		**Spandrel**	c_{sp}	μ_{sp}	**Pier**	**Spandrel**
			$\bar{c}$	$\bar{\mu}$					
	P1-P6		0.18	0.45	S1-S2	0.15	0	EPP	EPP
3a	**Pier**		Magenes and Calvi		**Spandrel**	c_{sp}	μ_{sp}	**Pier**	**Spandrel**
		$\frac{H_0}{H}$	α_v	c_{mc}	μ_{mc}				
	P1	0.50	1.1	0.09	0.22	S1-S2	0.15	0	EPP	EPP
	P2	0.50	0.6	0.11	0.28				
	P3	0.50	1.1	0.09	0.22				
	P4	0.50	0.8	0.10	0.25				
	P5	0.50	0.3	0.13	0.34				
	P6	0.50	0.8	0.10	0.25				
3b	**Pier**		Magenes and Calvi		**Spandrel**	c_{sp}	μ_{sp}	**Pier**	**Spandrel**
		$\frac{H_0}{H}$	α_v	c_{mc}	μ_{mc}				
	P1	0.50	1.1	0.09	0.22	S1-S2	0.15	0	EPP	EPP
	P2	0.65	0.8	0.10	0.25				
	P3	0.60	1.3	0.08	0.20				
	P4	0.50	0.8	0.10	0.25				

	P5	0.95	0.6	0.11	0.27
	P6	0.50	0.8	0.10	0.25

	Pier			Magenes and Calvi		**Spandrel**	c_{sp}	μ_{sp}	**Pier**	**Spandrel**
		$\frac{H_0}{H}$	α_v	c_{mc}	μ_{mc}					
3c	P1	0.50	1.1	0.09	0.22	S1-S2	0.15	0	LS+DL	EPP
	P2	0.65	0.8	0.10	0.25					
	P3	0.60	1.3	0.08	0.20					
	P4	0.50	0.8	0.10	0.25					
	P5	0.95	0.6	0.11	0.27					
	P6	0.50	0.8	0.10	0.25					

	Pier				Abrams		**Spandrel**	c_{sp}	μ_{sp}	**Pier**	**Spandrel**
		$\frac{H_0}{H}$	α_v	p	c_e	μ_e					
4a	P1	0.50	1.1	0.3	0.10	0.16	S1-S2	0.15	0	EPP	EPP
	P2	0.50	0.6	0.4	0.15	0.25					
	P3	0.50	1.1	0.3	0.10	0.16					
	P4	0.50	0.8	0.1	0.06	0.11					
	P5	0.50	0.3	0.2	0.13	0.23					
	P6	0.50	0.8	0.1	0.06	0.11					

	Pier				Abrams		**Spandrel**	c_{sp}	μ_{sp}	**Pier**	**Spandrel**
		$\frac{H_0}{H}$	α_v	p	c_e	μ_e					
4b	P1	0.50	1.1	0.3	0.10	0.16	S1-S2	0.15	0	EPP	EPP
	P2	0.65	0.8	0.3	0.12	0.20					
	P3	0.60	1.3	0.6	0.13	0.22					
	P4	0.50	0.8	0.1	0.06	0.11					
	P5	0.95	0.6	0.2	0.08	0.14					
	P6	0.50	0.8	0.1	0.06	0.11					

EPP = elastic perfectly plastic; LS+DL = Linear Softening + Drift Limitation

Parameters given in grey are posteriori implemented, making use of an updated analysis.

APPENDIX B

* on the x-axis the integration points in the area of the cross section are shown